High Precision Separation and Recovery Process of Rare Earth Elements from Neodymium Magnet Scrap Using Molten Salt

Hang Hua
2022

Contents

List of Tables

List of Figures

Chapter 1
General Introduction

1.1   Characteristics of Rare-earth (RE) Elements

RE elements are a suite of seventeen elements in the periodic table. There are several different ways to classify RE elements. The common definition is that those with small atomic numbers are called light rare earth elements and those with large atomic numbers are called heavy rare earth elements. According to one classification, lanthanum (La), cerium (Ce), praseodymium (Pr), neodymium (Nd), promethium (Pm), and samarium (Sm) are called light RE elements.[1] The other eleven, europium (Eu), gadolinium (Gd), terbium (Tb), dysprosium (Dy), holmium (Ho), erbium (Er), thulium (Tm), ytterbium (Yb), lutetium (Lu), scandium (Sc), and yttrium (Y) are called heavy RE elements.[1] Elements from La to Lu are called lanthanides, which are f-block elements, corresponding to the filling of the inner 4f electron orbital, except for La which is a d-block element. The atomic radius of the lanthanide elements decreases as the atomic number increases, and this phenomenon is called "lanthanide contraction". The chemical properties of the RE elements are very similar and thus extremely difficult to separate from each other. Sc and Y are also included in the RE group, because they tend to occur in the same mineral deposits as the lanthanide and exhibit similar chemical properties.

Since RE metals are contained in minor metals, they are generally considered to be highly rare in nature. However, RE elements are not as "rare" as the name implies. For example, Ce, the most abundant of the RE elements, is more abundant in the earth's crust than nickel (Ni), copper (Cu), and lead (Pb), which are the major industrial metals. Even the least abundant element (except
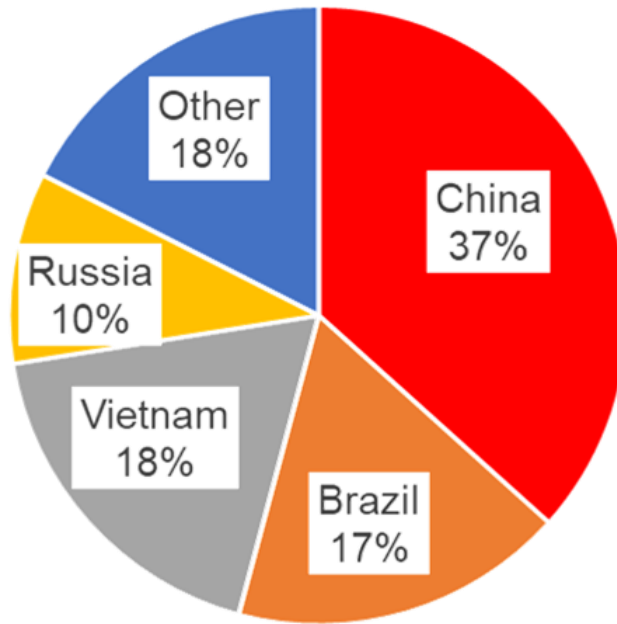
Fig. 1-1 **Share of the proven reserves of RE elements in oxide conversion. Total reserve is estimated as 120 Mt in 2020.[2]**

Pm) Lu is much more abundant than silver (Ag), platinum (Pt), and gold (Au), which are known as the precious metals. Nevertheless, as shown in Fig 1-1, more than 80% of the world's proven reserves of RE are concentrated in a small number of countries.[2] Therefore, the supply of RE elements is often limited due to production technology, environmental issues, and circumstances in the producing countries.

1.2   Conventional RE Production Methods

RE metals smelting was first implemented by Mosander in 1827.[3] Then, von Welsbach developed the molten salt electrolysis method for producing mischmetal, a mixture of RE metals, in the early 19th century.[4]

The standard Gibbs energies of formation for RE oxides are negatively larger than those for most of metal oxides. For example, the standard Gibbs energy of formation for CeO_2 is -1024.6 kJ $(\text{mol-}O_2)^{-1}$ at 298.15 K and this value is more negative than that for $2Na_2O$, -750.92 kJ $(\text{mol-}O_2)^{-1}$.[5] Since Na is unstable in the air and reacts rapidly with oxygen, the powdery Ce also reacts

rapidly with oxygen in the air. The standard redox potential of Ce^{3+}/Ce in aqueous solution is -2.34 V (vs. SHE) at 298.15 K,[6] which mean Ce^{3+} cannot be reduced to Ce metal in aqueous solution like Cu^{2+}. Furthermore, CeO_2 cannot be reduced by carbon or hydrogen like Fe_2O_3. Until now, there are only three main methods applied to the production of large quantities of RE products.[1]

    (a) Molten salt electrolysis method

    (b) Metallothermic reduction method

    (c) Metallothermic reduction and distillation method

1.2.1 Molten Salt Electrolysis Method

Generally, molten salt electrolysis methods are classified into three types: "chloride molten salt electrolysis", "RE oxide electrolysis in fluoride bath" and "fluoride molten salt electrolysis".[1,7-9] Principles and features are described below.

1.2.1.1 Chloride Molten Salt Electrolysis[1]

Chloride molten salt electrolysis was adopted in the early 1900s to produce mischmetal, which is a RE alloy, used for lighter flint. Until 1975, this method was used not only for lighter flint but also for the large production of additives to steel. Dehydrated RE chloride salt is dissolved in molten KCl–$NaCl$–$CaCl_2$ and electrolyzed by using a carbon anode and a metal cathode. The reactions are expressed as follow:

$$RE^{3+} + 3\ e^- \rightarrow RE \qquad\qquad (1),$$

$$2\ Cl^- \rightarrow Cl_2\uparrow + 2\ e^- \qquad\qquad (2),$$

$$2\ RECl_3 \rightarrow 2RE + 3\ Cl_2\uparrow \qquad\qquad (3).$$

RE metal is electrodeposited as liquid metal at the bottom of electrolysis bath. Because the carbon anode is on the top of molten salt, Cl_2 gas is released immediately and collected by NaOH solution. Owing to the high hygroscopicity of RE chloride salts, the electrolysis efficiency significantly decreases when water is present. Moreover, water-containing RE chloride salt transforms to RE

oxychloride salt when it is dehydrated at 400 to 450 °C. The RE oxychloride salt does not dissolve in the molten chloride salt and precipitates at the bottom of the bath to pollute the electrodeposited RE metal. In this process, Fe was initially used as the cathode, but Mo and Ta, which do not alloy with RE metals, were used to avoid contamination from the cathode. The current efficiency of the practical process is around 60% and RE metals are obtained as mischmetal with 85–90% yield.

1.2.1.2 RE Oxide Electrolysis in Fluoride Bath[1,7]

RE oxide electrolysis method is similar to the electrolytic Al smelting process, where RE oxide is dissolved in a fluoride bath and electrolyzed. Compared with the RE chloride used in the chloride molten salt electrolysis, RE oxide and fluoride are stable and non-hygroscopic. For the production of Nd metal, NdF_3–LiF–BaF_2 is a common fluoride molten system, which is operated at 900–1000 °C.[10] Mischmetal can also be produced by this method in a molten REF_3–LiF–BaF_2 system. The reactions are described as:

$$RE^{3+} + 3\ e^- \rightarrow RE \tag{4},$$

$$C + 2\ O^{2-} \rightarrow CO_2\uparrow + 4\ e^- \tag{5},$$

$$2\ RE_2O_3 + 3\ C \rightarrow 4\ RE + 3\ CO_2\uparrow \tag{6}.$$
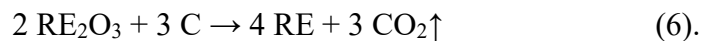
It should be noted that the concentration of RE oxides needs to be rigorously controlled. Because when the concentration of RE oxides is insufficient, the fluoride in this system will be electrolyzed. Then, the formed non-conductive fluorocarbon layer covers the carbon anode and cut off the flow of current. In other words, the anode effect occurs in this situation. When the concentration of RE oxides is too high, undissolved RE oxides precipitate as RE oxyfluorides at the bottom of the bath. The current efficiency of this method is 80–85% and mischmetal is obtained with 90–95% yield. Since this method produces high-purity mischmetal containing no RE oxychloride, it is used for mass production of mischmetal for hydrogen storage alloys. Furthermore, not only the mischmetal but also the Nd master alloy used in the production of Nd–Fe–B magnet is manufactured by this method using an Fe cathode.

1.2.1.3 Fluoride Molten Salt Electrolysis[1,8,9]

As described in the previous section, anode effect would occur when pure fluoride is electrolyzed. However, since the anode effect is difficult to occur in molten salts with high LiF content, a carbon anode can be used in such fluoride systems. The Nd master alloy for the Nd–Fe–B magnet is manufactured by this method. The reactions are described as:

$$Nd^{3+} + 3\ e^- + x\ Fe \rightarrow NdFe_x \qquad (7),$$

$$2\ F^- \rightarrow F_2\uparrow + 2\ e^- \qquad (8),$$

$$2\ NdF_3 + 2x\ Fe \rightarrow 2\ NdFe_x + 3\ F_2\uparrow \qquad (9).$$
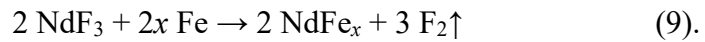
The current efficiency of this method is around 70%. The advantages are high purity alloys and long-time electrolysis, and the disadvantages are the difficulty and high cost in treating the generated F_2 gas.

1.2.2 Metallothermic Reduction Method[1]

Compared with the molten salt electrolysis method, the ability to obtain high-purity RE metal is the greatest advantage of the metal thermal reduction method. In this method, the dehydrated RE fluoride salt is usually reduced by Ca metal at high temperature. For example, NdF_3 is reduced to Nd metal in the following reaction:

$$NdF_3\ (s) + 3/2\ Ca\ (s) \rightarrow Nd\ (l) + 3/2\ CaF_2\ (s) \qquad (10).$$
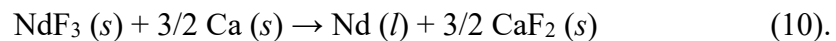
The standard Gibbs energy of the reaction is -160 kJ mol^{-1} at 900 °C, thus the reaction proceeds to the right thermodynamically. After the reaction, Nd metal can be separated in a liquid state. Other RE metals such as Dy, Tb, and Gd are also produced by the same method. In order to obtain the high-purity RE metal, high-purity RE fluoride salt is required as the raw material.

For the RE metal with high melting point such as Y (T_m = 1557 °C), Mg metal is used to produce the RE alloy with low melting point such as Y–Mg alloy. Y sponge is obtained after the evaporation of Mg.

1.2.3 Metallothermic Reduction and Distillation Method[1]

Metallothermic reduction and distillation method is used for the production of Sm which is used to produce the Sm–Co magnet. Because of the largely negative redox potential of Sm^{2+}/Sm and the high vapor pressure of Sm metal, the molten salt electrolysis and metallothermic reduction methods described above cannot be adapted to Sm production. On the other hand, by using the high vapor pressure of Sm metal, a distillation recover method was adapted. The reaction of the method is described as:

$$Sm_2O_3\ (s) + 2\ La\ (l) \rightarrow 2\ Sm\ (g) + La_2O_3\ (s) \qquad (11).$$
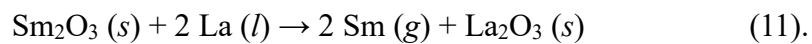
Although the standard Gibbs energy of this reaction is $+15$ kJ mol^{-1} at 1000 °C, the reaction proceeds to the right as Sm is removed from the system. La metal can be replaced by cheaper mischmetal. After evaporative purification, high-purity Sm metal is obtained in the low temperature part. By-product La_2O_3 is recycled as the raw material for mischmetal smelting.

1.3 Applications of RE Elements and Characteristics of Nd Magnet

The applications and demand for RE elements have been expanded over last few decades. In general, almost half of RE elements are used for catalyst and magnet.[11] Other important applications of RE elements are the functional alloy, glass, electronics, etc. Tables 1-1 and 1-2 summarize the main applications of light and heavy RE elements, respectively.[1,12-17]

RE magnet is one of the most important applications of RE elements. It is well known that RE magnet is much superior to the other permanent magnets such as ferrite and alnico magnets. The magnetic characteristics of typical magnets are summarized in Table 1-3.[18,19] Among them, Nd magnet shows excellent magnetic characteristics and is utilized in many industrial fields such as mobile phones, wind turbines, and motors for battery and hybrid electric vehicles (BEVs and HEVs). It is the strongest magnet available in the market, with a maximum energy product of 470 kJ m^{-3}.[19] In addition to the superior magnetic properties, reasonable production cost and high

Table 1-1   Main application of the light RE elements.[1,12]

Atomic number	Symbol	Main application
57	La	High refractive index and alkali-resistant glass, Flint, Hydrogen storage, Fuel cell electrode, Cracking catalyst, Abrasive
58	Ce	Abrasive, Yellow colors in glass and ceramic, Cracking catalyst
59	Pr	Nd magnet, Laser, Colorant in glasses and enamel, Abrasive
60	Nd	Nd magnet, Laser, Dielectric material, Abrasive
61	Pm	Nuclear battery, Luminous paint[12]
62	Sm	Sm magnet, Laser, Dielectric material

Table 1-2   Main application of the heavy RE elements.[1,12–17]

Atomic number	Symbol	Main application
21	Sc	Aluminum-scandium alloy, Solid electrolyte, Radioactive tracing agent[12]
39	Y	YAG laser, High-temperature superconductor, Microwave filter, Laser, Steel additive, Sintering aid, Fuel cell electrode, Solid electrolyte
63	Eu	Red and blue phosphor, Laser, Fluorescent lamp, NMR relaxation agent
64	Gd	Laser, Neutron capture, MRI contrast agent, NMR relaxation agent, Magnetostrictive alloy, Steel additive, Fuel cell electrode
65	Tb	Nd magnet additive, Green phosphor, Fluorescent lamp, Magnetostrictive alloy, Solid electrolyte
66	Dy	Nd magnets additive, Magnetostrictive alloy, Solid electrolyte
67	Ho	Lasers, Magnetic superconductor, Yellow or red colors in glass
68	Er	Infrared laser, Vanadium steel additive, Fiber-optic technology, Superconductor
69	Tm	Laser, X-ray source, High-temperature superconductor[13]
70	Yb	Laser, Stainless steel additive[12], Stress gauge,[13] Source of gamma ray,[14] Ion qubits for quantum computing[15]
71	Lu	Catalyst, High refractive index immersion lithography,[16] PET scan detector[17]

Table 1-3   Characteristics of typical permanent magnets.[18-19]

Magnet classification	Primary phase	Residual magnetization B_r / T	Coercivity H_c / MA m^{-1}	Curie temp. T_c / °C	Maximum energy product $(BH)_{max}$ / kJ m^{-3}
Ferrite	$SrFe_{12}O_{19}$	0.41	0.265	450	34
Alnico	$Al_8Ni_{21}Co_5Cu_3Fe_{63}$	1.25	0.052	800	43
Rare earth magnets	$SmCo_5$	0.88	0.66	720	150
	Sm_2Co_{17}	1.08	0.8	820	220
	$Nd_2Fe_{14}B$	1.28	0.9	310	470

mechanical strength are also the advantages of Nd magnet. Although Nd magnet shows superior properties, it still has a weakness of lower Curie temperature as shown in Table 1-3. Therefore, in order to maintain its superior magnetic properties at high temperatures, addition of other RE elements like Tb and Dy to the magnet is necessary. By using the intergranular diffusion method, it is possible to replace some of Nd with Tb or Dy to maintain the required magnetic force at high temperatures, although the magnetic moment is lowered.[20,21] Such magnets are called heat-resistant Nd magnets. Because of the economical reason, Dy is usually added to the Nd magnet. Typically, about 1.3 kg of Nd magnet is required for the production of BEVs/HEVs.[22] Up to 10 wt. % of Dy is added to the Nd magnet as an additive, which corresponds to about 30% of RE elements contained in the magnet.[22] Since BEVs/HEVs emit less amount of carbon dioxide than the conventional petrol-driven vehicles, they are expected to spread worldwide as they contribute to the promotion of carbon neutrality. Therefore, the production of BEVs/HEVs will increase rapidly in the near future. The demand for Nd and Dy will rise in accordance with the increasing production of BEVs/HEVs.

1.4   RE Elements Recycling

1.4.1   Necessity of RE Elements Recycling

RE elements are naturally found in very low concentration in the environment. As

mentioned in section 1.1, RE elements are unevenly distributed in the limited countries. In particular, heavy RE elements are almost exclusively produced in China. Fig. 1-2 shows the import prices of Nd and Dy in Japan in recent years, and the prices changed dramatically due to political factors.[23] Although heavy RE mines are also found in some other countries, radioactive tailings due to Th and U in RE ores are a potential hazard, and improper handling of these substances can cause extensive environmental damage. Furthermore, strong acids are used in the mining process of RE minerals without adequate leakage prevention, which may leach into the environment and be transported through water, leading to acidification of the aquatic environment. Therefore, RE mining and refining can cause serious environmental problems if not managed properly.

The recycling of RE elements from the RE-containing scraps is a feasible way to obtain RE sustainably for the countries that have no RE resources and want to decrease the environmental load. Nowadays, RE elements accumulated in home appliances, such as an air-conditioner in which Nd magnet is used, are expected as urban mines to become alternative RE resources.[24] In 2020, around 160,000 tons and 12,000 tons of Nd sintered and bonded magnets have been sold worldwide, respectively.[25] Furthermore, the amount of Nd magnet scraps will increase with the popularity of
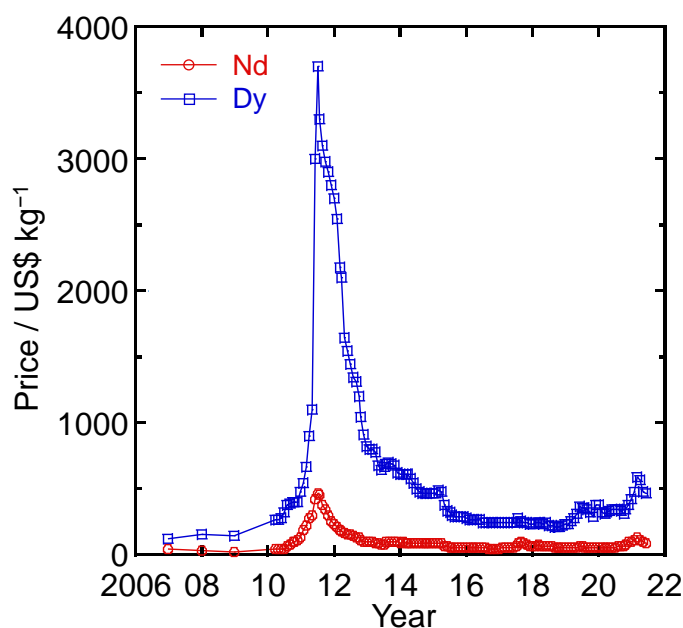
Fig. 1-2   **Import prices of Nd and Dy metals in Japan.[23]**

the BEVs/HEVs in the foreseeable future. Thus, RE elements recycling from Nd magnet scraps should be focused immediately. Currently, only a small amount of RE is recycled from in-process scraps discarded in the magnet manufacturing plants. A large amount of Nd magnet scraps generated in daily lives is either disposed of as garbage or accumulated as urban mines. In the recycling of the scrap of heat-resistant Nd magnets, the separation of Dy is necessary because the heat resistance is achieved by the presence of Dy of the grain boundary of the $Nd_2Fe_{14}B$ phase, and a mixture of Nd and Dy is inadequate as a raw material for heat-resistant Nd magnet.

1.4.2   RE Recycling Methods for Nd Magnet

In the manufacturing process of Nd magnet, a large amount of in-process scraps is generated. These scraps cannot be used as products due to high contamination concentrations of oxygen and other impurities. The cutting chips (sludge) generated during the cutting process also do not meet the product specifications. As a result, only about 70% of the raw materials become final products.[26] The relatively less-contaminated scraps without Dy may be used as raw material alloys by melting again at high temperature. However, some scraps are contaminated with a large amount of moisture and oil, so it is common to first dissolve them with acids. After several rounds of solvent extraction and filtration, high-purity hydrates of RE oxides and fluorides are obtained.[27] RE elements can be recovered as metal from RE oxides or fluorides by a molten salt electrolysis process.[28] Fig. 1-3 shows the flowchart of the Nd magnet scrap recycling process based on this hydrometallurgical method.[22] However, due to the disadvantages such as multistage process, high energy consumption, and high environmental load, it has not been widely adopted and is only used in magnet manufacturing plants.

Meanwhile, several new RE recycling methods have been proposed, which are described below. Some of them were initially proposed as a new smelting method for raw ores, but are also expected to be applied to the recycling of RE elements from Nd magnet scrap later on. Adachi et al. proposed a process named the chemical vapor transport (CVT) method and Fig. 1-4(a) shows

10
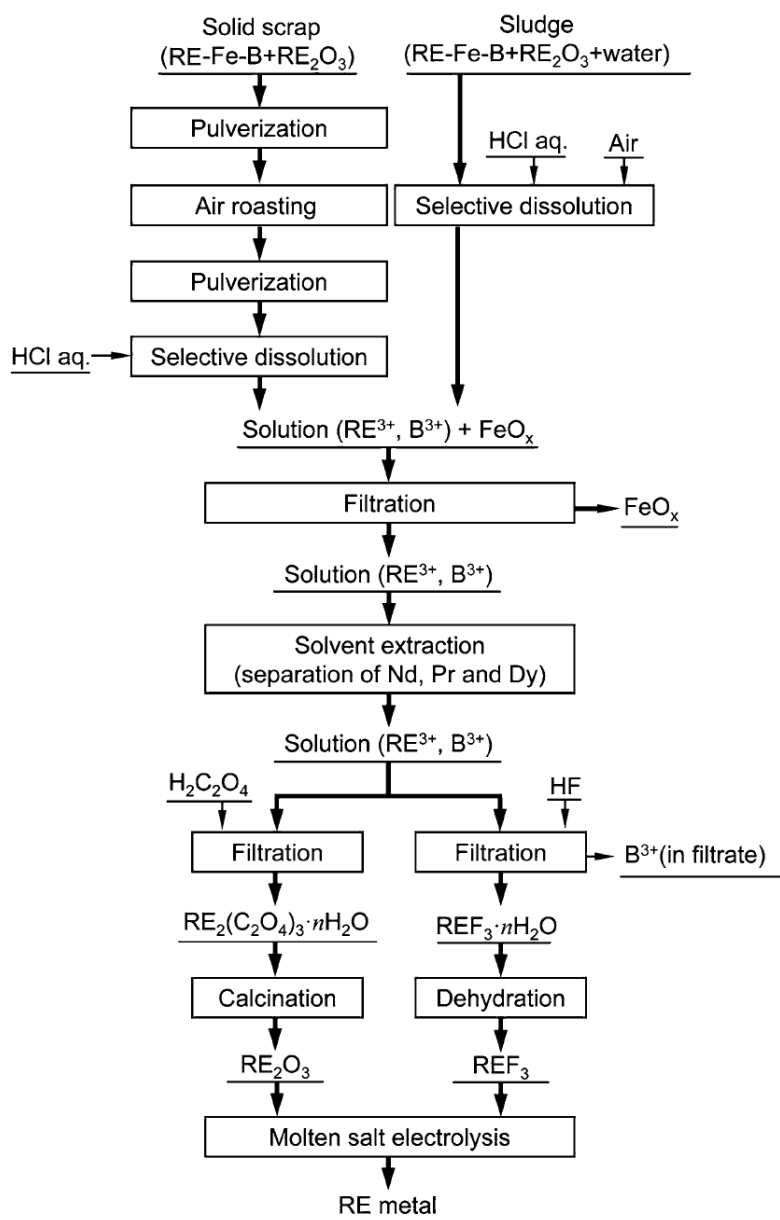
Fig. 1-3   **Recycling process for RE elements from Nd magnet scrap based on hydrometallurgical method.[22]**

the flowchart of this method.[22,29-33] In this process, RE chlorides are reacted with aluminum chloride vapor at high temperature to synthesize high-vapor-pressure complexes containing RE and Al. Each component is then separated and recovered by using the difference in vapor pressure of each complex. Murase et al. investigated the recovery of Sm, Nd, and Dy from Sm_2Co_{17} and Dy-added $Nd_2Fe_{14}B$ by using the CVT method.[31] Fig. 1-4(b) shows the distribution of $NdCl_3$, $SmCl_3$, and $DyCl_3$ deposits, and Fig. 1-4(c) shows the relationship between molar ratios of Nd:Dy, Sm:Dy,
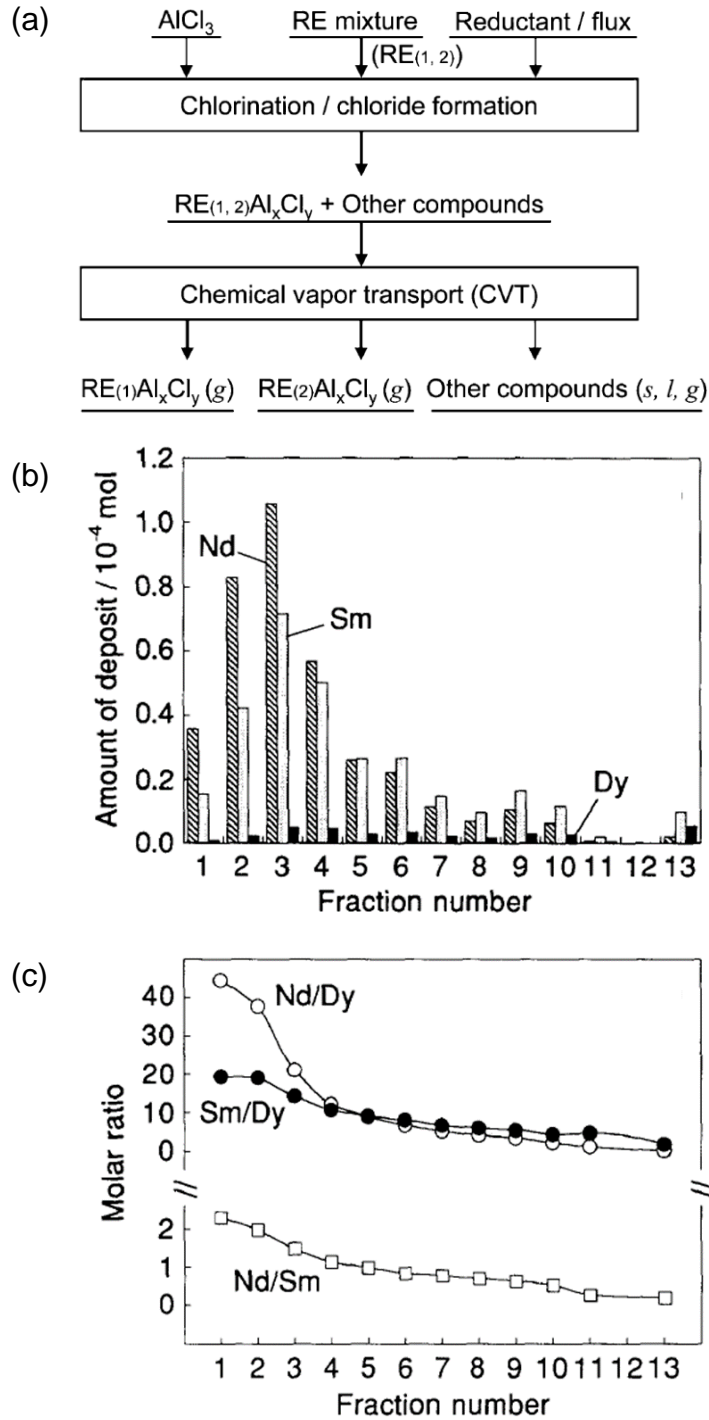
Fig. 1-4   **(a) RE elements separation and refining process by CVT method.[22,29-33] (b) Distribution of NdCl₃, SmCl₃, and DyCl₃ deposits and (c) relationship between molar ratios of Nd:Dy, Sm:Dy, and Nd:Sm and fraction number.[31]**

and Nd:Sm. Since the original molar ratio of Nd:Dy was approximately 12:1, the separation ability between RE is not very high.

Uda et al. also reported an evaporation method for RE recycling and Fig. 1-5(a) shows the flowchart of this method.[22,34,35] The RE components are separated using the difference in vapor pressure of chlorides or iodides with different valences. Fig. 1-5(b) shows chemical potentials of chlorine corresponding to the equilibria between $Ln/LnCl_2$ and $LnCl_2/LnCl_3$ at 1073 K. This method is innovative in focusing on the fact that the vapor pressure of halides differs largely between the divalent and trivalent forms,[34] which considerably increases the separation efficiency. Advantages such as fewer steps than the hydrometallurgical process and the high separation factor between Nd and Sm were achieved, but the separation between Nd and Dy was not reported.
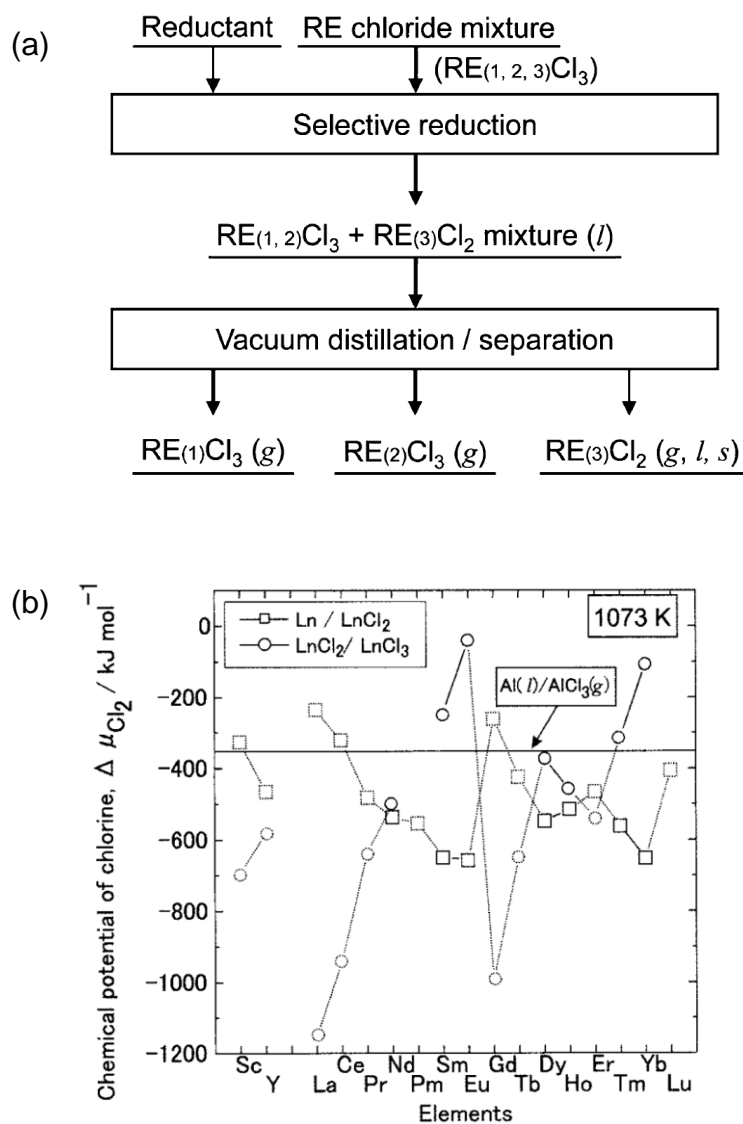
Fig. 1-5 **(a) Evaporative separation of RE chloride (or iodide) utilizing difference of vapor pressure between different valences states.[22,34-35] (b) Chemical potentials of chlorine corresponding to the equilibria between $Ln/LnCl_2$ and $LnCl_2/LnCl_3$ at 1073 K.[34]**

Several selective extraction methods have also been proposed.[36-48] Fig. 1-6(a) shows an example of a recycling method reported by Takeda et al.[22,38,40,42] In this method, RE elements are selectively extracted directly from Nd magnet scrap into molten Mg or Ag, which are extracting agents. Figs. 1-6(b) and (c) show Nd concentrations in extracted scraps and in Mg–Nd alloy with Mg metal, respectively.[42] As the results, most Nd was successfully extracted. The method using molten metal as an extracting agent has higher operating costs than the hydrometallurgical method. However, the molten metal method has the advantage of not generating liquid waste, which is especially important for recycling in developed countries with strict environmental regulations.

As described in Fig. 1-7, Uda et al. also developed a process to selectively separate and
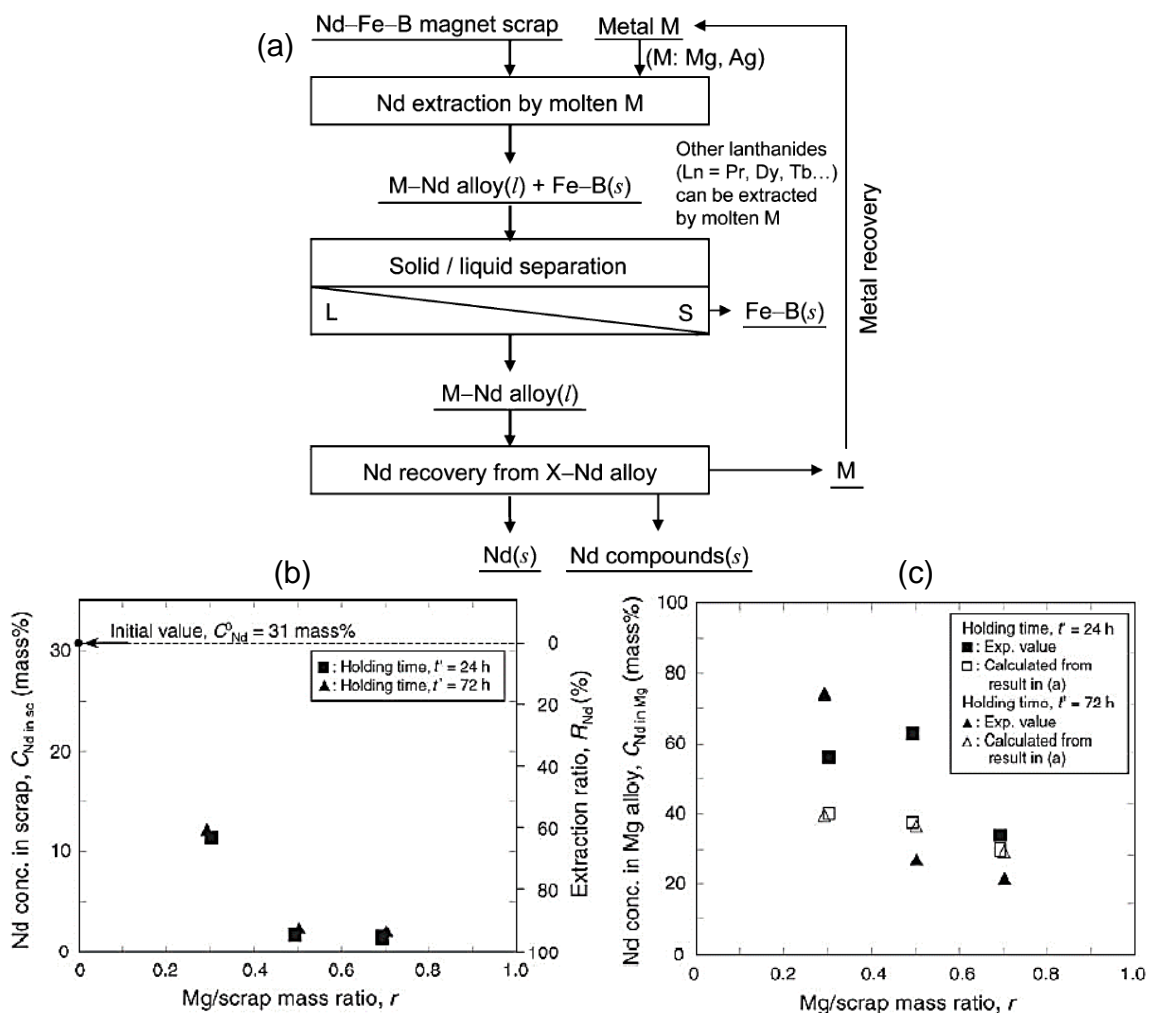
Fig. 1-6   (a) Selective extraction process of Nd metal directly from Nd magnet scrap by utilizing molten metals as extracting agents.[22,38,40,42] (b) Neodymium concentration in extracted scrap and (c) neodymium concentration in Mg–Nd alloy.[42]
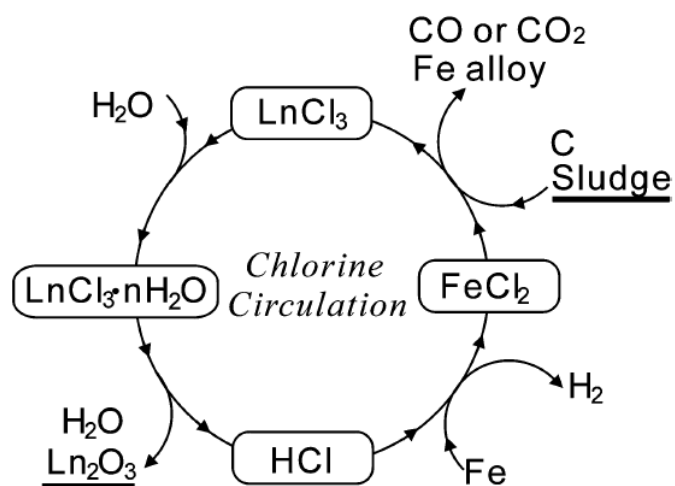
Fig. 1-7 **Separation and recovery process of Nd from Nd magnet sludge by utilizing FeCl$_2$ as an extraction agent.**[37]

recover Nd from Nd magnet sludge by chlorination with FeCl$_2$.[37] As the flowchart of this reaction shows, in principle a chlorination-based recycling process that consumes only water and carbon can be developed. Furthermore, since the only by-products are CO_2, H_2, and iron alloy, this method has a low environmental load. RE oxides produced from this process can be used as raw materials for the electrolysis of oxide in a molten fluoride.

Another chloride extraction agent method has been reported by Shirayama et al. As Fig. 1-8(a) shows, this method uses molten MgCl$_2$ to extract RE elements from Nd magnet scrap.[48] In principle, the RE elements contained in Nd magnet scrap are selectively chlorinated and dissolved into the molten salt. Since the reaction products are RE chlorides, they can be separated from the molten salt using the differences in their vapor pressures, and RE elements can be separated simultaneously. Therefore, this process is suitable for processing a large amount of Nd magnet scrap. In Fig. 1-8(b), the result of this experiment showed that about 80% of Nd and Dy are efficiently extracted as chlorides from Nd magnet scrap in a 12 h reaction.

Besides these, Itoh et al. have reported that NH$_4$Cl is another agent for extracting RE elements from Nd magnet scrap.[43] This selective chlorination was attributed to the difference in the standard enthalpies of formation between RECl$_3$ and FeCl$_2$. RE chlorides were successfully recovered in about 90% yield from powder scrap of Nd sintered magnets.

(a) Dy-containing Nd–Fe–B magnet scrap   MgCl$_2$(l)

Nd and Dy extraction by molten MgCl$_2$

NdCl$_x$(l) + DyCl$_y$(l) + Mg(l) + MgCl$_2$(l) + Fe–B(s)

Solid / liquid separation

L   S → Fe–B(s)

NdCl$_x$(l) + DyCl$_y$(l) + Mg(l) + MgCl$_2$(l)

Vacuum distillation / separation → MgCl$_2$(l, g)

NdCl$_x$(s, l, g)   DyCl$_y$(s, l, g) Mg(g)

Refining / reduction

Nd(s)   Dy(s)

(b) 1273 K (1000 °C), Molten MgCl$_2$
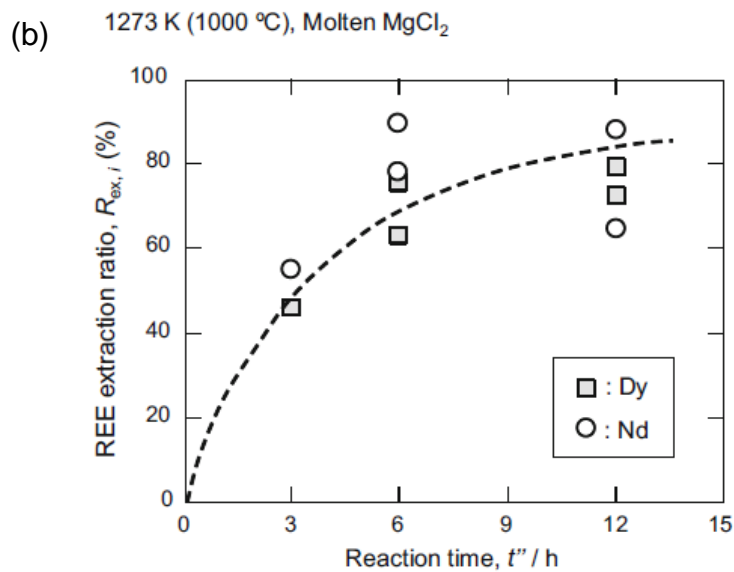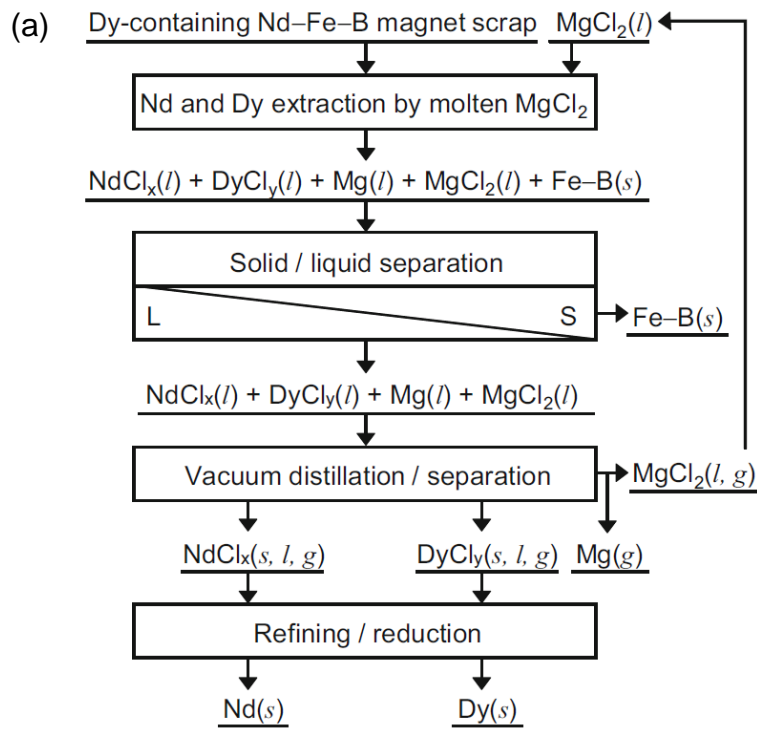
Fig. 1-8   **(a) Recovery process of RE elements from Nd magnet scrap by utilizing molten MgCl$_2$ as an extraction agent and (b) RE extraction ratio in the extraction experiment.[48]**

Fluorides can also be selected as the agent to extract RE from Nd magnet scrap. Takeda et al. developed a process as shown in Fig. 1-9(a).[22,44] In this process, the RE oxide components are first extracted from Nd magnet scrap using molten fluoride. The RE oxides are then removed by the slag/metal separation method, and the magnet alloy with low oxide concentration is recovered.
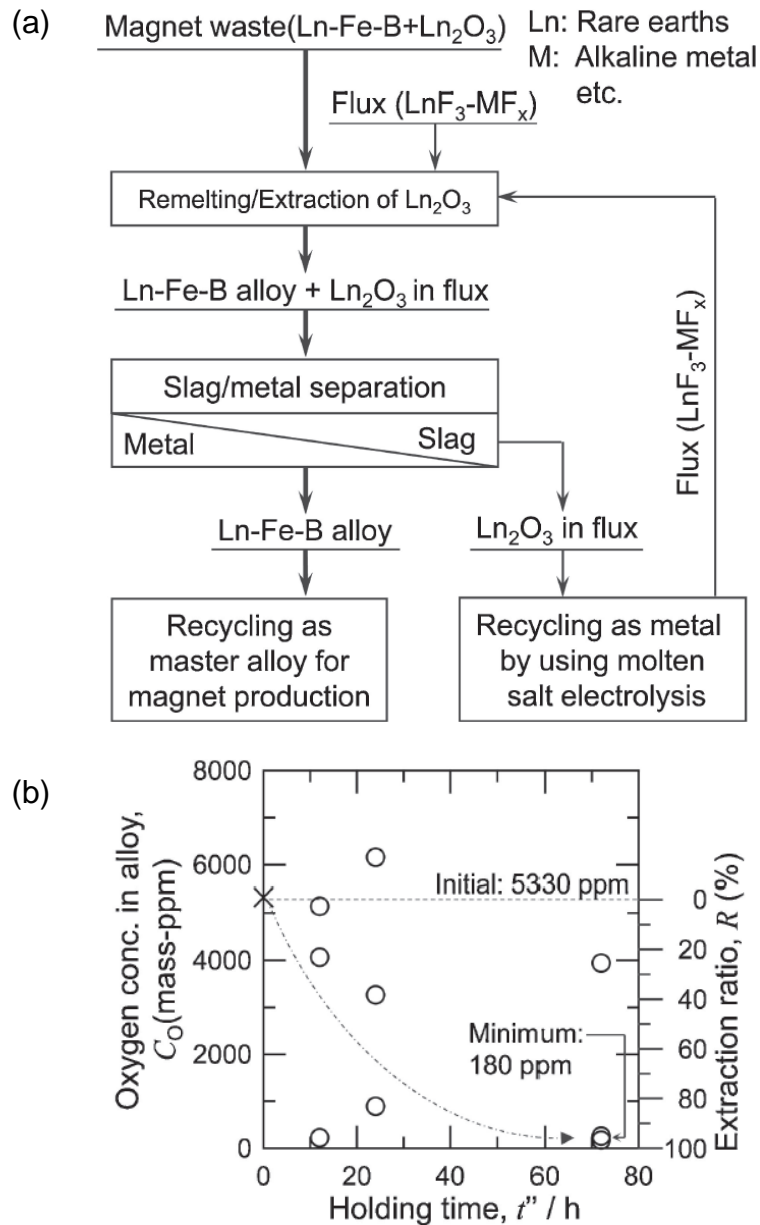
Fig. 1-9 **(a) Recovery process of RE elements from Nd magnet scrap by utilizing molten fluorides as extraction agents.[22,44] (b) Oxygen concentration of the obtained alloy determined by using infrared absorption method.[44]**

Fig. 1-9(b) shows the oxygen concentration of the obtained alloy.[44] After 60 h treatment, the concentration of oxygen is decreased. The RE oxides extracted by fluoride are recycled as RE metals by molten salt electrolysis. This process is relatively simple and consumes less energy by regenerating the Nd magnet without oxidizing.

Although all the methods described above are capable of separating RE elements from non-

RE elements, their ability to separate individual RE elements does not meet the high-precision separation requirements for magnet production. There have been several researches focusing on the separation of individual RE elements, which are explained below.

Riaño et al. reported a method that uses ionic liquid to extract and separate Nd and Dy from Nd magnet scraps.[46] Trihexyl(tetradecyl)phosphonium nitrate was employed successfully for the liquid-liquid separation of Co, Nd, and Dy. After performing the liquid-liquid separation for RE elements three times, high-purity Nd_2O_3 (99.6%) and Dy_2O_3 (99.8%) were obtained by roasting. Although the ability to separate individual RE elements is high, this process is only a modification of the conventional hydrometallurgical process.

Besides the ionic liquid extraction method, a molten salt electrolysis method is also good at individual RE element separation. Oishi et al. developed a method for separating and recovering RE elements using molten salt electrolysis and a bipolar alloy diaphragm.[49-53] Fig. 1-10(a) shows the concept diagram of this method. Nd magnet scrap is used as the anode, and the RE elements are anodically dissolved by molten salt electrolysis. Then, the RE ions are reduced on the bipolar alloy diaphragm to form a RE alloy. The formed RE alloy diffuses inside the diaphragm and anodically redissolved on the surface of the cathode compartment side of the diaphragm. Finally, the RE ions in the cathode compartment are reduced at the cathode via molten salt electrolysis, and the RE elements are electrodeposited as high-purity metals. As shown in Fig. 1-10(b), it has been experimentally shown that Dy can be selectively separated from molten LiCl–KCl containing both Dy and Nd by properly controlling the electrolysis potential.[50] In addition to the LiCl–KCl system, NaCl–KCl and $LiF–CaF_2$ systems were also investigated, however, none of them showed better separation performance than the LiCl–KCl system.[51,52] This process has the advantage of being able to extract and separate RE elements simultaneously. Due to the high formation rate of $DyNi_2$ alloy, high precision and efficient RE separation can be expected. However, the durability and strength of $DyNi_2$ alloy is insufficient to perform long-term electrolysis. Several researches have been done on high-strength bipolar electrodes, yet the results have not been satisfactory.[54-57]

(a) Rapid and selective dissolution of RE
$RE_{alloy} = RE^{3+} + 3\,e^{-}$

Rapid formation of RE-TM alloy
$RE^{3+} + 3\,e^{-} = RE_{alloy}$

Bipolar electrode

Cathode

Anode

RE^{3+}

RE

RE^{3+}

RE^{3+}

Metal

RE

Selective diffusion

Scrap

Molten salt RE-TM alloy Molten salt

(b)
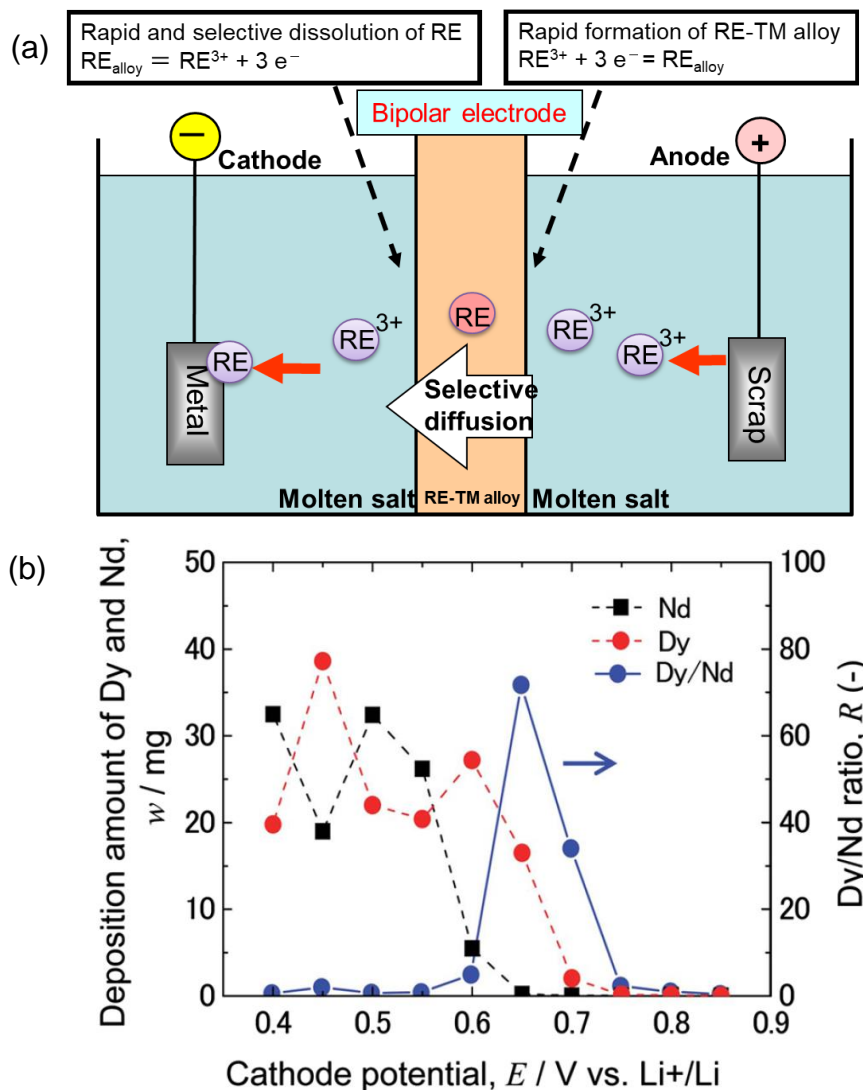
Fig. 1-10　(a) **Separation and recovery process of RE metals via molten salt electrolysis using bipolar electrode.[49-53] (b) Deposition amount of Dy and Nd, and separation ratio of Dy/Nd for RE–Ni alloys prepared in molten LiCl–KCl at 723 K.[50]**

1.5　New RE Elements Recycling Process Proposed in This Study

As described above, various researchers have reported the RE elements recycling process from Nd magnet scrap. Advantages such as fewer steps, high-purity RE obtained, and high separation ratio of Dy/Nd, etc. are theoretically available in their studies. However, there have been few studies on pyrometallurgy that have completed the entire process of separating and recovering Nd and Dy from Nd magnet scrap.

In this study, a new entire RE recycling process is proposed to separate and recover

individual RE elements from Nd magnet scrap. The concept diagram is shown in Fig. 1-11. Since this process includes three steps: (A) selective extraction, (B) selective evaporation, and (C) selective electrolysis, the name of this process is abbreviated as "SEEE process". The details of this process are described as follows.
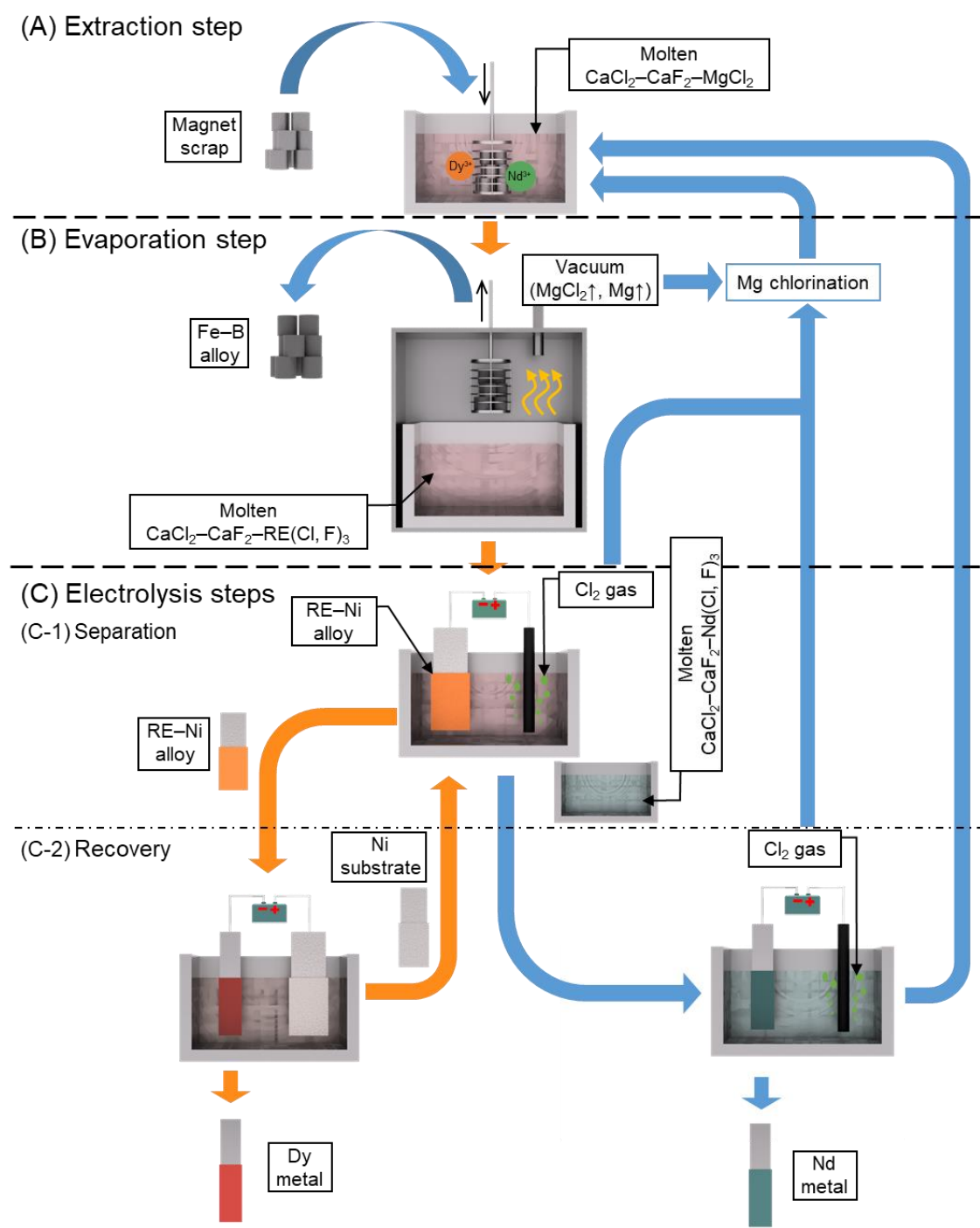
Fig. 1-11   **Concept diagram of the SEEE process that RE elements recycling from Nd magnet scrap.**

(A) Extraction step

First, Nd magnet scraps are immersed in molten $CaCl_2$–CaF_2 containing $MgCl_2$ for RE elements extraction. According to the Ellingham diagrams of chlorides and fluorides shown in Fig. 1-12,[58] the standard Gibbs energies of formation for chloride and fluoride of Mg are more negative than those of Cu, Ni, Fe, B, and Al, and more positive than those of Nd, Dy, and Ca, which means that $MgCl_2$ and MgF_2 do not react with Cu, Ni, Fe, B, and Al, but react with Nd and Dy. Thus, only RE elements are extracted into the molten $CaCl_2$–CaF_2 after the extraction step. Unlike the process reported by Shirayama et al.,[48] which used 100% $MgCl_2$ as an extraction agent, $CaCl_2$ is the main component of the molten salt in the present process and $MgCl_2$ is added with limited concentration for RE extraction. In addition, $CaCl_2$ and CaF_2 do not react with all the metals which are listed in the two diagrams. Here, Fe, B, Nd, and Dy are the main components of heat-resistant Nd magnets and Cu, Ni, and Al are usually used as the coating materials to prevent magnets from oxidation. After the RE extraction by Mg^{2+}, Cu, Ni, Fe, B, and Al are separated by removing the solid phase. Nd and Dy are extracted as chloride or fluoride into the melt by the following reaction:

$$2 \text{ RE} + 3 \text{ Mg}^{2+} \rightarrow 2 \text{ RE}^{3+} + 3 \text{ Mg} \tag{12}.$$
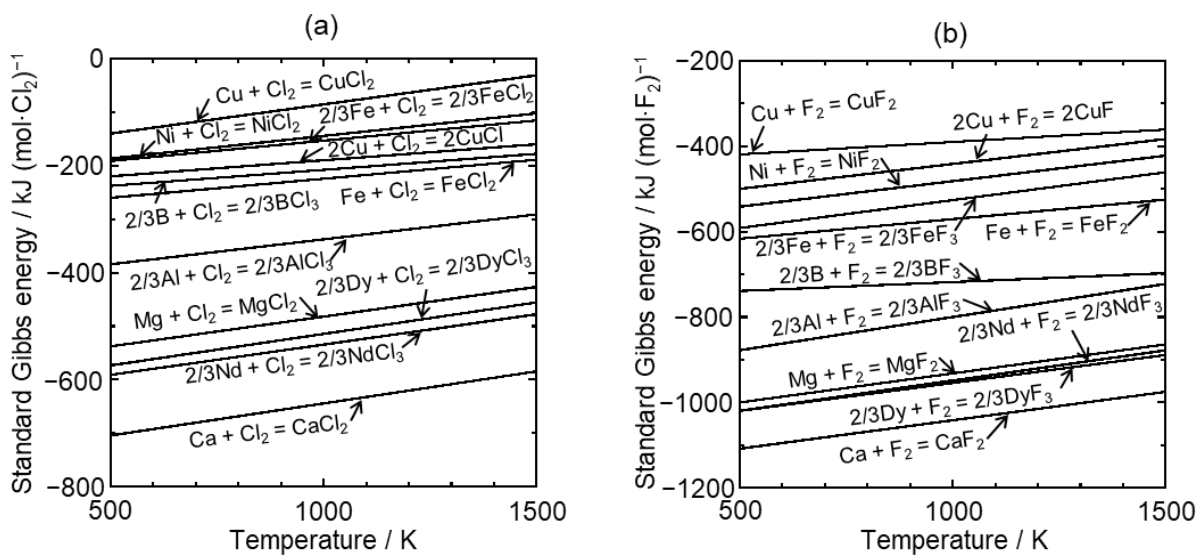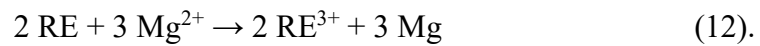
Fig. 1-12   Ellingham diagrams of (a) chlorides and (b) fluorides.[58]

(B) Evaporation step

After the RE extraction step, Mg metal, chlorides and fluorides of Mg, Nd, Dy, and Ca exist in the molten salt. Fig. 1-13 shows the calculated vapor pressures of them. The solid lines indicate the values calculated from the thermodynamic data of the liquid phase, and the broken lines indicate the values extrapolated from the thermodynamic data of the liquid phase at high temperature.[58] The vapor pressures of Mg and $MgCl_2$ are 8.6×10^{-2} atm and 2.4×10^{-3} atm at 1123 K, respectively, which are much higher than those of other substances. Therefore, Mg and $MgCl_2$ can be easily removed by vacuum. Since $NdCl_3$ and $DyCl_3$ also have relatively high vapor pressures, they may partly evaporate together with Mg and $MgCl_2$. Thus, CaF_2 is initially added into the melt to fluorinate and decrease the vapor pressures of Nd and Dy compounds. Note that the vapor pressure of MgF_2 is 1.1×10^{-8} atm at 1123 K, which is even lower than that of $CaCl_2$. In order to thoroughly remove Mg element at the Mg evaporation step, the fluorination of Mg should be avoided. The evaporated Mg and $MgCl_2$ are reused as extraction agent after chlorination treatment.
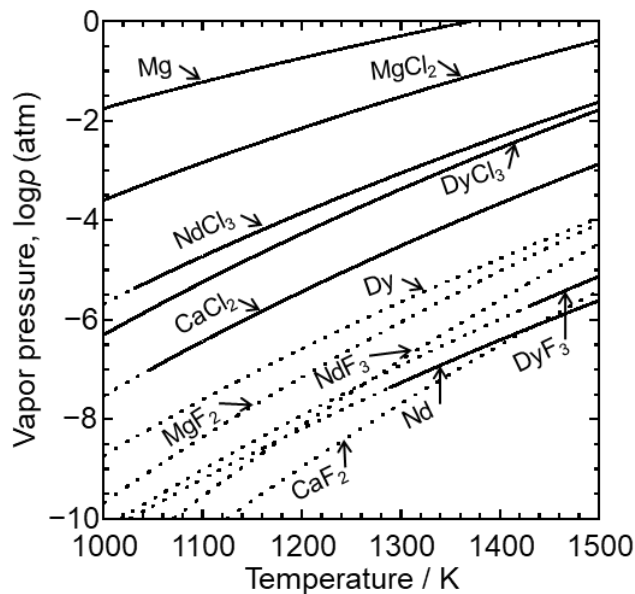
Fig. 1-13   **Vapor pressures of substances that may exist in the evaporation step.[58] The solid lines indicate the liquid state, and the broken lines indicate the extrapolation of the liquid state data from high temperature.**

(C) Electrolysis steps

Electrolysis separation is carried out in the obtained melt using Ni metal and carbon as cathode and anode, respectively. Cl_2 gas generated at the carbon anode is used to chlorinate the Mg in the previous step. Unlike the process reported by Oishi et al.,[49] in which RE–Ni alloy was used as a bipolar electrode, Ni metal is used as a cathode to form RE–Ni alloy in the present step. By controlling the electrolysis potential, a specific RE–Ni alloy with a high Dy/Nd ratio is obtained.

The formed RE–Ni alloy is transported to another melt to use as an anode, where the RE elements are selectively and anodically dissolved. Finally, the RE elements are electrodeposited as metal on a cathode. After the RE elements are dissolved out, the remaining Ni metal is reused as a cathode in the previous step. On the other hand, the molten salt after the Dy separation is regenerated by electrodeposition of the metallic Nd on a cathode. The regenerated molten salt and chlorinated Mg are reused together in the RE extraction step.

In the electrolysis step, the low strength of the RE–Ni alloy is not a fatal problem.

1.6   Outline of This Study

In order to verify the effective of SEEE process, this study investigated the RE extraction step, the Mg evaporation step, and the Dy/Nd electrolysis separation step.

In Chapter 2, as a fundamental study on the molten $CaCl_2$ system, the electrochemical behaviors of RE^{3+} (RE = Nd, Dy) were investigated in molten $CaCl_2$–$RECl_3$ (1 mol%) at 1123 K by cyclic voltammetry. Open-circuit potentiometry was used to study the two-phase coexisting potentials of RE–Ni alloys. Based on the results, several samples were prepared at the potential interval of the observed potential plateaus. The surfaces of the samples were first analyzed by X-ray diffractometry (XRD) and then the cross-sections were observed by scanning electron microscopy (SEM) and the compositions of the alloys were analyzed by energy dispersive X-ray spectroscopy (EDX).

In Chapter 3, as an extension of Chapter 2, the thermodynamic properties of RE–Ni alloys

were investigated by electrochemical method in molten $CaCl_2$ system. After collecting the temperature dependence data of the two-phase coexisting potentials, thermodynamic parameters such as the relative partial molar Gibbs energies and activities of RE and Ni were calculated. Then, the standard Gibbs energies, enthalpies, and entropies of formation for various RE–Ni alloys were calculated using the temperature dependence of relative partial molar Gibbs energies of RE and Ni. All the obtained thermodynamic data were compared with other reported values calculated by different methods.

In Chapter 4, based on the values of two-phase coexisting potentials of RE–Ni alloys obtained in Chapter 2, electrolytic separation experiments of Nd and Dy were performed in molten $CaCl_2$–$NdCl_3$ (1 mol%)–$DyCl_3$ (1 mol%) at 1123 K. First, the possibility of separation was discussed by the potential difference between the $RENi_2$ and $RENi_3$ alloys. Secondly, the potential dependences of RE–Ni alloy formation rates and Dy/Nd separation ratios were determined by preparing RE–Ni alloys at different potentials. Thirdly, since CaF_2 is added at the initial step of SEEE process, the RE–Ni alloy formation rates and the Dy/Nd separation ratios were also investigated in a CaF_2-containing melt. Finally, discussions were made on the obtained results, taking into account the effect of F^-.

In Chapter 5, the entire process of separation and recovery of Nd and Dy from Nd magnet scrap were investigated. First, different amounts of $MgCl_2$ were added as extraction agent to selectively extract RE from commercial heat-resistant Nd magnets in molten $CaCl_2$ at 1123 K. Secondly, the Nd magnet scraps before and after RE extraction and Mg evaporation were analyzed by inductively coupled plasma atomic emission spectroscopy (ICP-AES) to determine the RE extraction ratios. Thirdly, the effect of F^- on the RE evaporation ratio was also determined in the same way by adding CaF_2. Finally, electrolytic separation experiments of Dy and Nd were conducted by preparing the molten salt containing RE components similar to those in a commercial heat-resistant Nd magnet. Several samples were prepared at different potentials to investigate the suitable conditions for the enrichment of Dy using Ni electrodes. Similar experiments were also

conducted by preparing the molten salt having RE components similar to those in Nd magnets used for BEVs/HEVs motors.

Finally, Chapter 6 summarized the previous chapters. The optimal operating conditions for each step of the SEEE process were considered and a model process was proposed. Furthermore, the inadequacies of this process were discussed and improvements were provided.

References

1. G. Adachi, *SCIENCE OF RARE EARTHS*, Kagakudoujin Publishing Co., Ltd., Japan (1999).

2. *Mineral Commodity Summaries 2021* (U. S. Geological Survey, Reston, VA) 133 (2021).

3. G. G. Mosander, *Arm. Phys. (Leipzig), formerly Pogg. Ann.,* **11**, 406 (1827).

4. R. Adunka and M. V. Orna, *Carl Auer von Welsbach: Chemist, Inventor, Entrepreneur*, Springer, UK (2018).

5. The Chemical Society of Japan, *Handbook of Chemistry 7th ed.*, Maruzen Publishing Co., Ltd., Japan (2014).

6. The Electrochemical Society of Japan, *Handbook of Electrochemistry 6th ed.*, Maruzen Publishing Co., Ltd., Japan (2013).

7. E. S. Shedd, J. D. Marchant, and M. M. Wong, *Electrowinning Misch Metal from a Treated Bastnasite Concentrate*, U.S. Department of the Interior, Bureau of Mines, US (1970).

8. K. Ito, Y. Watanabe, E. Nakamura, and M. Toyoshima, *METHOD AND DEVICE FOR PRODUCING NEODYMIUM-IRON BASE ALLOY*, 61-087888 (1984).

9. T. Furuya, *MANUFACTURE OF MAGNET RAW POWDER*, 04-348004 (1992).

10. A. Kaneko, Y. Yamamoto, and C. Okada, *J. Alloy. Compd.,* **193**, 44 (1993).

11. B. Zhou, Z. Li, and C. Chen, *Minerals (Basel, Switz.),* **7**, 203/1 (2017).

12. J. R. Rumble, *CRC Handbook of Chemistry and Physics, 102nd Edition (Internet Version 2021)*, CRC Press/Taylor & Francis Group, US (2021).

13. C. K. Gupta and N. Krishnamurthy, *Extractive metallurgy of rare earths*, CRC Press, US (2004).

14. R. Halmshaw, *Industrial radiology: theory and practice*, Springer, UK (1995).

15. S. Olmschenk, K. C. Younge, D. L. Moehring, D. N. Matsukevich, P. Maunz, and C. Monroe, *Phys. Rev. A,* **76**, 052314 (2007).

16. Y. Wei and R. L. Brainard, *Advanced Processes for 193-NM Immersion Lithography*, SPIE Press, US (2009).

17. F. Daghighian, P. Shenderov, K. S. Pentlow, M. C. Graham, B. Eshaghian, C. L. Melcher, and J. S. Schweitzer, *IEEE Trans. Nucl. Sci.,* **40**, 1045 (1993).

18. J. M. D. Coey, *J. Magn. Magn. Mater.,* **248**, 441 (2002).

19. N. Jones, *Nature,* **472**, 22 (2011).

20. S. Hirosawa, Y. Matsuura, H. Yamamoto, S. Fujimura, M. Sagawa, and H. Yamauchi, *J. Appl. Phys.,* **59**, 873 (1986).

21. M. Sagawa, S. Hirosawa, H. Yamamoto, S. Fujimura, and Y. Matsuura, *Jpn. J. Appl. Phys.,* **26**, 785 (1987).

22. O. Takeda and T. H. Okabe, *Metall. Mater. Trans. E,* **1**, 160 (2014).

23. *THE RARE METAL NEWS*, Arumu Publishing Co., Ltd., Japan (2021).

24. T. Shiratori and T. Nakamura, *Shigen-to-Sozai,* **122**, 325 (2006).

25. D. Kramer, *Phys. Today,* **74**, 20 (2021).

26. W. Shi, I. Daigo, Y. Matsuno, and Y. Adachi, *J. Jpn. I Met.,* **74**, 758 (2010).

27. J. P. Rabatho, W. Tongamp, Y. Takasaki, K. Haga, and A. Shibayama, *J. Mater. Cycles Waste Manage.,* **15**, 171 (2012).

28. J.-C. G. Bunzli and V. K. Pecharsky, *Handbook on the Physics and Chemistry of Rare Earths*, North Holland, Holland (2012).

29. G. Adachi, K. Murase, K. Shinozaki, and K. Machida, *Chem. Lett.,* **21**, 511 (1992).

30. K. Murase, K. Shinozaki, Y. Hirashima, K. Machida, and G. Adachi, *J. Alloy. Compd.,* **198**, 31 (1993).

31. K. Murase, K. Machida, and G. Adachi, *J. Alloy. Compd.,* **217**, 218 (1995).

32. K. Murase, T. Ozaki, K. Machida, and G. Adachi, *J. Alloy. Compd.,* **233**, 96 (1996).

33. T. Ozaki, J. Jiang, K. Murase, K. Machida, and G. Adachi, *J. Alloy. Compd.,* **265**, 125 (1998).

34. T. Uda, K. T. Jacob, and M. Hirasawa, *Science,* **289**, 2326 (2000).

35. T. Uda, S. Komarov, and M. Hirasawa, *Mater. Trans.,* **42**, 1813 (2001).

36. Y. Xu, L. S. Chumbley, and F. C. Laabs, *J. Mater. Res.,* **15**, 2296 (2000).

37. T. Uda, *Mater. Trans.,* **43**, 55 (2002).

38. T. H. Okabe, O. Takeda, K. Fukuda, and Y. Umetsu, *Mater. Trans.,* **44**, 798 (2003).

39. T. Saito, H. Sato, S. Ozawa, J. Yu, and T. Motegi, *J. Alloy. Compd.,* **353**, 189 (2003).

40. O. Takeda, T. H. Okabe, and Y. Umetsu, *J. Alloy. Compd.,* **379**, 305 (2004).

41. M. Itoh, M. Masuda, S. Suzuki, and K.-I. Machida, *J. Alloy. Compd.,* **374**, 393 (2004).

42. O. Takeda, T. H. Okabe, and Y. Umetsu, *J. Alloy. Compd.,* **408-412**, 387 (2006).

43. M. Itoh, K. Miura, and K.-i. Machida, *J. Alloy. Compd.,* **477**, 484 (2009).

44. O. Takeda, K. Nakano, and Y. Sato, *Mater. Trans.,* **55**, 334 (2014).

45. H. J. Chae, Y. D. Kim, B. S. Kim, J. G. Kim, and T.-S. Kim, *J. Alloy. Compd.,* **586**, S143 (2014).

46. S. Riaño and K. Binnemans, *Green Chem.,* **17**, 2931 (2015).

47. T. Akahori, Y. Miyamoto, T. Saeki, M. Okamoto, and T. H. Okabe, *J. Alloy. Compd.,* **703**, 337 (2017).

48. S. Shirayama and T. H. Okabe, *Metall. Mater. Trans. B,* **49**, 1067 (2018).

49. T. Oishi, H. Konishi, T. Nohira, M. Tanaka, and T. Usui, *Kagaku Kogaku Ronbunshu,* **36**, 299 (2010).

50. H. Konishi, H. Ono, T. Nohira, and T. Oishi, *ECS Trans.,* **50**, 463 (2012).

51. T. Nohira, S. Kobayashi, K. Kondo, K. Yasuda, R. Hagiwara, T. Oishi, and H. Konishi, *ECS Trans.,* **50**, 473 (2012).

52. K. Yasuda, K. Kondo, S. Kobayashi, T. Nohira, and R. Hagiwara, *J. Electrochem. Soc.,* **163**, D140 (2016).

53. T. Awazu, T. Sugihara, M. Majima, T. Nohira, R. Hagiwara, and S. Kobayashi, *Element recovery method and element recovery apparatus*, US 10309022 B2 (2019).

54. Y. Watanabe, Y. Norikawa, K. Yasuda, and T. Nohira, *Mater. Trans.,* **60**, 379 (2019).

55. K. Yasuda, T. Enomoto, Y. Watanabe, T. Oishi, and T. Nohira, *Mater. Trans.,* **61**, 2329 (2020).

56. K. Yasuda, T. Oishi, T. Kagotani, K. Kawaguchi, M. Yaguchi, T. Enomoto, and T. Nohira, *J.*

Alloy. Compd., **889**, 161605 (2021).

57. K. Kawaguchi and T. Nohira, *J. Electrochem. Soc.,* **168**, 082503 (2021).

58. A. Roine and P. Kobylin, *HSC Chemistry®,* ver 9, Outotec Information Center, Pori, Finland (2016).

Chapter 2

Electrochemical Formation of RE–Ni (RE = Nd, Dy) Alloys in Molten CaCl₂–RECl₃

2.1   Introduction

In this chapter, the electrochemical behavior of RE^{3+} (RE = Nd, Dy) ions at Mo and Ni electrodes was investigated by cyclic voltammetry. Then, the electrochemical formation potential of each RE–Ni alloy was estimated by open-circuit potentiometry. After that, the formed RE–Ni alloy phases were identified by XRD, and cross-sections of the alloy samples were observed by SEM and analyzed by EDX. Finally, the electrochemical formation potentials of various RE–Ni alloys were summarized and compared with each other.

2.2   Experimental

As shown in Fig. 2-1, 300 g of $CaCl_2$ powder (Kojundo Chemical Laboratory Co., Ltd., 99%) loaded in a graphite crucible (Sanko Co., Ltd., IG-110, inner diameter: 90 mm, height: 120 mm) was first dried in a vacuum oven at 453 K for 72 h, and then placed at the bottom of a stainless-steel vessel in an airtight Kanthal container for further drying under vacuum at 773 K for 24 h. After drying, the temperature was raised to the experimental value of 1123 K. All the experiments were carried out under the dry argon atmosphere in a glove box. One mol-percent of $RECl_3$ powder (Kojundo Chemical Laboratory Co., Ltd., 99.9%) was added directly into the molten salt. Two types of working electrodes were used, flag electrodes (diameter: 3.0 mm, thickness: 0.1 mm, lead wire diameter: 0.2 mm) for the cyclic voltammetry and open-circuit potentiometry, and plate
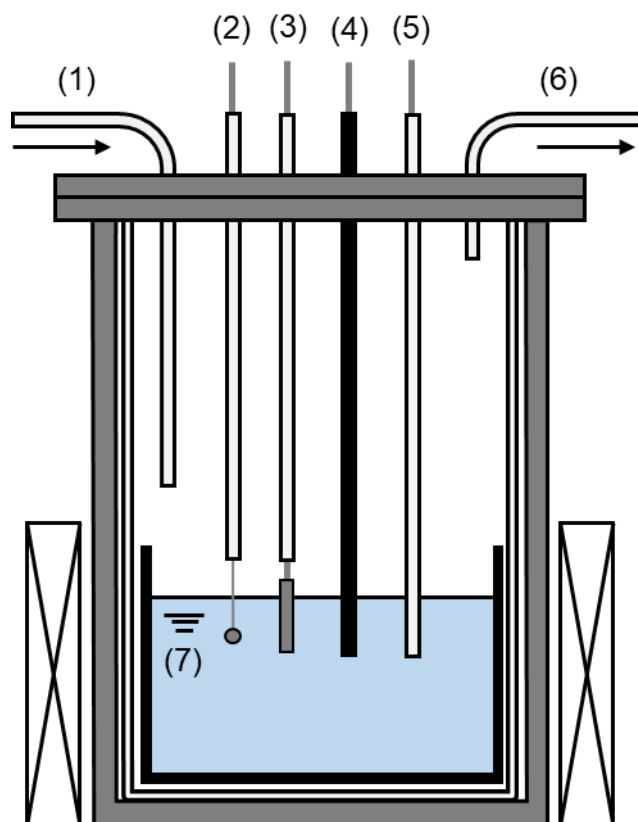
Fig. 2-1   **Schematic drawing of the experimental apparatus for molten $CaCl_2$–$RECl_3$ systems. (1) Ar gas inlet, (2) working electrode (Mo or Ni), (3) working electrode (Ni plate), (4) counter electrode (carbon rod), (5) reference electrode (Ni^{2+}/Ni), (6) gas outlet, and (7) $CaCl_2$ molten salt (1.0 mol% $RECl_3$ added).**

electrodes (width: 5 mm × length: 20 mm × thickness: 0.1 mm) for the sample preparation. The working electrode materials were Ni (Nilaco Corp., >99%) and Mo (Nilaco Corp., >99%). A Ni wire immersed in molten $CaCl_2$ containing 1.0 mol% $NiCl_2$ (Alfa Aesar Corp., 98%), set in a mullite tube (Nikkato Corp., outer diameter: 6 mm × inner diameter: 4 mm × length: 500 mm, 56% Al_2O_3–40% SiO_2; HB grade) was used as the reference electrode. All the potentials in this study were calibrated with reference to a dynamic Ca^{2+}/Ca reference electrode, which was prepared by electrodepositing Ca metal on a Mo flag electrode at sufficiently large cathodic current densities (>2 A cm^{-2}). A carbon rod (Sanko Co., Ltd., diameter: 7 mm × length: 520 mm) was used as the counter electrode. An electrochemical measurement system (Hokuto Denko Corp., HZ-7000) connected to a computer was used for the entire measurements.

The alloy samples prepared by the potentiostatic electrolysis were usually covered with the solidified salts. Before the analysis, the samples were washed with deionized water to remove the salts and then rinsed by ethanol (FUJIFILM Wako Pure Chemical Corp., 99.5%). After this treatment, XRD (Rigaku Corp., Ultima IV) analysis was carried out with a diffractometer using Cu-$K\alpha$ radiation ($\lambda = 0.15418$ nm) at 40 kV and 40 mA. Subsequently, the samples were embedded in resin and polished with the emery papers (#320 and #600), polycrystalline diamond suspensions (3 μm and 9 μm), and buffing compound (Micro Polish II, 0.3 μm, Buehler), successively. After exposing the cross-section, the samples were analyzed by SEM (Thermo Fisher Scientific Inc., Phenom Pro Generation 5) and EDX (Thermo Fisher Scientific Inc., SE1200–8001).

2.3 Results and Discussion

2.3.1 Cyclic Voltammetry

2.3.1.1 CaCl$_2$–NdCl$_3$ System

A Mo electrode was used to measure the potentials of Ca^{2+}/Ca and Nd^{3+}/Nd, because there are no alloys in binary Mo–Ca and Mo–Nd systems at 1123 K.[1] Fig. 2-2(a) shows the cyclic voltammogram comparison for a Mo electrode in molten CaCl$_2$ before (black curve) and after (red curve) the addition of 1.0 mol% NdCl$_3$. For blank measurement, only a pair of rapid cathodic and anodic current are observed, which should correspond to the deposition/dissolution of Ca. After NdCl$_3$ addition, besides the currents assigned to Ca deposition/dissolution, a new anodic current increase at approximately 0.3 V (vs. Ca^{2+}/Ca). Based on Mo properties, the current should be interpreted as the dissolution of Nd metal. The cathodic current of the Nd deposition may be overcome by the rapid increase in the cathodic current due to the formation of Ca metal fog which is a phenomenon that the formed Ca metal has an activity smaller than unity, because Ca metal dissolves into molten CaCl$_2$ up to 4 mol%.[2] Fig. 2-2(b) presents the cyclic voltammograms measured for a Ni electrode under the same conditions. For blank measurements, the Ca metal fog formation current is observed. After NdCl$_3$ addition, the cathodic currents increase from
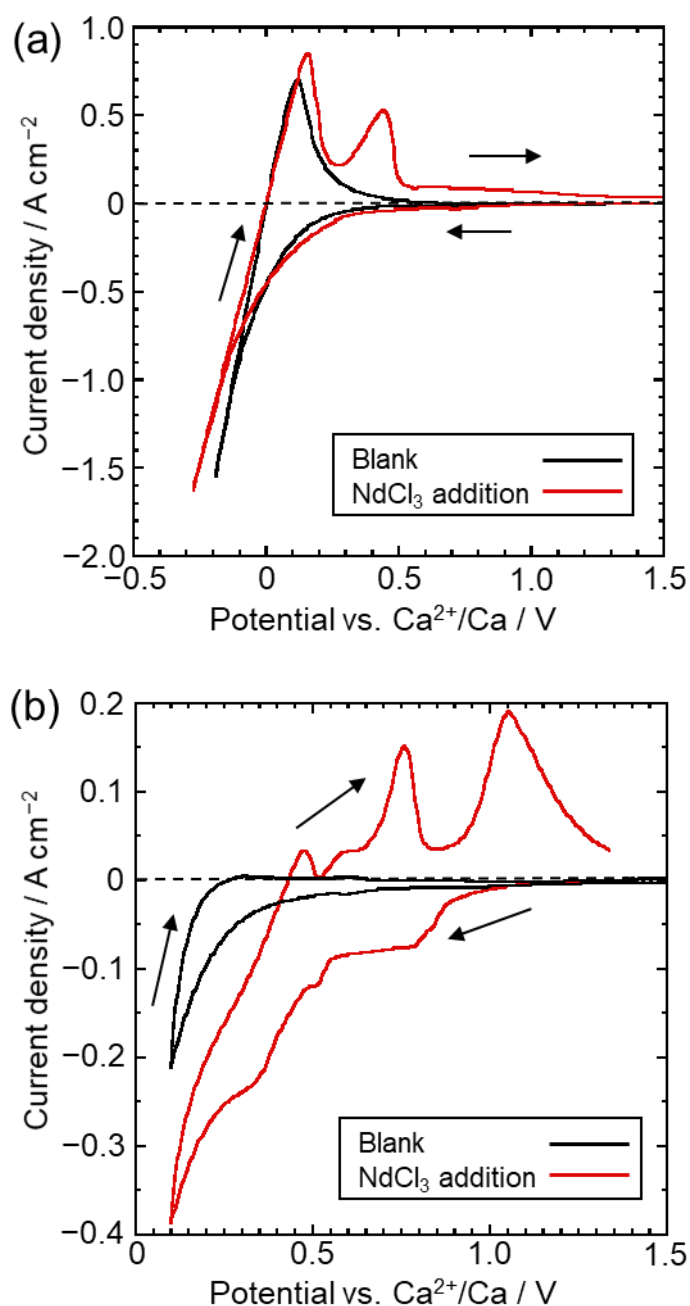
Fig. 2-2 Cyclic voltammograms for a (a) Mo and (b) Ni flag electrode in molten CaCl₂ before and after the addition of 1.0 mol% NdCl₃ at 1123 K. Scan rate: 100 mV s⁻¹.

approximately 1.0 V suggesting the formation of Nd–Ni alloys. The Nd–Ni system phase diagram (Fig. 2-3) shows four intermetallic compounds ($NdNi_2$, $NdNi_3$, Nd_2Ni_7, and $NdNi_5$) and a liquid alloy exist at 1123 K.[3] The four Nd–Ni alloys are expected to form electrochemically. Several anodic peaks/shoulders are observed under an anodic sweep, which should be caused by Nd dissolution from the different Nd–Ni alloys.
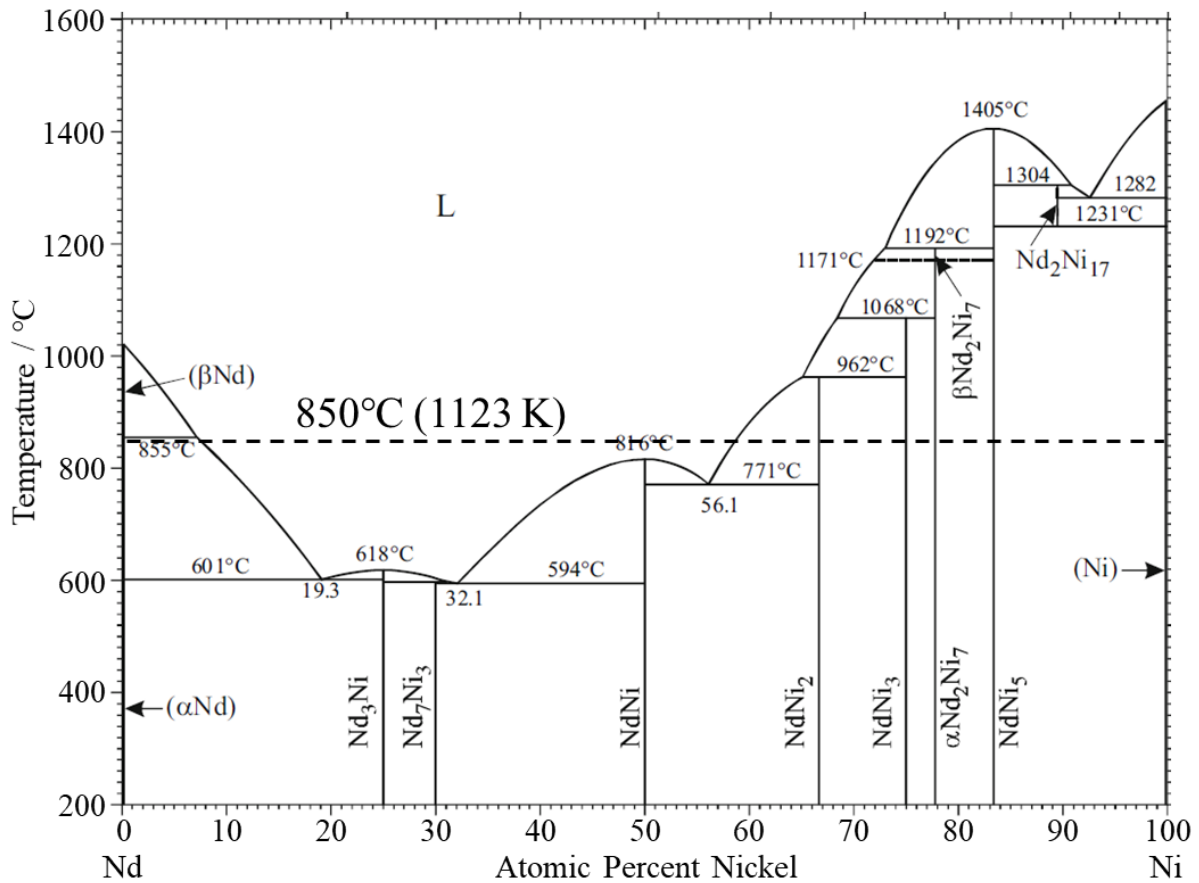
Fig. 2-3   Binary phase diagram for the Nd–Ni system.[3]

2.3.1.2 CaCl$_2$–DyCl$_3$ System

As for the DyCl$_3$ addition system, the obtained cyclic voltammograms for a Mo electrode before (broken curve) and after (solid curve) the addition of 1.0 mol% DyCl$_3$ are shown in Fig. 2-4(a). In the blank measurement, cathodic currents rapidly increase from approximately 0.2 V. These currents possibly correspond to the formation of Ca metal fog. After the DyCl$_3$ addition, a sharply rising cathodic current and an anodic current peak are observed at approximately 0.3 V. Since no Mo–Dy alloys exist at 1123 K, they should be interpreted as the deposition and dissolution of Dy metal, respectively. Fig. 2-4(b) presents the cyclic voltammograms for a Ni electrode before and after the 1.0 mol% DyCl$_3$ addition. For the reference, the voltammogram for Mo electrode in DyCl$_3$ addition system is also plotted (broken curve). Before the addition of DyCl$_3$, the voltammogram for Ni electrode (solid black curve) is almost the same as the Mo electrode in Fig. 2-4(a), indicating
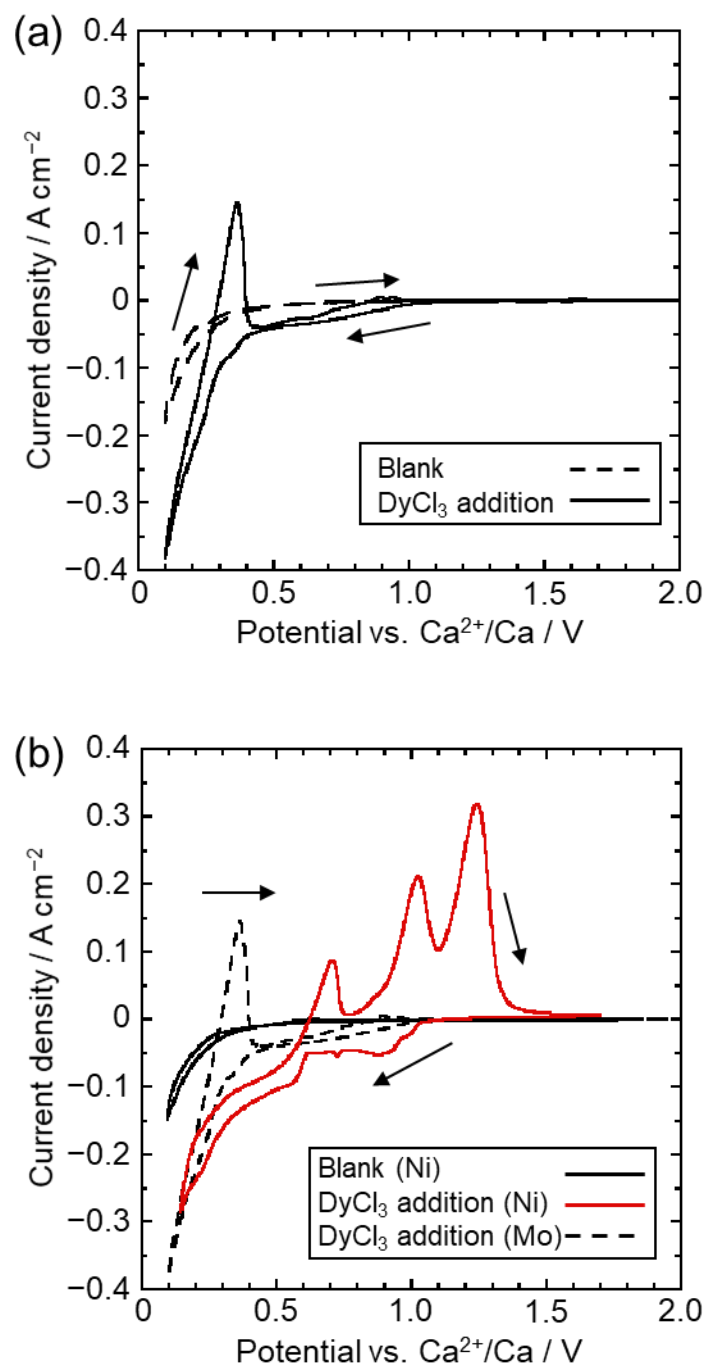
Fig. 2-4 Cyclic voltammograms for a (a) Mo and (b) Ni flag electrode in molten CaCl₂ before and after the addition of 1.0 mol% DyCl₃ at 1123 K. Scan rate: 20 mV s⁻¹.

that the cathodic currents increasing from 0.2 V at Ni electrode should also correspond to the formation of Ca metal fog. After the DyCl₃ addition (solid red curve), cathodic currents increase from 1.0 V, which suggests the start of Dy–Ni alloys formation. From approximately 0.6 V, a further increase in cathodic current is observed, suggesting the formation of Dy–Ni alloys having higher
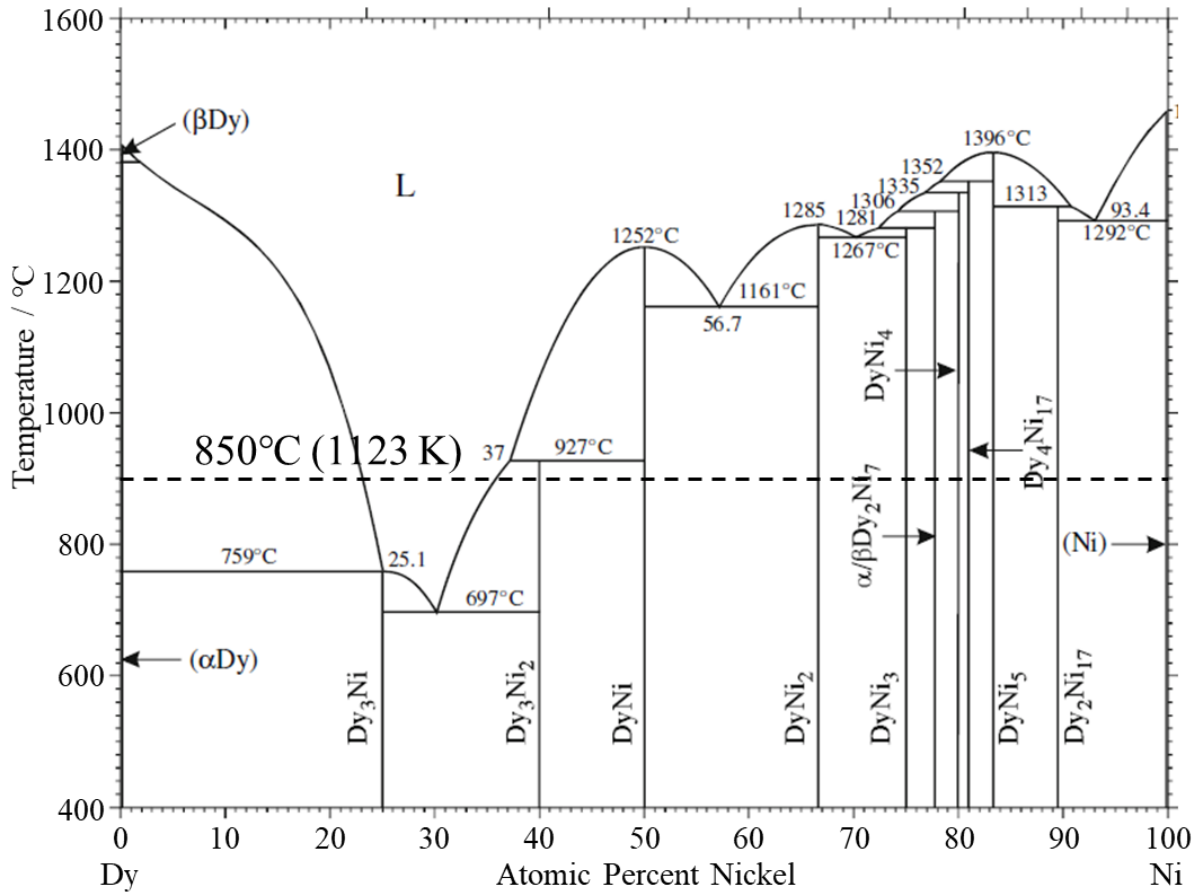
Fig. 2-5   Binary phase diagram for the Dy–Ni system.[4]

Dy concentration. According to the phase diagram of the Dy–Ni system shows in Fig 2-5,[4] there are nine intermetallic compounds (Dy_3Ni_2, $DyNi$, $DyNi_2$, $DyNi_3$, Dy_2Ni_7, $DyNi_4$, Dy_4Ni_{17}, $DyNi_5$, and Dy_2Ni_{17}) and liquid alloy exist at 1123 K. These Dy–Ni alloys were expected to form by the electrochemical reaction in this study. In contrast, several anodic peaks observed in the anodic sweep possibly correspond to the dissolution of Dy from the formed different Dy–Ni alloys.

2.3.2   Open-circuit Potentiometry

2.3.2.1   CaCl₂–NdCl₃ System

From the previous study,[5-7] OCP was selected as the appropriate method to determine the equilibrium potential of RE^{3+}/RE and the two-phase coexisting potentials of RE–Ni alloys. To determine the Nd^{3+}/Nd potential, the measurement was conducted using a Mo electrode in molten

CaCl$_2$ before and after the addition of NdCl$_3$. As shown in Fig. 2-6, after galvanostatic electrolysis at -1.0 A cm^{-2} for 30 s, compared with blank measurement, a new potential plateau appears at 0.27 V after the NdCl$_3$ addition. This corresponds to the equilibrium potential of Nd^{3+}/Nd. According to the binary phase diagram of the Ca–Ni system,[8] Ca–Ni alloys exist at 1123 K. To find the potential of Ca–Ni alloy formation, the measurement was conducted for a Ni electrode in molten CaCl$_2$. Fig. 2-7 shows the open-circuit potentiogram after galvanostatic electrolysis at -2.0 A cm^{-2} for 30 s. Only one potential plateau maintained at 0.13 V over 50 s should correspond to the formation potential of Ca–Ni alloy. To avoid the influence of Ca–Ni alloy and Nd metal, OCP measurement for a Ni electrode was conducted after the formation of Nd–Ni alloys at 0.30 V for 150 s. As shown in Fig. 2-8, three potential plateaus are observed at 0.48, 0.68, and 0.95 V, which are determined from the smallest differential coefficient points. These plateaus correspond to the two-phase coexisting state potential of different Nd–Ni alloys.
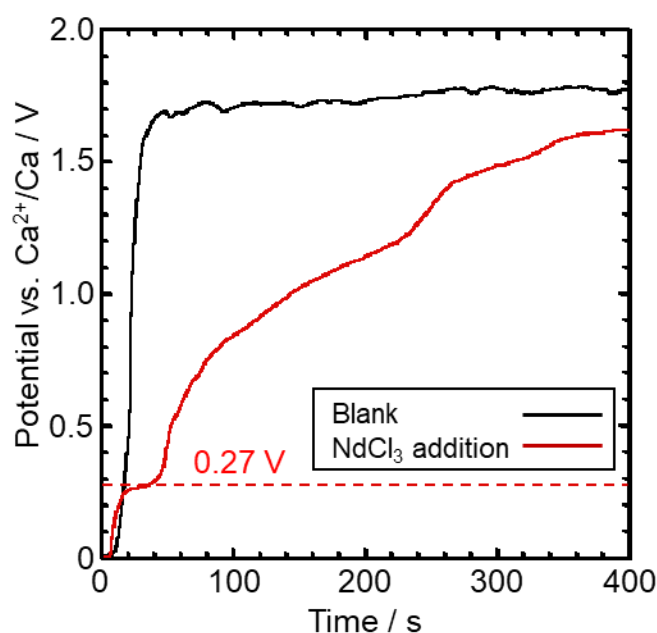
Fig. 2-6   **Open-circuit potentiograms for a Mo flag electrode after galvanostatic electrolysis at -1.0 A cm^{-2} for 30 s in molten CaCl$_2$ before and after the addition of 1.0 mol% NdCl$_3$ at 1123 K.**
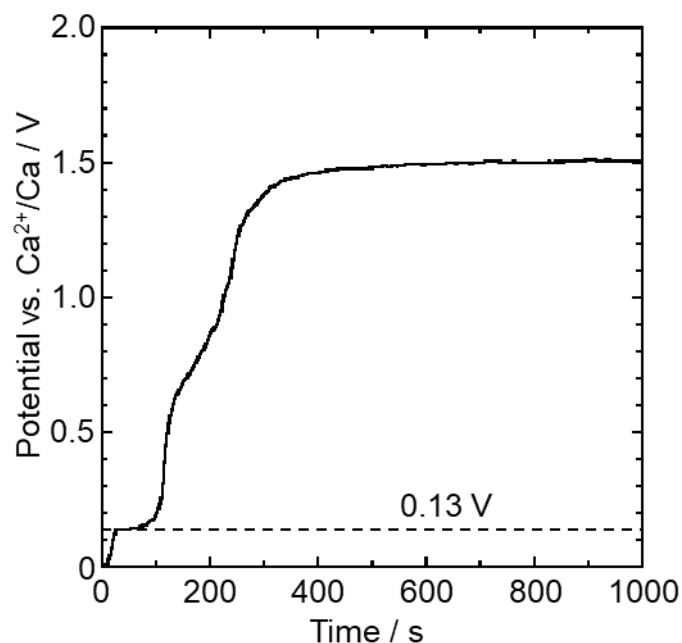
Fig. 2-7 Open-circuit potentiogram for a Ni flag electrode after galvanostatic electrolysis at −2.0 A cm^{-2} for 30 s in molten CaCl$_2$ at 1123 K.
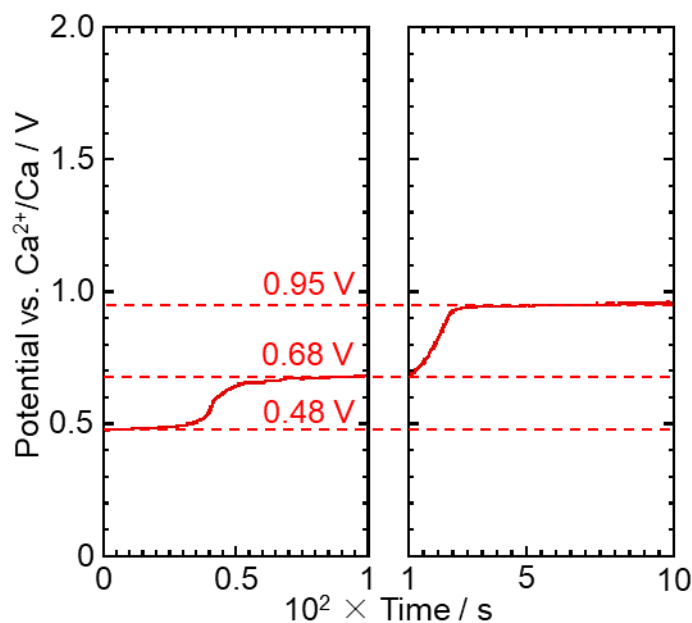
Fig. 2-8 Open-circuit potentiogram at a Ni flag electrode after potentiostatic electrolysis at 0.30 V for 150 s in molten CaCl$_2$–NdCl$_3$ (1.0 mol%) at 1123 K.

2.3.2.2 CaCl$_2$–DyCl$_3$ System

To elucidate the potential of Dy^{3+}/Dy and each of the two-phase coexisting state of Dy–Ni alloys, a Mo and a Ni electrode were used in CaCl$_2$–DyCl$_3$ (1.0 mol%) for OCP measurements. A black curve in the left part of Fig. 2-9 shows the result corresponding to the Mo electrode exhibiting
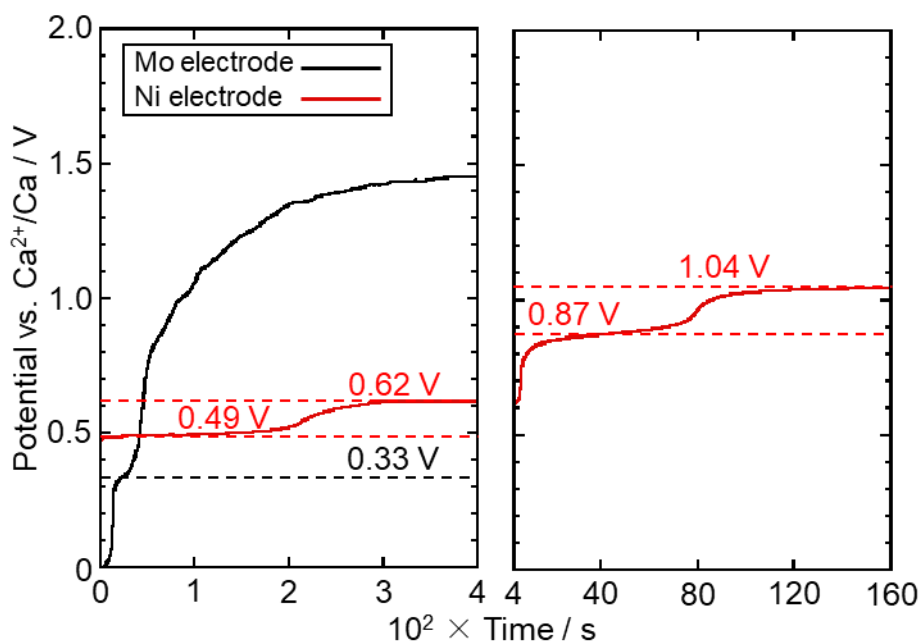
Fig. 2-9 Open-circuit potentiograms at Mo and Ni flag electrodes in molten CaCl$_2$–DyCl$_3$ (1.0 mol%) at 1123 K. Electrolysis condition: −0.50 V for 30 s (Mo), 0.25 V for 15 min (Ni).

only one potential plateau at 0.33 V, after the potentiostatic electrolysis at −0.50 V for 30 s. Since Mo does not form any intermetallic compounds with Dy at 1123 K, the observed potential should be interpreted as the Dy^{3+}/Dy potential. For the Ni electrode, the measurement condition was selected at 0.25 V for 15 min to avoid the influence of Ca–Ni alloy. Fig. 2-9 shows the result for the Ni electrode (red curves) exhibiting four potential plateaus at 0.49, 0.62, 0.87, and 1.04 V. The result suggests that the potential plateaus at 0.62, 0.87, and 1.04 V are related to the three anodic peaks shown in Fig. 2-4(b). The four potential plateaus possibly correspond to the potentials of two-phase coexisting states of different Dy–Ni alloys.

2.3.3 Preparation and Characterization of RE–Ni alloys

2.3.3.1 Nd–Ni Alloys

To obtain more information on Nd–Ni alloys formation, samples were prepared by potentiostatic electrolysis at 0.30, 0.50, 0.80, and 1.00 V.

Fig. 2-10 shows (a) a cross-sectional SEM image with EDX analysis and (b) an XRD pattern,

Fig. 2-10 **(a) A cross-sectional SEM image with EDX analysis and (b) an XRD pattern of the sample obtained by potentiostatic electrolysis with a Ni electrode at 0.30 V for 15 min in a molten $CaCl_2$–$NdCl_3$ (1.0 mol%) system at 1123 K.**

for the sample prepared by the potentiostatic electrolysis at 0.30 V for 15 min. Three layers are observed through the cross-sectional SEM image. According to the EDX analysis, the atomic composition for Nd:Ni at point (1), (2), and (3) are Nd:Ni = 0:100, 26.50:73.50, and 33.87:66.13, respectively. The three layers would correspond to Ni, $NdNi_3$, and $NdNi_2$. The different alloy layers

40

were formed due to the varying Nd diffusion rates. The XRD pattern confirmed that the sample has a $NdNi_2$ surface layer. As $NdNi_2$ is formed from the highest Nd concentrated Nd–Ni alloy, it is the thermodynamically stable phase at 0.30 V.

Fig. 2-11 shows the analysis of the sample electrolyzed at 0.50 V for 60 min. Fig. 2-11(a) shows the cross-sectional SEM image and EDX analysis with two alloy layers on the Ni substrate.

Fig. 2-11 **(a) A cross-sectional SEM image with EDX analysis and (b) an XRD pattern of the sample obtained by potentiostatic electrolysis with a Ni electrode at 0.50 V for 60 min in a molten $CaCl_2$–$NdCl_3$ (1.0 mol%) system at 1123 K.**

41

(2) The Nd:Ni composition of the middle layer is 18.02:81.98, which is close to the $NdNi_5$ composition. (3) The outer alloy layer has an Nd:Ni composition of 25.85:74.15, which is similar to the $NdNi_3$ composition. Fig. 2-11(b) shows the obtained XRD pattern, which confirms the $NdNi_3$ outer alloy layer. The XRD pattern for the $NdNi_3$ phase was calculated by the PowderCell program using the reported crystallographic parameters. Lattice parameters for $NdNi_3$ were reported by A.V. Virkar and A. Raman[9] and positional parameters of $PuNi_3$ atoms, which are isostructural with $NdNi_3$ were reported by D.T. Cromer and C.E. Olsen.[10] Finally, the thermodynamically stable phase at 0.50 V is confirmed as $NdNi_3$. From the analysis results of samples prepared at 0.30 and 0.50 V, the potential plateau at 0.48 V in Fig. 2-8 corresponds to the two-phase coexisting state of $NdNi_2$ and $NdNi_3$.

To confirm the coexisting phase at 0.68 V in Fig. 2-8, the sample was prepared at 0.80 V for 60 min. Fig. 2-12 shows the (a) cross-sectional SEM image with EDX analysis and (b) an XRD pattern for the sample. A thin alloy layer is observed in the SEM image. The EDX (Nd:Ni = 17.56:82.44 at point (2) and 17.92:82.08 at point (3)) and XRD analyses confirmed the $NdNi_5$ alloy layer. As the alloy layer thickness is below 5 μm, XRD peaks assigned to the Ni substrate are observed in the XRD pattern. Thus, $NdNi_5$ is the thermodynamically stable phase at 0.80 V, and the potential plateau at 0.68 V corresponds to the two-phase coexisting state of $NdNi_3$ and $NdNi_5$.

Finally, to confirm that the two-phase coexisting state of Nd–Ni and Ni metal is shown by the plateau at 0.95 V in Fig. 2-8, the sample was prepared at 1.00 V for 60 min. Fig. 2-13(a) and (b) show a cross-sectional SEM image with EDX analysis and an XRD pattern for the sample, respectively. These analyses did not show the formation of an alloy. Thus, Ni is the thermodynamically stable phase at 1.00 V and the potential plateau at 0.95 V in Fig. 2-8 corresponds to the two-phase coexisting state of $NdNi_5$ and Ni.

Upon comparison with previous studies, which confirmed the Nd–Ni alloy formation,[6-7,11] the Nd_2Ni_7 formation was not confirmed. It might be caused by the slow formation rate of Nd_2Ni_7 and the high transition rate of $NdNi_5$. The $NdNi_2$ formation rate is over 100 μm h^{-1}, which is

Fig. 2-12 **(a) A cross-sectional SEM image with EDX analysis and (b) an XRD pattern of the sample obtained by potentiostatic electrolysis with a Ni electrode at 0.80 V for 60 min in a molten CaCl$_2$–NdCl$_3$ (1.0 mol%) system at 1123 K.**

equivalent to that of the fluoride system at the same temperature.[6] Based on the aforementioned results, the three potential plateaus at 0.48, 0.68, and 0.95 V obtained during the OCP measurement correspond to the two-phase coexisting states of (NdNi$_2$ + NdNi$_3$), (NdNi$_3$ + NdNi$_5$), and (NdNi$_5$ + Ni), respectively.

(a)

(1)
+

10 µm

EDX (at%)	(1) Nd : Ni = 0 : 100

(b)

Diffraction intensity / a.u.

O Ni
PDF: 00-003-1051

2θ / deg. (Cu-Kα)
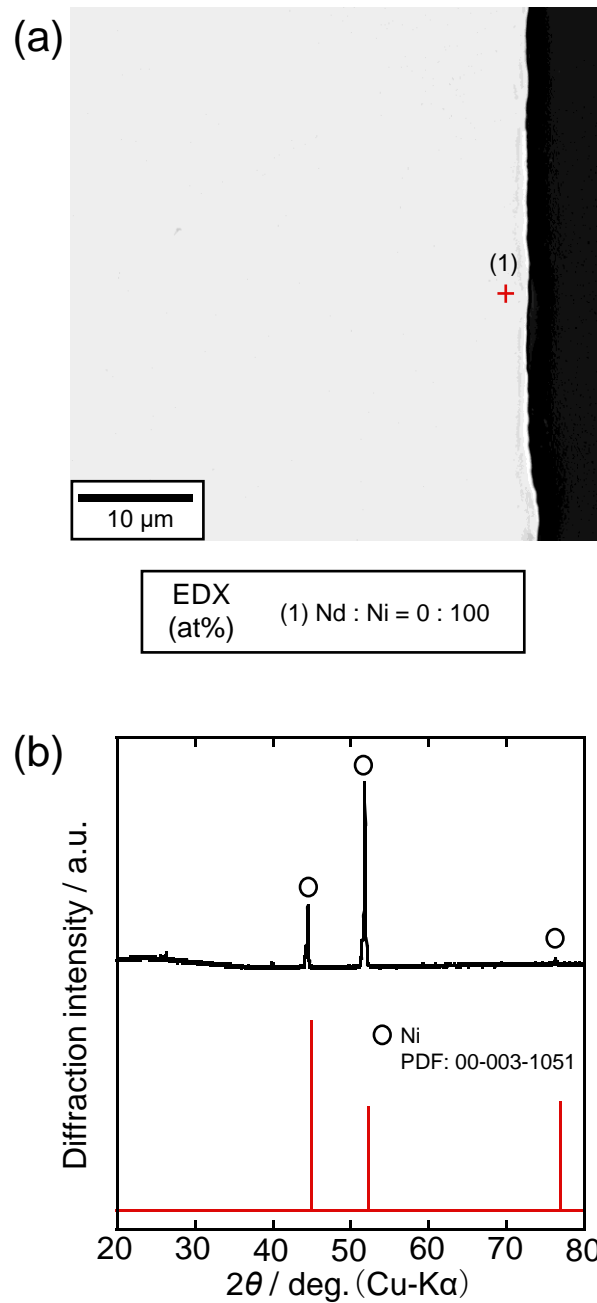
Fig. 2-13   **(a) A cross-sectional SEM image with EDX analysis and (b) an XRD pattern of the sample obtained by potentiostatic electrolysis with a Ni electrode at 1.00 V for 60 min in a molten CaCl₂–NdCl₃ (1.0 mol%) system at 1123 K.**

2.3.3.2   Dy–Ni Alloys

To confirm each of the two-phase coexisting state, Dy–Ni alloy samples were prepared by the potentiostatic electrolysis at 0.40, 0.50, 0.70, 0.90, and 1.20 V, respectively.

Fig. 2-14 shows (a) a cross-sectional SEM image obtained using EDX analysis, and (b) an
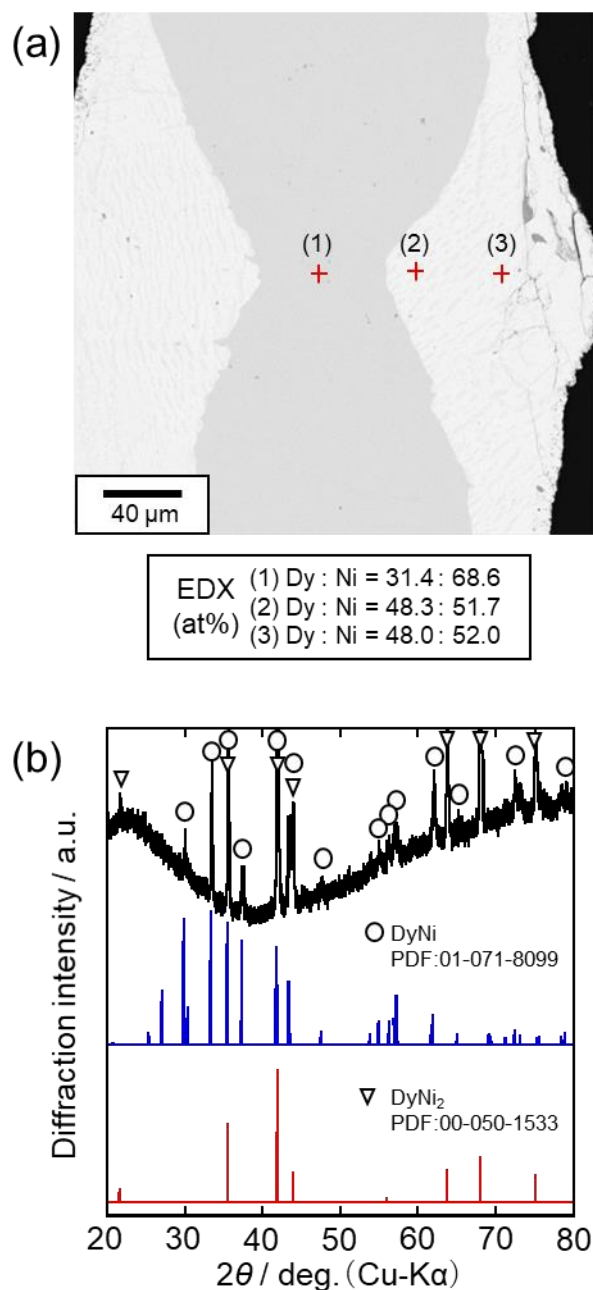
Fig. 2-14 **(a) A cross-sectional SEM image with EDX analysis and (b) an XRD pattern of the sample obtained by potentiostatic electrolysis with a Ni electrode at 0.40 V for 60 min in a molten CaCl₂–DyCl₃ (1.0 mol%) system at 1123 K.**

XRD pattern for the sample prepared by the potentiostatic electrolysis at 0.40 V for 60 min. Non-uniform inner and outer layers were found through the cross-section. EDX analysis revealed the atomic composition to be Dy:Ni = 31.4:68.6 at point (1) of the inner layer, indicating the formation of DyNi$_2$; while at points (2) and (3) of outer layer, the compositions were Dy:Ni = 48.3:51.7 and

48.0:52.0, respectively, which indicated that the finally formable alloy at 0.40 V is DyNi. The existence of inner $DyNi_2$ layer would be caused by the fast formation rate of $DyNi_2$ and the slow formation rate of DyNi. The XRD pattern of the sample confirmed the formations of both DyNi and $DyNi_2$.

To confirm the fast formation rate of $DyNi_2$ and the slow formation rate of DyNi, the sample was prepared at the same potential of 0.40 V for 15 min. Fig. 2-15 shows (a) a cross-sectional SEM image and (b) an XRD pattern of the sample. Uniform alloy layer having a thickness of approximately 50 μm was observed. The only existing of $DyNi_2$ alloy was confirmed from the EDX and XRD results. Therefore, the formation rate of $DyNi_2$ is much faster than that of DyNi.

Fig. 2-16 shows (a) a cross-sectional SEM image with EDX analysis and (b) an XRD pattern for the sample electrolyzed at 0.50 V for 60 min. The Ni plate substrate electrode was uniformly and completely alloyed. The thickness of the plate increased from the original value of 100 μm to 200 μm. According to the EDX analysis, compositions at point (1), (2) and (3) were Dy:Ni = 30.7:69.3, 29.7:70.3 and 30.5:69.5, respectively, indicating the uniform alloy is $DyNi_2$. Besides, the XRD analysis indicated that only $DyNi_2$ alloy exists. According to these results, $DyNi_2$ is the thermodynamically stable phase at 0.50 V. The growth rate of $DyNi_2$ alloy is over 100 μm h^{-1}, similar to that in molten $LiF-CaF_2$ at 1123 K.[12]

From the previous studies of electrochemical formation of Dy–Ni alloys in molten salts that the formation rates of Dy-poor phases such as $DyNi_3$ and $DyNi_5$ are very slow.[12-14] However, once an Dy-rich alloy such as $DyNi_2$ is formed as the starting electrode, the formation of the Dy-poor phases, namely, the anodic dissolution of Dy metal from the Dy-rich alloy, becomes considerably faster. Hence, in this study, based on the result at 0.50 V, electrodes with Dy-rich alloy were prepared by potentiostatic electrolysis at 0.50 V for 15 min, as the first step. Subsequently, Dy-poor phases were produced by the anodic dissolution of Dy from the Dy-rich phase at 0.70, 0.90, and 1.20 V for 60 min, as the second step.

As shown in Fig. 2-17, the reaction of the first step was investigated by, (a) a cross-sectional
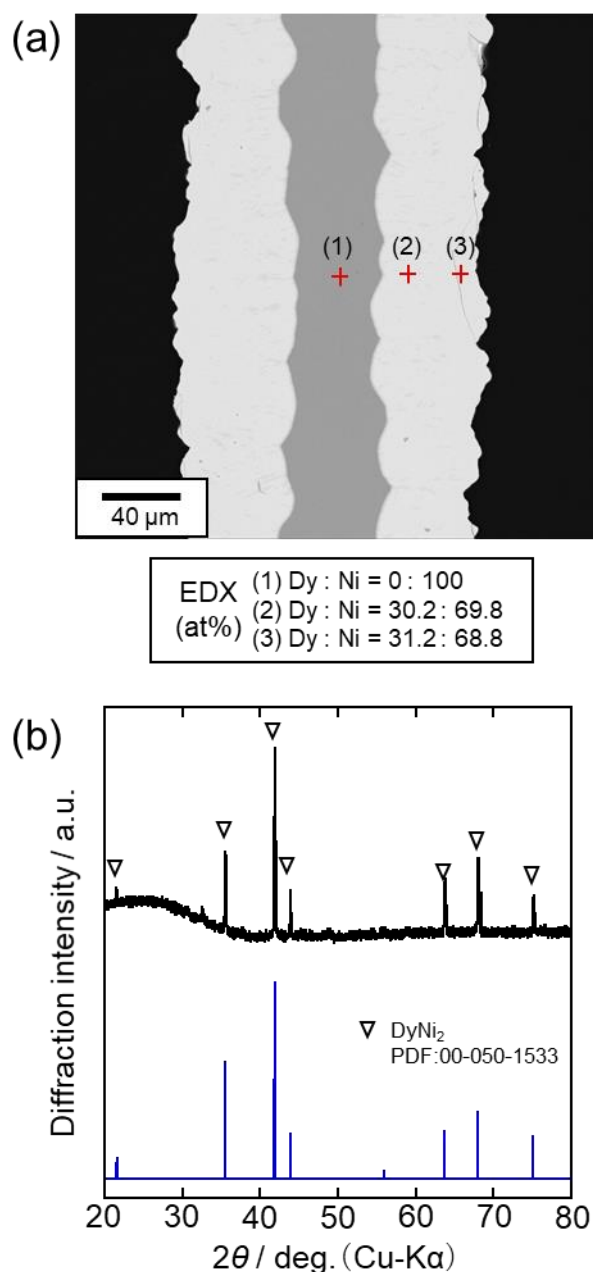
Fig. 2-15   **(a) A cross-sectional SEM image with EDX analysis and (b) an XRD pattern of the sample obtained by potentiostatic electrolysis with a Ni electrode at 0.40 V for 15 min in a molten CaCl$_2$–DyCl$_3$ (1.0 mol%) system at 1123 K.**

SEM image with EDX analysis and (b) an XRD pattern for the sample electrolyzed at 0.50 V for 15 min. Except the inner Ni substrate layer, three alloy layers were detected by the EDX analysis. At points (2), (3), and (4), the compositions are Dy:Ni = 16.7:83.3, 23.9:76.1, and 30.2:69.8, indicating that they are DyNi$_5$, DyNi$_3$, and DyNi$_2$, respectively. According to SEM image, the dominating phase of DyNi$_2$ layer exhibited a thickness of approximately 20 μm. Furthermore, the
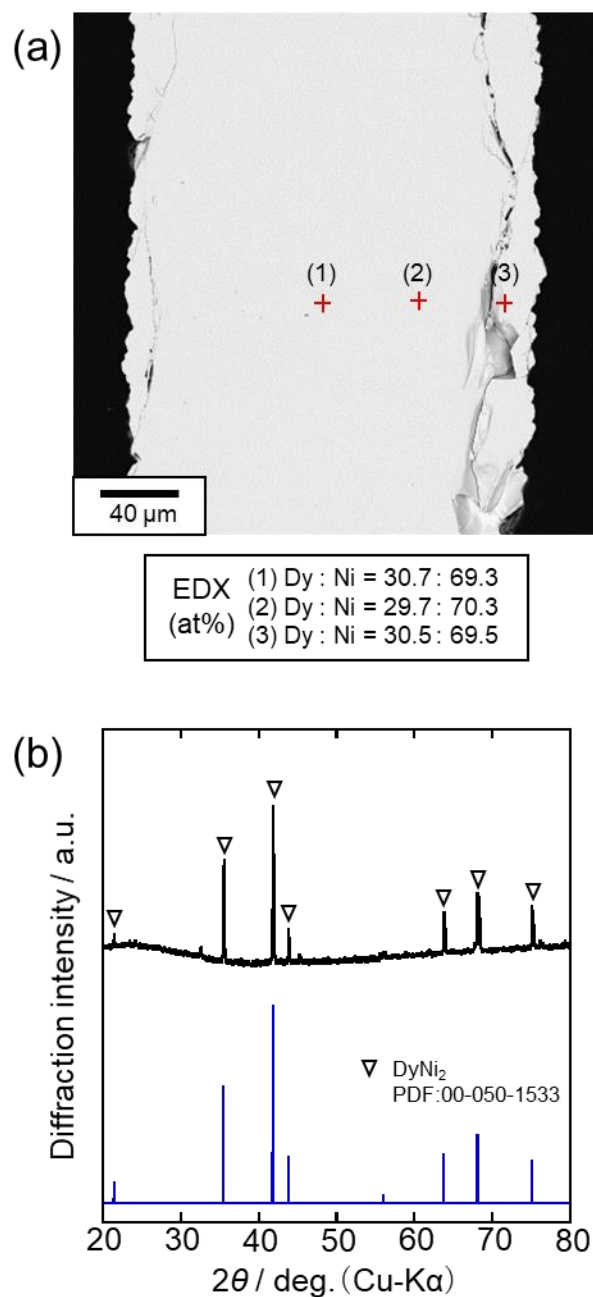
Fig. 2-16 **(a) A cross-sectional SEM image with EDX analysis and (b) an XRD pattern of the sample obtained by potentiostatic electrolysis with a Ni electrode at 0.50 V for 60 min in a molten CaCl$_2$–DyCl$_3$ (1.0 mol%) system at 1123 K.**

XRD analysis confirmed the formation of DyNi$_2$. Based on these results, the Dy-rich alloy formed in the first step was confirmed to be DyNi$_2$.

Fig. 2-18 shows (a) a cross-sectional SEM image with EDX analysis and (b) an XRD pattern for the sample electrolyzed at 0.70 V for 60 min in the second step. According to Fig. 2-18(a),
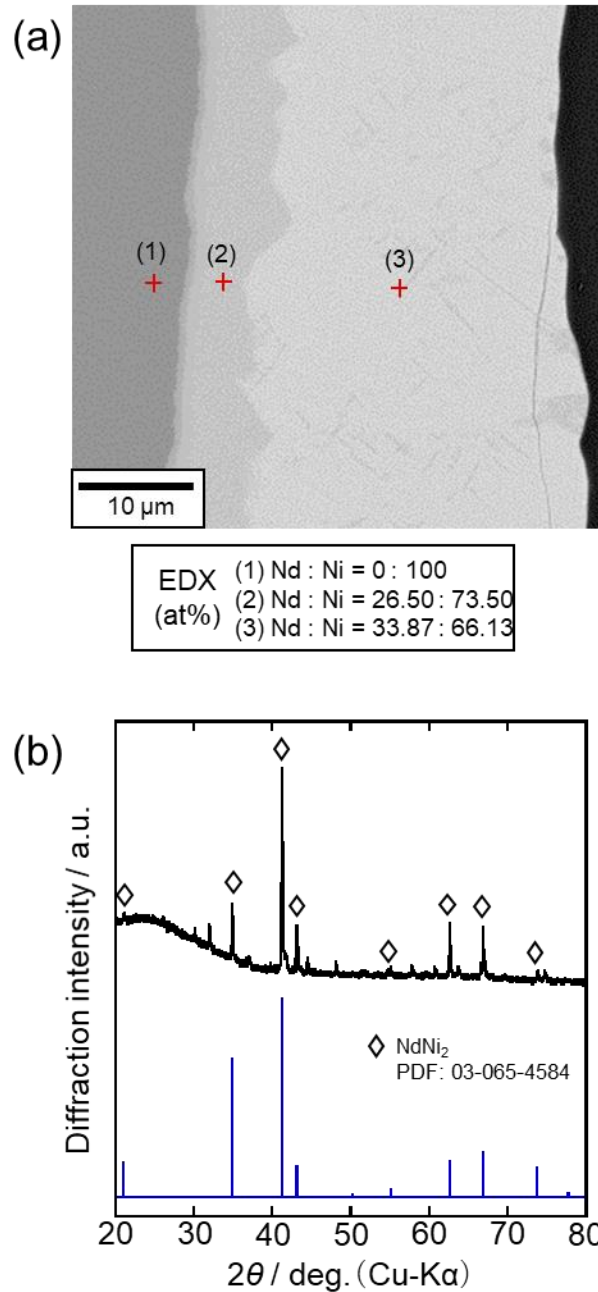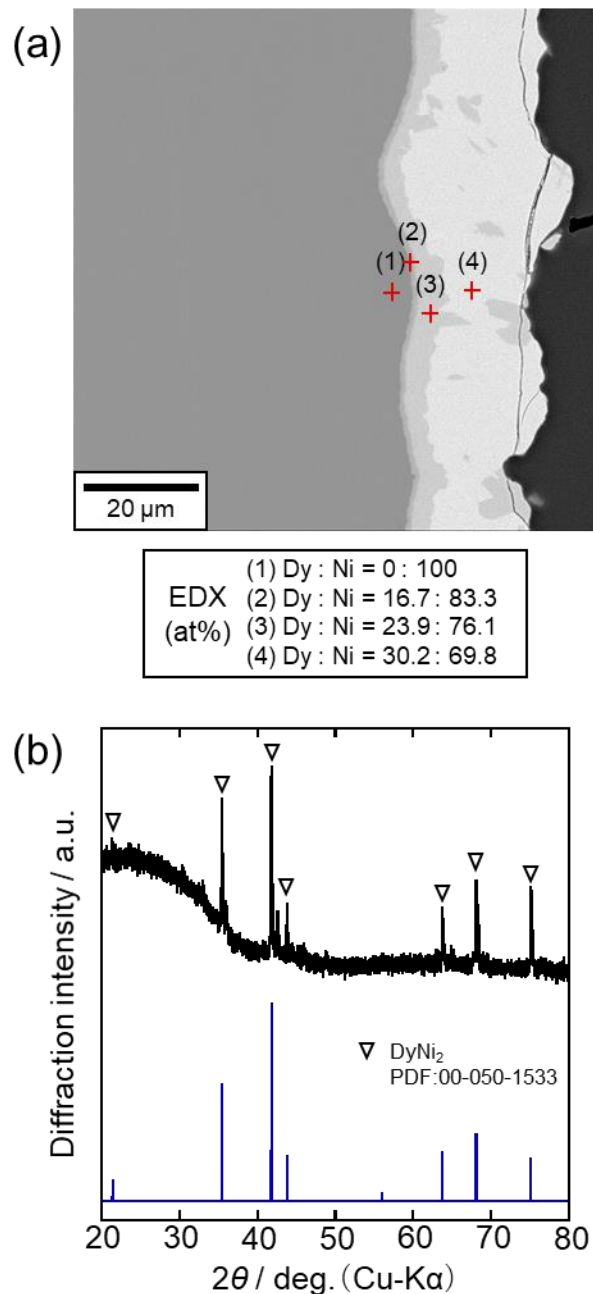
Fig. 2-17 **(a) A cross-sectional SEM image with EDX analysis and (b) an XRD pattern of the sample obtained by potentiostatic electrolysis with a Ni electrode at 0.50 V for 15 min in a molten $CaCl_2$–$DyCl_3$ (1.0 mol%) system at 1123 K.**

thickness of the alloy layer was larger than that in Fig. 2-17(a). The EDX analysis indicated the compositions at point (2) and (3) as, Dy:Ni = 16.8:83.2 and 23.7:76.3, which suggest the formation of $DyNi_5$ and $DyNi_3$, respectively. Compared to the $DyNi_2$ alloy layer formed in the first step, only $DyNi_3$ alloy was left on the surface of sample, as confirmed by the XRD analysis. Thus, $DyNi_3$ is

49
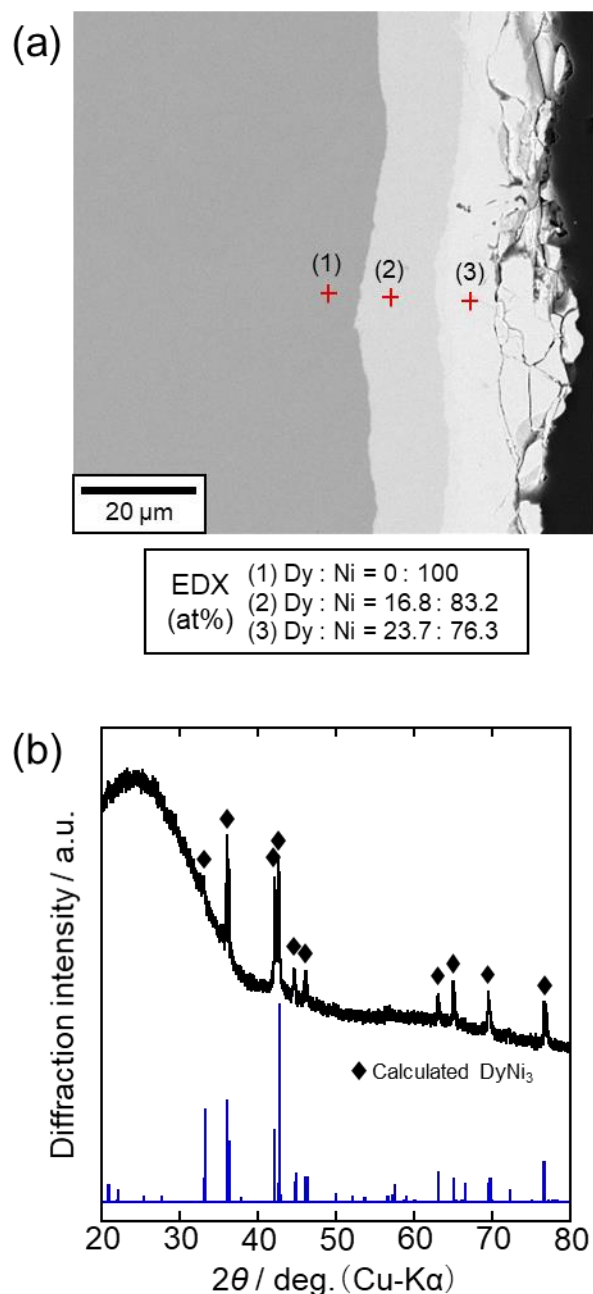
Fig. 2-18   **(a) A cross-sectional SEM image with EDX analysis and (b) an XRD pattern of the sample obtained by potentiostatic electrolysis of the DyNi₂ electrode at 0.70 V for 60 min in a molten CaCl₂–DyCl₃ (1.0 mol%) system at 1123 K.**

the thermodynamically stable phase at 0.70 V. The middle DyNi₅ alloy layer was formed due to the interdiffusion between DyNi₃ and Ni substrate.

The same fabrication method was repeated; the second step was performed at 0.90 V for 60 min. Fig. 2-19 shows (a) a cross-sectional SEM image with EDX analysis and (b) an XRD pattern
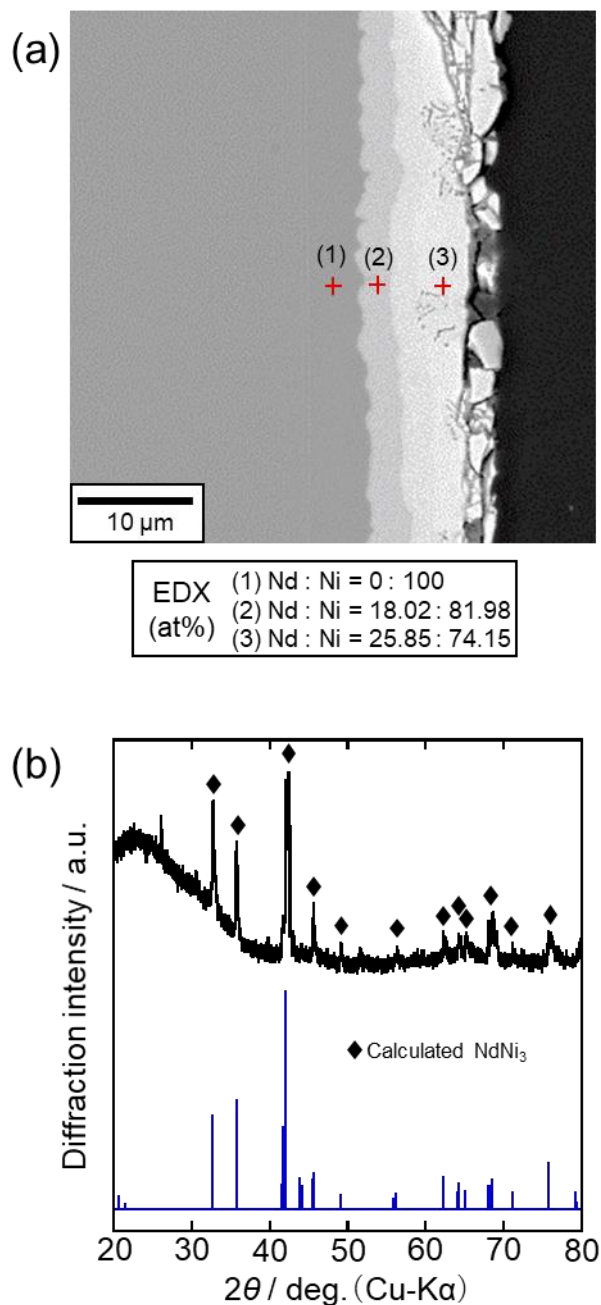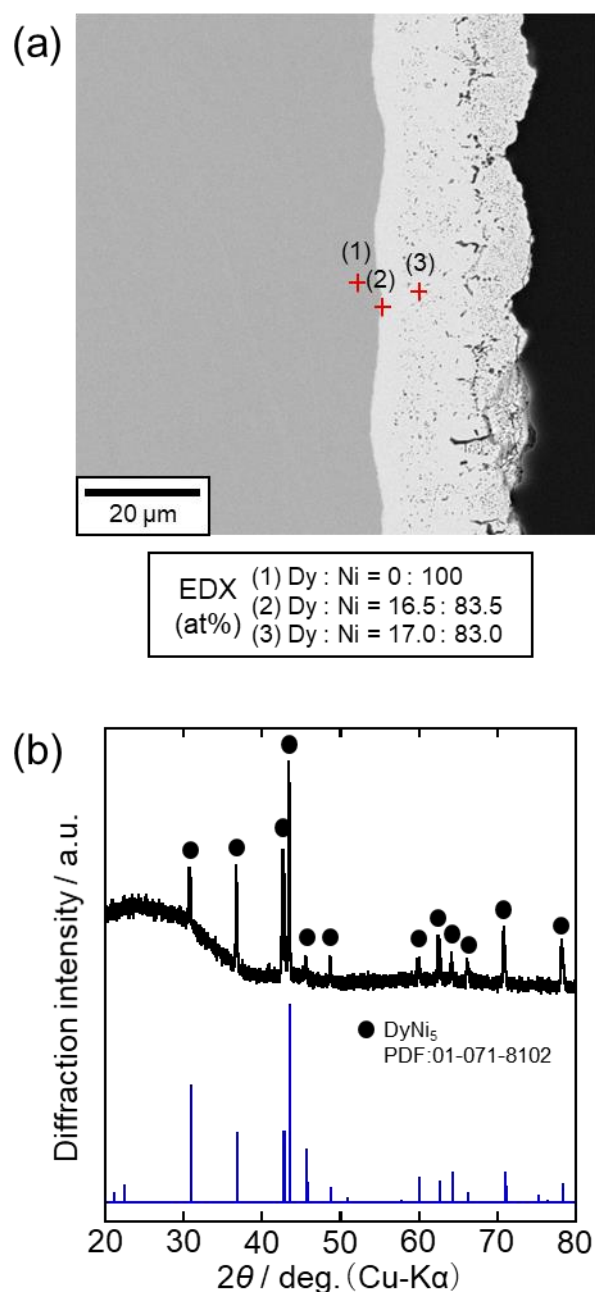
Fig. 2-19 **(a) A cross-sectional SEM image with EDX analysis and (b) an XRD pattern of the sample obtained by potentiostatic electrolysis of the DyNi$_2$ electrode at 0.90 V for 60 min in a molten CaCl$_2$–DyCl$_3$ (1.0 mol%) system at 1123 K.**

for the sample. A porous layer caused by the volume change during the Dy dissolution from DyNi$_2$ was observed. EDX analysis results at point (2) and (3) were Dy:Ni = 16.5:83.5 and 17.0:83.0, respectively, suggesting the alloy layer is DyNi$_5$. In addition, the XRD analysis confirmed the formation of DyNi$_5$. Therefore, DyNi$_5$ is the thermodynamically stable state at 0.90 V.

Finally, the sample was prepared at 1.20 V for 60 min in the second step. Fig. 2-20 shows (a) a cross-sectional SEM image with EDX analysis and (b) an XRD pattern for the sample. According to the SEM image, $DyNi_2$ alloy was transformed into a porous layer. Both EDX and XRD analyses confirmed the porous layer is Ni.

In the present study, formations of Dy_3Ni_2, Dy_2Ni_7, $DyNi_4$, Dy_4Ni_{17}, and Dy_2Ni_{17} were not

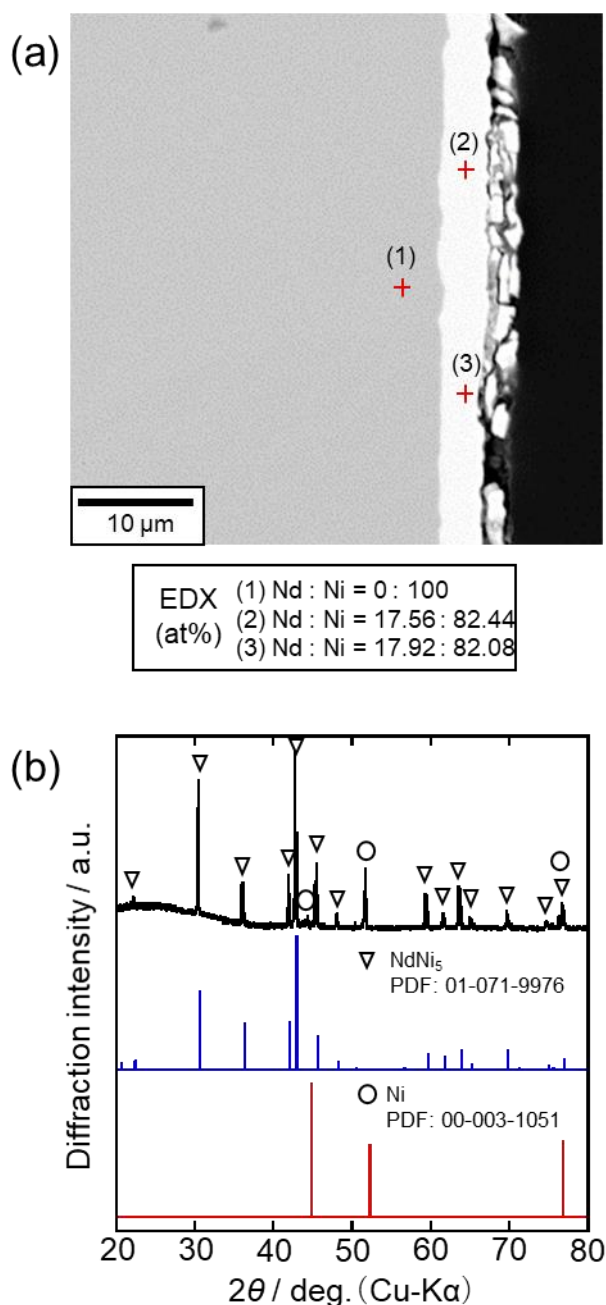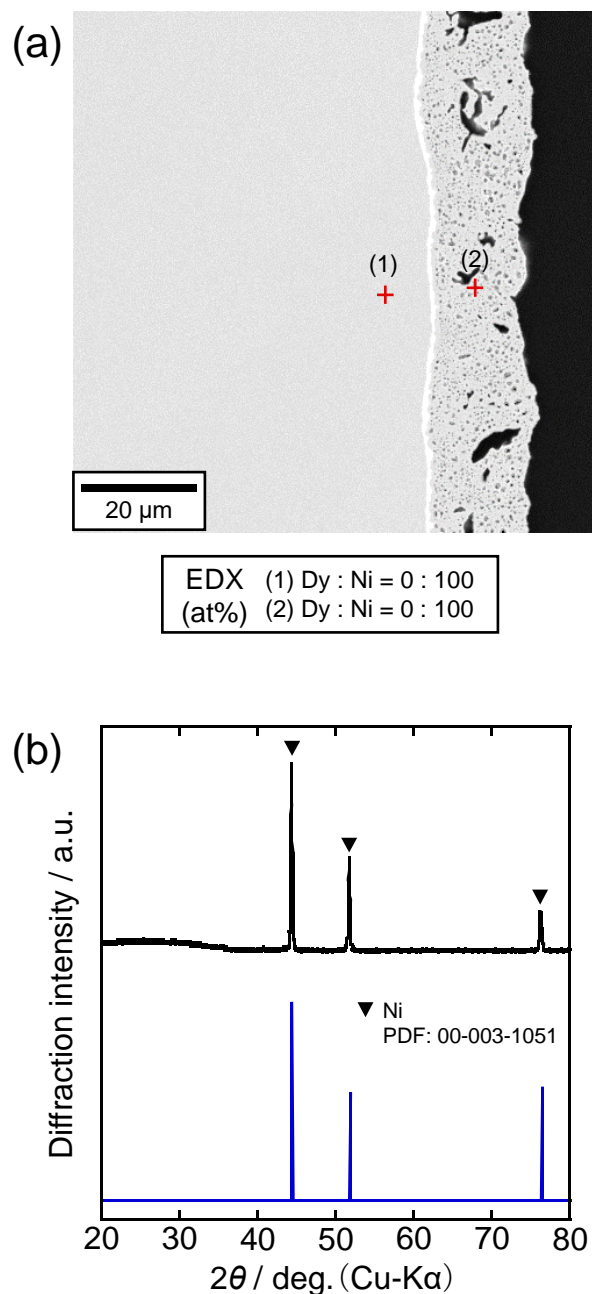**Fig. 2-20** **(a) A cross-sectional SEM image with EDX analysis and (b) an XRD pattern of the sample obtained by potentiostatic electrolysis of the $DyNi_2$ electrode at 1.20 V for 60 min in a molten $CaCl_2$–$DyCl_3$ (1.0 mol%) system at 1123 K.**

confirmed. It is probably caused by the slow formation rate of unconfirmed alloy phase and high transition rate to observe alloy phase in this system. From these results, the four potential plateaus (0.49, 0.62, 0.87, and 1.04 V) obtained in the open-circuit potentiometry measurement are found to correspond to the two-phase coexisting states of ($DyNi + DyNi_2$), ($DyNi_2 + DyNi_3$), ($DyNi_3 + DyNi_5$), and ($DyNi_5 + Ni$), respectively.

2.4   Conclusion

In this Chapter, the electrochemical behaviors of Nd^{3+} and Dy^{3+} were investigated in molten $CaCl_2$–$NdCl_3$ (1.0 mol%) and $CaCl_2$–$DyCl_3$ (1.0 mol%) systems, respectively, at 1123 K. The metallic Nd and Dy deposition potential were 0.27 and 0.33 V vs. Ca^{2+}/Ca. After electrolysis of a Ni electrode at various conditions, three potential plateaus were observed at 0.48, 0.68, and 0.95 V in the $NdCl_3$ addition system and four potential plateaus were observed at 0.49, 0.62, 0.87, and 1.04 V in the $DyCl_3$ addition system at the open-circuit potentiograms. The observed potential plateaus suggested different two-phase coexisting states. According to the SEM, EDX, and XRD analysis results, the thermodynamically stable phases at 0.30, 0.50, 0.80, and 1.00 V are $NdNi_2$, $NdNi_3$, $NdNi_5$, and Ni, respectively, in the $NdCl_3$ addition system. And the thermodynamically stable phases at 0.40, 0.50, 0.70, 0.90, and 1.20 V are $DyNi$, $DyNi_2$, $DyNi_3$, $DyNi_5$, and Ni, respectively, in the $DyCl_3$ addition system. The equilibrium reactions of RE–Ni alloys, RE metals, and the corresponding equilibrium potentials are summarized in Table 2-1. These potentials are also given with reference to the RE^{3+}/RE potential.

Table 2-1 **Equilibrium reactions and corresponding potentials for RE–Ni (RE = Nd, Dy) alloys and metallic RE in molten $CaCl_2$–$RECl_3$ (1.0 mol%) at 1123 K.**

Equilibrium reactions	Potential vs. Ca^{2+}/Ca / V		Potential vs. RE^{3+}/RE / V	
	RE = Nd	RE = Dy	RE = Nd	RE = Dy
$5\,Ni + RE^{3+} + 3\,e^- \rightleftharpoons RENi_5$	0.95	1.04	0.68	0.71
$3/2\,RENi_5 + RE^{3+} + 3\,e^- \rightleftharpoons 5/2\,RENi_3$	0.68	0.87	0.41	0.54
$2\,RENi_3 + RE^{3+} + 3\,e^- \rightleftharpoons 3\,RENi_2$	0.48	0.62	0.21	0.29
$RENi_2 + RE^{3+} + 3\,e^- \rightleftharpoons 2\,RENi$	–	0.49	–	0.16
$RE^{3+} + 3\,e^- \rightleftharpoons RE$	0.27	0.33	0	0

References

1. T. B. Massalski, H. Okamoto, P. R. Subramanian, and L. Kacprzak, *Binary Alloy Phase Diagrams,* (ASM International, Materials Park, Ohio), 2nd ed. (1990), CD-ROM version 1.0.

2. K. M. Axler and G. L. DePoorter, *Mater. Sci. Forum,* **73**, 19 (1991).

3. H. Okamoto, *J. Phase Equilib. Diffus.,* **36**, 390 (2015).

4. H. Okamoto, *J. Phase Equilib. Diffus.,* **35**, 105 (2014).

5. H. Konishi, T. Nishikiori, T. Nohira, and Y. Ito, *Electrochim. Acta,* **48**, 1403 (2003).

6. S. Kobayashi, K. Kobayashi, T. Nohira, R. Hagiwara, T. Oishi, and H. Konishi, *J. Electrochem. Soc.,* **158**, E142 (2011).

7. K. Yasuda, S. Kobayashi, T. Nohira, and R. Hagiwara, *Electrochim. Acta,* **92**, 349 (2013).

8. M. Notin, D. Belbacha, M. Rahmane, J. Hertz, G. Saindrenan, and J. L. Jorda, *J. Less-Common Met.,* **162**, 221 (1990).

9. A. V. Virkar and A. Raman, *J. Less-Common Met.,* **18**, 59 (1969).

10. D. T. Cromer and C. E. Olsen, *Acta Crystallogr.,* **12**, 689 (1959).

11. C. Nourry, L. Massot, P. Chamelot, and P. Taxil, *J. New Mater. Electrochem. Syst.,* **10**, 117 (2007).

12. S. Kobayashi, T. Nohira, K. Kobayashi, K. Yasuda, R. Hagiwara, T. Oishi, and H. Konishi, *J. Electrochem. Soc.,* **159**, E193 (2012).

13. H. Konishi, T. Usui, T. Nohira, and Y. Ito, *J. Phys. Conf. Ser.,* **165**, 012060 (2009).

14. K. Yasuda, S. Kobayashi, T. Nohira, and R. Hagiwara, *Electrochim. Acta,* **106**, 293 (2013).

Chapter 3

Thermodynamic Properties of RE–Ni (RE = Nd, Dy) Alloys in Molten CaCl₂–RECl₃

3.1   Introduction

In the previous chapter, the electrochemical formation of RE–Ni (RE = Nd, Dy) alloys were investigated in molten CaCl$_2$–RECl$_3$. As the fundamental research of the RE–Ni alloys, the thermodynamic properties of RE–Ni alloys were investigated in molten CaCl$_2$–RECl$_3$ by an electrochemical investigating method. According to the two-phase coexisting potentials of various RE–Ni alloys, the relative partial molar Gibbs energies and activities of RE and Ni could be calculated. Then, the standard Gibbs energies, enthalpies, and entropies of formation for various RE–Ni alloys were calculated using the temperature dependence of relative partial molar Gibbs energies of RE and Ni. Finally, the obtained thermodynamic parameters were compared with previously reported values.

3.2   Experimental

The preparation method of CaCl$_2$ and the experimental apparatus are almost the same as Chapter 2. Additional information is described below.

The Nd^{3+}/Nd potential was measured by open-circuit potentiometry, after electrodepositing Nd metal on a Mo electrode. And the Dy^{3+}/Dy potential was determined by measuring immersion potential of the Dy metal in the melt. All the two-phase coexisting potentials of Nd–Ni and Dy–Ni alloys were measured by open-circuit potentiometry using a Ni electrode. The same measurements

were conducted at 1073, 1098, 1123, 1148, and 1173 K to determine the temperature dependence of RE^{3+}/RE and the two-phase coexisting potentials of virous RE–Ni alloys.

3.3   Results and Discussion

3.3.1   Two-phase Coexisting Potential Measurements

3.3.1.1   CaCl$_2$–NdCl$_3$ System

In the previous Chapter, Nd$_2$Ni$_7$ was not observed in molten CaCl$_2$–NdCl$_3$ system due to its sluggish formation rate and its fast transition rate to NdNi$_5$. Since Nd$_2$Ni$_7$ was not confirmed for this system, further evaluations of the system were conducted based only on the metastable states.

As shown in Fig. 3-1 (a), after galvanostatic electrolysis at −3.0 A cm^{-2} for 30 s of a Mo electrode, two potential plateaus are observed at 1073 K. The former corresponds to the Ca^{2+}/Ca equilibrium, and the latter to the Nd^{3+}/Nd equilibrium. The plateau termination potential is slightly more positive than the plateau start potential because the Ca or Nd activity on the electrode surface decreases with Ca or Nd dissolution. Because the plateau slopes, the plateau potential is determined by extending the rapid shift line and later plateau line, as shown in Fig. 3-1 (b). In this study, the intersection of two such lines is defined as the plateau potential. The Nd^{3+}/Nd potential is 0.255 V (vs. Ca^{2+}/Ca) at 1073 K. Subsequently, the two-phase coexisting potentials of the Nd–Ni alloys were determined via open-circuit potentiometry using a Ni electrode. Fig. 3-2 shows the open-circuit potentiogram of a Ni electrode. The electrode potential gradually shifts to positive, and the three potential plateaus (i), (ii), and (iii) are observed. The shift is due to the diffusion of Nd atoms within the formed Nd–Ni alloy into the bulk electrode or dissolution in the melt via oxidation by the residual impurities. When two phases coexist on the electrode surface, potential plateaus are observed because the degree of freedom determined by the Gibbs phase rule is zero. Conversely, the potential shifts rapidly to positive values when only one Nd–Ni alloy exists on the electrode surface because the degree of freedom is zero. Three potential plateaus are observed after 180 s of potentiostatic electrolysis at 0.30 V. According to the last Chapter, the three potential plateaus (i),
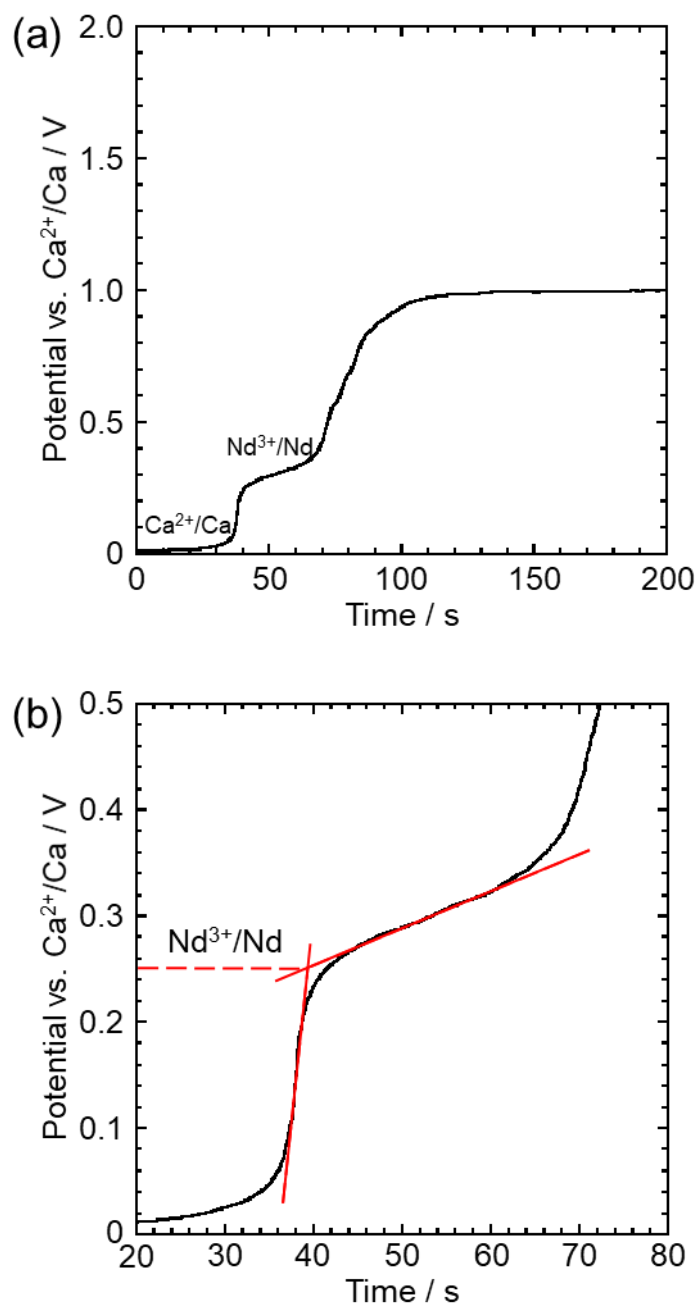
Fig. 3-1 **(a) Open-circuit potentiogram of a Mo flag in molten CaCl₂–NdCl₃ (1.0 mol%) system electrode after galvanostatic electrolysis at −3.0 A cm⁻² for 30 s at 1073 K. (b) Enlarged figure showing how the plateau potential is determined.**

(ii), and (iii) at 0.492, 0.669, and 0.960 V, respectively, vs. Ca^{2+}/Ca correspond to the phase coexisting states of ($NdNi_2$ + $NdNi_3$), ($NdNi_3$ + $NdNi_5$), and ($NdNi_5$ + Ni), respectively. After measurement at 1073 K, the same experiments were conducted at 1098, 1123, 1148, and 1173 K. The two-phase coexisting potentials, expressed with respect to the Nd^{3+}/Nd potential at each

temperature, are shown in Table 3-1.
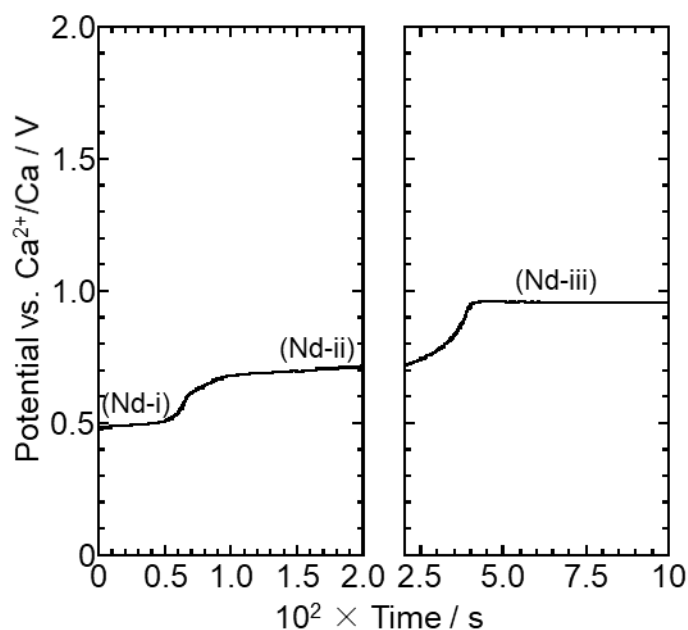
Fig. 3-2   **Open-circuit potentiogram of a Ni flag electrode in molten $CaCl_2$–$NdCl_3$ (1.0 mol%) system after potentiostatic electrolysis at 0.30 V for 180 s at 1073 K.**

Table 3-1   **Two-phase coexisting potentials in molten $CaCl_2$–$NdCl_3$ (1.0 mol%) system at 1073–1173 K.**

Plateau No.	Potential vs. Nd^{3+}/Nd E/V [a]					Coexisting phases
	1073 K	1098 K	1123 K	1148 K	1173 K	
(Nd-i)	0.237	0.233	0.238	0.234	0.238	$NdNi_2$ + $NdNi_3$
(Nd-ii)	0.414	0.419	0.416	0.401	0.404	$NdNi_3$ + $NdNi_5$
(Nd-iii)	0.705	0.709	0.704	0.703	0.705	$NdNi_5$ + Ni

a) The Nd^{3+}/Nd potentials are 0.255, 0.245, 0.235, 0.234, and 0.227 V vs. Ca^{2+}/Ca at 1073, 1098, 1123, 1148, and 1173 K, respectively.

3.3.1.2 $CaCl_2$–$DyCl_3$ System

Due to the similar reason, several Dy–Ni alloys (Dy_3Ni_2, Dy_2Ni_7, $DyNi_4$, Dy_4Ni_{17}, and Dy_2Ni_{17}) were also not found in $CaCl_2$–$DyCl_3$ system. The evaluations of the system were also

conducted based only on the metastable states.

To measure the equilibrium potential of Dy^{3+}/Dy, a Dy rod electrode was immersed in molten $CaCl_2$–$DyCl_3$. As shown with blue lines in Fig. 3-3, a very stable potential was observed, which should correspond to the equilibrium potential of Dy^{3+}/Dy. In order to accurately measure the two-coexisting potentials of Dy–Ni alloys, open-circuit potentiometry was performed at a Ni flag electrode in the melts. The obtained potentiogram are shown as red curves in Fig. 3-3. After potentiostatic electrolysis at 0.40 V for 20 min, the electrode potential gradually shifted to a more positive value as Dy in the formed Dy–Ni alloys diffused into the bulk electrode or dissolved into the melt. The potential shifted to positive values when only one Dy–Ni alloy existed on the electrode surface. As explained above, the four potential plateaus should correspond to the different two-phases coexisting states of Dy–Ni alloys. From the last chapter, four potential plateaus appeared and they should correspond to the two-phase coexisting states of $(DyNi + DyNi_2)$, $(DyNi_2 + DyNi_3)$, $(DyNi_3 + DyNi_5)$, and $(DyNi_5 + Ni)$. The same experiments were also conducted at 1098,
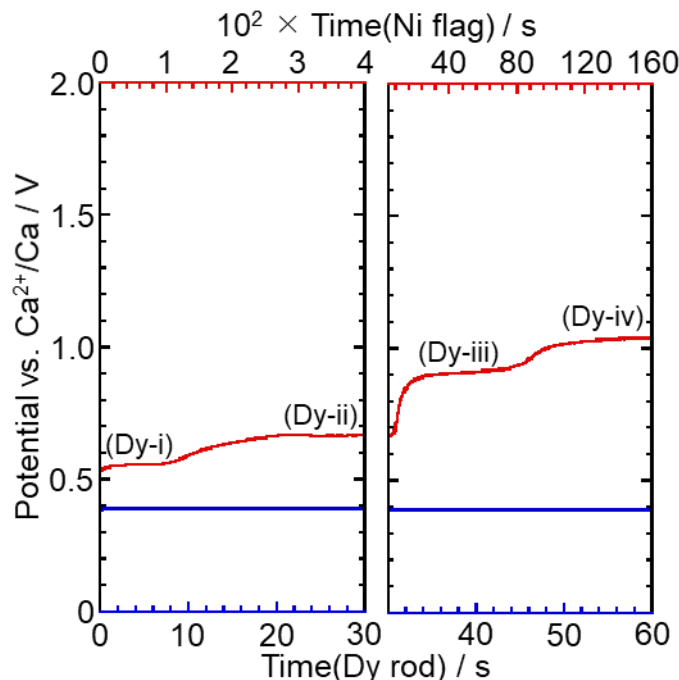
Fig. 3-3 **Immersion potentiogram of a Dy rod electrode (blue line) and open-circuit potentiogram of a Ni flag electrode (red line) after potentiostatic electrolysis at 0.40 V for 20 min in molten $CaCl_2$–$DyCl_3$ (1.0 mol%) system at 1073 K.**

1123, 1148, and 1173 K and the two-phase coexisting potentials, expressed with respect to the

Dy^{3+}/Dy potential at each temperature, are summarized in Table 3-2.

Table 3-2   **Two-phase coexisting potentials in molten CaCl$_2$–DyCl$_3$ (1.0 mol%) system at 1073–1173 K.**

Plateau No.	Potential vs. Dy^{3+}/Dy, E/V [a]					Coexisting phases
	1073 K	1098 K	1123 K	1148 K	1173 K	
(Dy-i)	0.165	0.164	0.151	0.150	0.150	DyNi + DyNi$_2$
(Dy-ii)	0.271	0.268	0.274	0.260	0.265	DyNi$_2$ + DyNi$_3$
(Dy-iii)	0.502	0.500	0.500	0.474	0.476	DyNi$_3$ + DyNi$_5$
(Dy-iv)	0.656	0.667	0.683	0.674	0.663	DyNi$_5$ + Ni

a) The Dy^{3+}/Dy potentials were 0.391, 0.377, 0.360, 0.359, and 0.344 V vs. Ca^{2+}/Ca at 1073, 1098, 1123, 1148, and 1173 K, respectively.

3.3.2   Thermodynamic Calculations

3.3.2.1   Nd–Ni Alloys

The temperature dependences of the two-phase coexisting potentials are plotted in Fig. 3-4, with the corresponding regression lines. The temperature dependences of the two-phase coexisting potentials (vs. Nd^{3+}/Nd, E/V) are expressed as functions of temperature, T (K), using the following equations:

$$E_{(Nd-i)} = 0.223 - 1.12 \times 10^{-5}T \qquad (NdNi_2 + NdNi_3), \qquad (1)$$

$$E_{(Nd-ii)} = 0.584 - 1.54 \times 10^{-4}T \qquad (NdNi_3 + NdNi_5), \qquad (2)$$

$$E_{(Nd-iii)} = 0.730 - 2.24 \times 10^{-5}T \qquad (NdNi_5 + Ni). \qquad (3)$$

According to Raoult's law, the relative partial molar Gibbs energies ($\Delta\overline{G}_{Nd}$) and activities (a_{Nd}) of Nd in each two-phase coexisting state are calculated using the obtained E and the following equations:
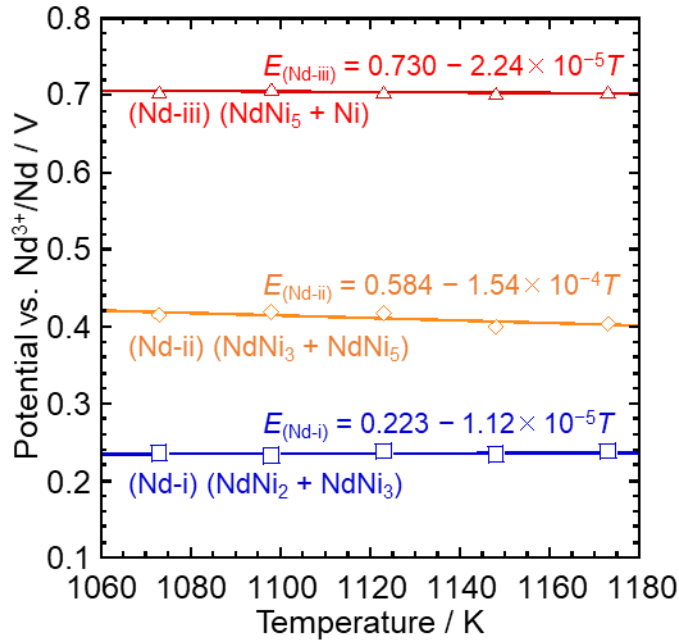
Fig. 3-4 **Temperature dependence of the two-phase coexisting potentials of various Nd–Ni alloys.**

$$\Delta \overline{G}_{Nd} = -3FE \tag{4}$$

and

$$a_{Nd} = \exp(\Delta \overline{G}_{Nd}/RT), \tag{5}$$

where F (C mol^{-1}) and R (J mol^{-1} K^{-1}) are the Faraday and gas constants, respectively. Subsequently, the Ni activity (a_{Ni}) with reference to pure solid Ni as the standard state in each two-phase coexisting state is calculated using the Gibbs-Duhem equation:

$$\ln a_{Ni} = -\int_{X_{Ni}=1}^{X_{Ni}} \frac{X_{Nd}}{X_{Ni}} \, d\ln a_{Nd}, \tag{6}$$

where X denotes the mole fraction of the component. According to the Nd–Ni phase diagram, the solid phases in this system are all line compounds with trivial solid-solution ranges. Therefore, the a_{Ni} in the (NdNi$_5$ + Ni) state is unity, according to Raoult's law. The $\Delta \overline{G}_{Ni}$ values are obtained using the following equation:

$$\Delta \overline{G}_{Ni} = RT \ln a_{Ni}. \tag{7}$$

The obtained $\Delta \overline{G}_{Nd}$ and $\Delta \overline{G}_{Ni}$ values are plotted as functions of temperature for each two-phase coexisting state, as shown in Fig. 3-5. The equations of the regression lines are presented in Table

Fig. 3-5 **Temperature dependence of the relative partial molar Gibbs energies of (a) Nd and (b) Ni in various Nd–Ni two-phase coexisting states.**

3-3. To calculate the relative partial molar enthalpies and entropies of Nd ($\Delta\overline{H}_{Nd}$ and $\Delta\overline{S}_{Nd}$) and Ni ($\Delta\overline{H}_{Ni}$ and $\Delta\overline{S}_{Ni}$), $\Delta\overline{G}_{Nd}$ or $\Delta\overline{G}_{Ni}$ are substituted into the Gibbs-Helmholtz equation:

$$\Delta\overline{G}_i = \Delta\overline{H}_i - \Delta\overline{S}_i \times T. \qquad (8)$$

In the enthalpy calculations, entropy is assumed to be independent of temperature. The calculated results are listed in Table 3-4. Subsequently, the standard Gibbs energies of formation for the Nd–Ni alloys per mol·atom ($\Delta G^\circ_{f(Nd-Ni)}$) are calculated using $\Delta \overline{G}_{Nd}$ and $\Delta \overline{G}_{Ni}$ and the following equation:

$$\Delta \overline{G}^\circ_{f(Ni-Nd)} = X_{Nd} \times \Delta \overline{G}_{Nd} + X_{Ni} \times \Delta \overline{G}_{Ni}. \tag{9}$$

Table 3-5 summarizes the values obtained.

The calculated standard Gibbs energies of formation for the Nd–Ni alloys are plotted, as shown in Fig. 3-6. The solid and broken lines indicate the experimental and extrapolated values, respectively. The values reported by Du and Clavaguera[1] (broken blue lines), Huang et al.[2] (broken

Table 3-3 **Equations of the regression lines of the temperature dependences of the relative partial molar Gibbs energies of Nd and Ni ($\Delta \overline{G}_{Nd}$ and $\Delta \overline{G}_{Ni}$) in the Nd–Ni alloys in two-phase coexisting states.**

Plateau No.	Coexisting phase	$\Delta \overline{G}_{Nd}$ / J (mol-Nd)$^{-1}$	$\Delta \overline{G}_{Ni}$ / J (mol-Ni)$^{-1}$
(Nd-i)	$NdNi_2 + NdNi_3$	$-6.46\times10^4 - 3.24T$	$-4.33\times10^4 + 8.32T$
(Nd-ii)	$NdNi_3 + NdNi_5$	$-1.69\times10^5 + 44.6T$	$-8.48\times10^3 - 7.62T$
(Nd-iii)	$NdNi_5 + Ni$	$-2.11\times10^5 + 6.48T$	0 [a]

a) The activity of Ni is approximated to be unity at these temperatures.

Table 3-4 **Relative partial molar enthalpies and entropies of Nd ($\Delta \overline{H}_{Nd}$ and $\Delta \overline{S}_{Nd}$) and Ni ($\Delta \overline{H}_{Ni}$ and $\Delta \overline{S}_{Ni}$) of the Nd–Ni alloys in two-phase coexisting states, according to the Gibbs-Helmholtz equation and assuming temperature independent entropy.**

Coexisting phase	$\Delta \overline{H}_{Nd}$ / kJ (mol-Nd)$^{-1}$	$\Delta \overline{H}_{Ni}$ / kJ (mol-Ni)$^{-1}$	$\Delta \overline{S}_{Nd}$ / J (mol-Nd)$^{-1}$ K^{-1}	$\Delta \overline{S}_{Ni}$ / J (mol-Ni)$^{-1}$ K^{-1}
$NdNi_2 + NdNi_3$	-64.6	-43.3	3.24	-8.32
$NdNi_3 + NdNi_5$	-169	-8.48	-44.6	7.62
$NdNi_5 + Ni$	-211	0	-6.48	0

Table 3-5   Standard Gibbs energies of formation ($\Delta G_{\mathrm{f}}^{\circ}$) for the Nd–Ni alloys.

Phase	$\Delta G_{\mathrm{f}}^{\circ}$ / J (mol·atom)$^{-1}$
NdNi$_2$	$-5.04\times10^4 + 4.47T$
NdNi$_3$	$-4.86\times10^4 + 5.43T$
NdNi$_5$	$-3.52\times10^4 + 1.08T$
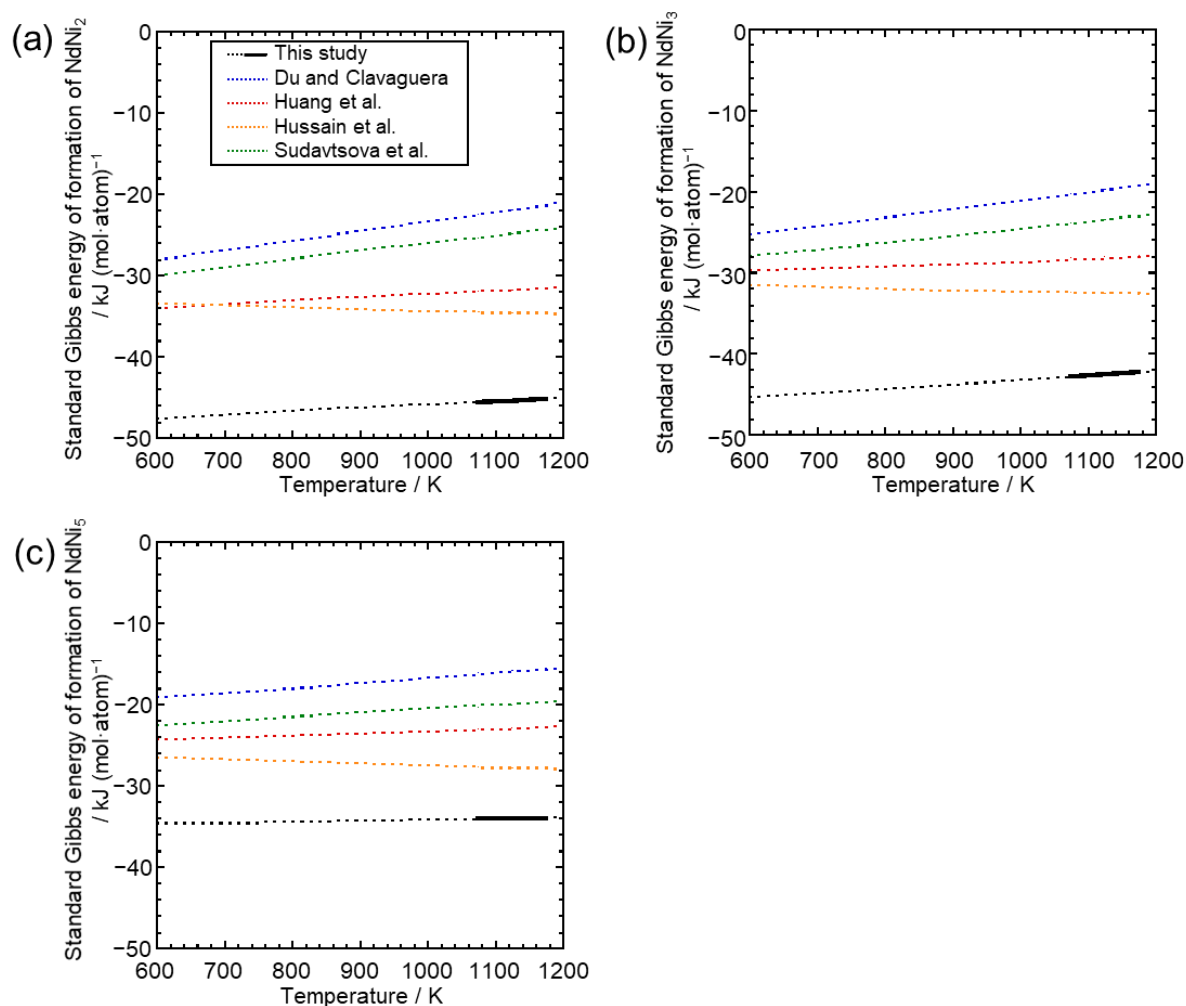
Fig. 3-6   Calculated standard Gibbs energies of formation for (a) NdNi$_2$, (b) NdNi$_3$, and (c) NdNi$_5$. The solid line indicates the experimental temperature range.

red lines), Hussain et al.[3] (broken yellow lines), and Sudavtsova et al.[4] (broken green lines) are also plotted for comparison. Although similar methods were used in each previous study, non-negligible differences are observed, particularly at higher temperatures. The values obtained in this study are more negative than all reported values. This is similar to the previous study,[5] which compared the

standard Gibbs energies of formation for Dy–Ni alloys with the values obtained using CALPHAD.[6] Because the slopes of the plotted lines are similar, the standard entropies of formation for the Nd–Ni alloys ($\Delta S^{\circ}_{\text{f(Nd–Ni)}}$) are close to the reported values. Using the Gibbs-Helmholtz equation (Eq. 8), the standard enthalpies ($\Delta H^{\circ}_{\text{f(Nd–Ni)}}$) and entropies of formation for the Nd–Ni alloys are calculated and summarized in Table 3-6 and Fig. 3-7. The previously reported values are plotted in Fig. 3-7 using different colors. In this study, the standard enthalpy of formation for NdNi$_2$ is −50.4 kJ (mol·atom)$^{-1}$, which is approximately 15 kJ (mol·atom)$^{-1}$ lower than the four reported values. As for NdNi$_3$ and NdNi$_5$, the standard enthalpies of formation are −48.6 and −35.2 kJ (mol·atom)$^{-1}$, respectively, in this study. The differences from the four reported values of NdNi$_3$ and NdNi$_5$ are approximately 17 and 10 kJ (mol·atom)$^{-1}$, respectively. This may be due to the new electrochemical method used in this study. All previous studies used the CALPHAD technique and calorimetry,

Table 3-6 Standard enthalpies and entropies of formation ($\Delta H^{\circ}_{\text{f}}$ and $\Delta S^{\circ}_{\text{f}}$) for the Nd–Ni alloys.

Phase	$\Delta H^{\circ}_{\text{f}}$ / kJ (mol·atom)$^{-1}$	$\Delta S^{\circ}_{\text{f}}$ / J (mol·atom)$^{-1}$ K^{-1}
NdNi$_2$	−50.4	−4.47
NdNi$_3$	−48.6	−5.43
NdNi$_5$	−35.2	−1.08
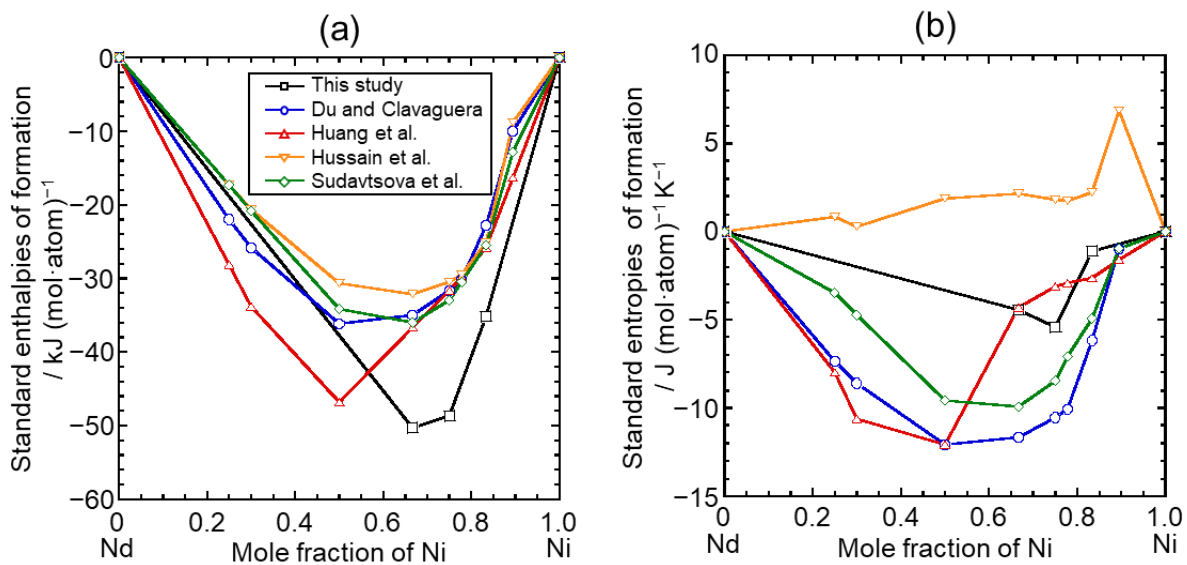
Fig. 3-7 Calculated standard (a) enthalpies and (b) entropies of formation for the Nd–Ni alloys.

although similar systematic errors could have occurred in their studies. Another possibility may be inaccuracy in determining the starting point of the plateau. As shown in Figs. 3-1 and 3-2, the plateaus are not completely horizontal. In this study, the plateau potential is defined using the intersection of the rapid shift line and later plateau line, potentially resulting in a determined potential that is slightly more negative than the actual plateau potential. The standard entropies of formation of NdNi$_2$, NdNi$_3$, and NdNi$_5$ in this study are −4.47, −5.43, and −1.08 J (mol·atom)$^{-1}$ K^{-1}, respectively. Most of the reported values are also negative, except for those reported by Hussain et al. Because most intermetallic compound systems exhibit negative standard entropies of formation, the values reported by Hussain et al. are insufficiently reliable. The other reported values, particularly those reported by Huang et al., are consistent with this study. Because all the standard entropies of formation are small, a wider range of experimental temperatures should yield a more reliable determination.

3.3.2.2 Dy–Ni Alloys

Based on the same theory, the thermodynamic properties could also be calculated. The two-phase coexisting potentials expressed in reference to the Dy^{3+}/Dy potential at each temperature are shown in Table 3-2, while the regression lines representing the temperature dependences of the two-phase coexisting potentials are plotted in Fig. 3-8. The two-phase coexisting potentials (vs. Dy^{3+}/Dy E/V) can be expressed by the following equations:

$$E_{(Dy\text{-}i)} = 0.350 - 1.73 \times 10^{-4} T \qquad (\text{DyNi} + \text{DyNi}_2), \qquad (10)$$

$$E_{(Dy\text{-}ii)} = 0.358 - 8.04 \times 10^{-5} T \qquad (\text{DyNi}_2 + \text{DyNi}_3), \qquad (11)$$

$$E_{(Dy\text{-}iii)} = 0.847 - 3.18 \times 10^{-4} T \qquad (\text{DyNi}_3 + \text{DyNi}_5), \qquad (12)$$

$$E_{(Dy\text{-}iv)} = 0.582 + 7.68 \times 10^{-5} T \qquad (\text{DyNi}_5 + \text{Ni}). \qquad (13)$$

Depending on the equations (4)–(7) listed above, $\Delta \overline{G}_{Dy}$ and $\Delta \overline{G}_{Ni}$ could be calculated. The calculated $\Delta \overline{G}_{Dy}$ and $\Delta \overline{G}_{Ni}$ values are plotted in Fig. 3-9 and the regression equations are
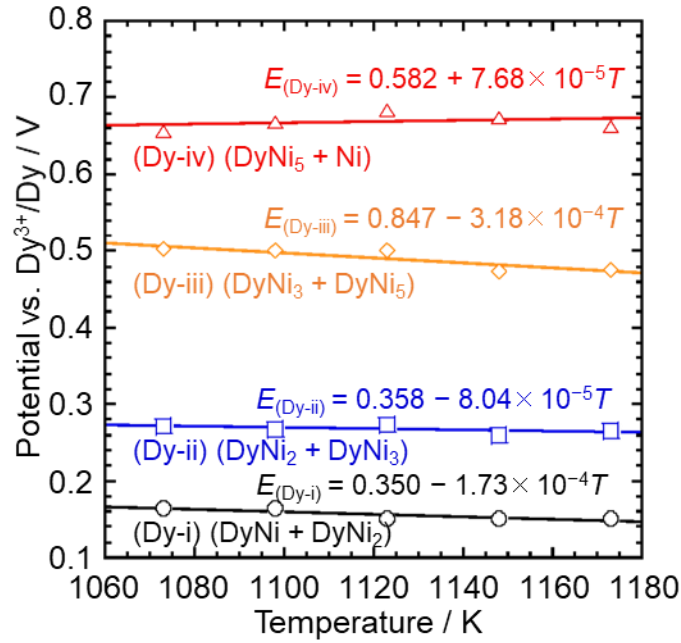
Fig. 3-8 **Temperature dependence of the two-phase coexisting potentials of various Dy–Ni alloys.**

summarized in Table 3-7. By substituting $\Delta \overline{G}_{Dy}$ and $\Delta \overline{G}_{Ni}$ into the equation (8), the relative partial molar enthalpies and entropies of Dy ($\Delta \overline{H}_{Dy}$ and $\Delta \overline{S}_{Dy}$) and Ni ($\Delta \overline{H}_{Ni}$ and $\Delta \overline{S}_{Ni}$) were calculated and the results are listed in Table 3-8. The standard Gibbs energies of formation for Dy–Ni alloys ($\Delta G^{\circ}_{f(Dy-Ni)}$) were calculated from $\Delta \overline{G}_{Dy}$ and $\Delta \overline{G}_{Ni}$ using the equation (9). The calculated results are shown in Table 3-9 and plotted as broken black lines in Fig. 3-10 for comparison with the CALPHAD values reported by Li et al. (broken red lines).[6] Although the experimental temperatures is different (663–773 K), values reported by Konishi et al. (broken blue lines)[5] were also plotted. In Fig. 3-10, the solid lines indicate the experimental temperature range. The results obtained in this study were close to the two sets of reported values in the experimental temperature range of 1073–1173 K. However, they were slightly more negative than the CALPHAD values and slightly more positive than the experimental values of Konishi et al.

Finally, using the Gibbs-Helmholtz equation (8), the standard enthalpies and entropies of formation for Dy–Ni alloys were calculated and are listed in Tables 3-10. For comparison, the standard enthalpies of formation values reported by CALPHAD and calorimetry, and the standard
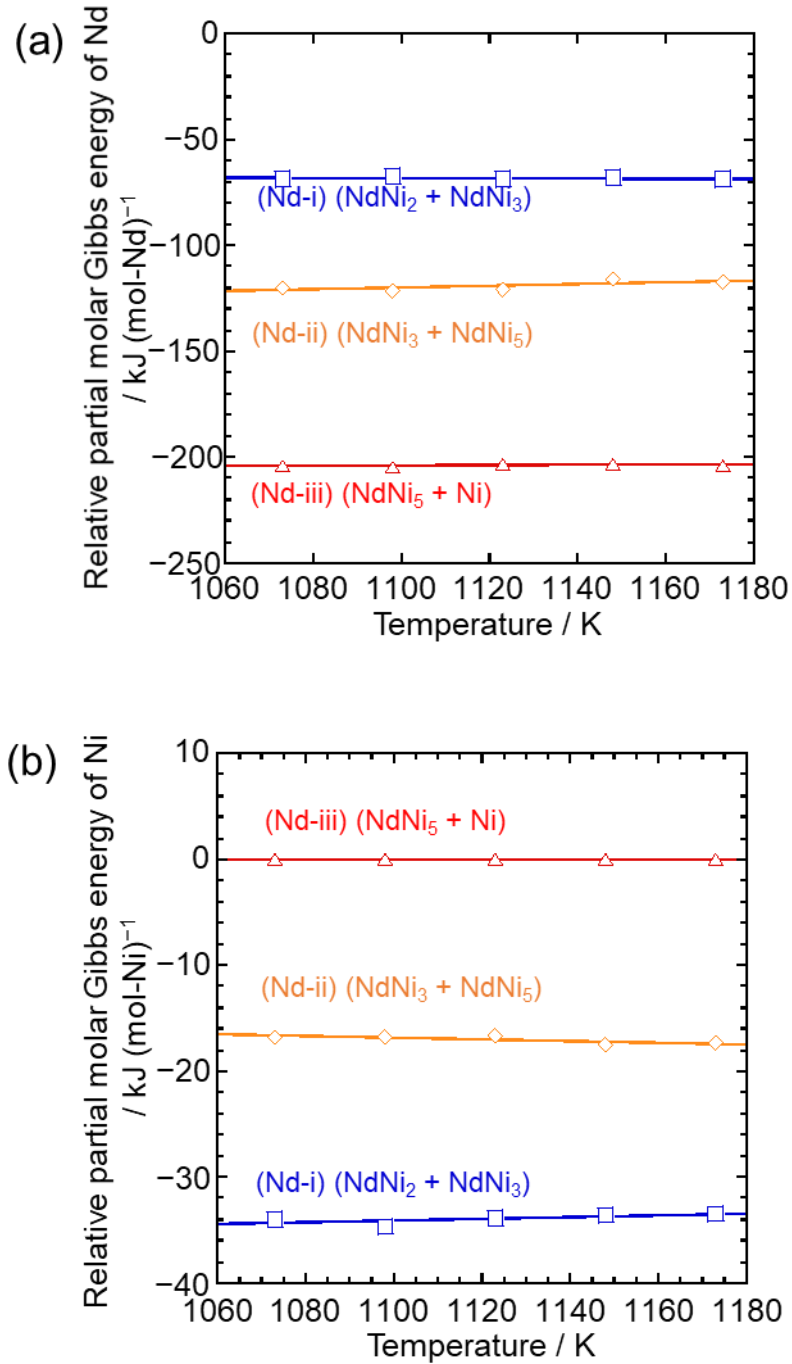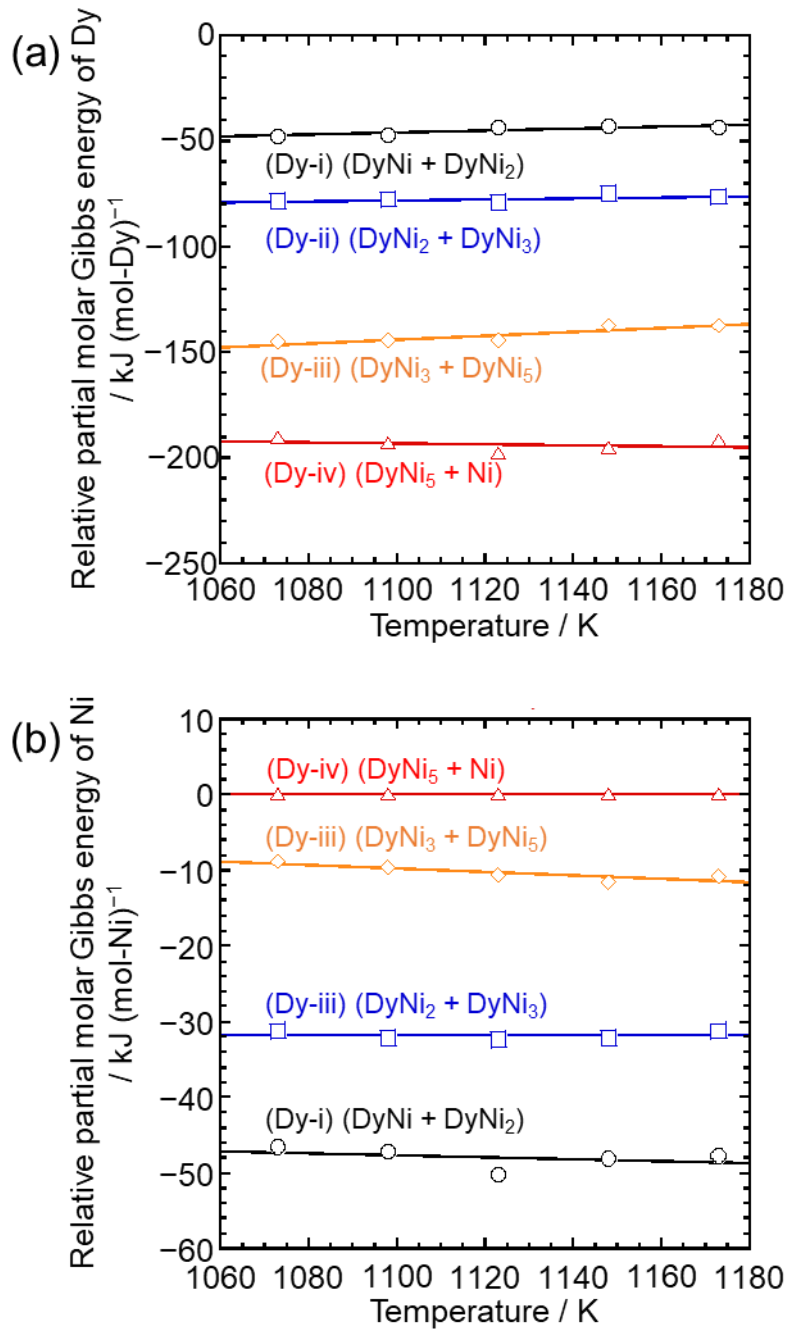
Fig. 3-9 Temperature dependence of the relative partial molar Gibbs energies of (a) Dy and (b) Ni in various Dy–Ni two-phase coexisting states.

entropies of formation values reported by CALPHAD are also listed. For the DyNi alloy, $\Delta H_\mathrm{f}^\circ$ of this study is more negative than the CALPHAD and calorimetry values. And $\Delta S_\mathrm{f}^\circ$ is also more negative than the CALPHAD value. The ambiguity and difficulty in determining the potential plateau (i) in Fig. 3-3. might be one possible reason to cause this deviation. Since the potential shift

Table 3-7   Equations of the regression lines of the temperature dependences of the relative partial molar Gibbs energies of Dy and Ni ($\Delta\overline{G}_{\text{Dy}}$ and $\Delta\overline{G}_{\text{Ni}}$) in the Dy–Ni alloys in two-phase coexisting states.

| Plateau No.	Coexisting phase	$\Delta\overline{G}_{\text{Dy}}$ / J (mol-Dy)$^{-1}$	$\Delta\overline{G}_{\text{Ni}}$ / J (mol-Ni)$^{-1}$
(Dy-i)	DyNi + DyNi$_2$	$-1.01\times10^5 + 5.00\times10T$	$-3.31\times10^4 - 1.33\times10T$
(Dy-ii)	DyNi$_2$ + DyNi$_3$	$-1.04\times10^5 + 2.33\times10T$	$-3.19\times10^4 + 6.95\times10^{-2}T$
(Dy-iii)	DyNi$_3$ + DyNi$_5$	$-2.45\times10^5 + 9.20\times10T$	$1.53\times10^4 - 2.29\times10T$
(Dy-iv)	DyNi$_5$ + Ni	$-1.69\times10^5 - 2.22\times10T$	0 [a]

a) The activity of Ni is approximated to be unity at these temperatures.

Table 3-8   Relative partial molar enthalpies and entropies of Dy ($\Delta\overline{H}_{\text{Dy}}$ and $\Delta\overline{S}_{\text{Dy}}$) and Ni ($\Delta\overline{H}_{\text{Ni}}$ and $\Delta\overline{S}_{\text{Ni}}$) of the Dy–Ni alloys in two-phase coexisting states, according to the Gibbs-Helmholtz equation and assuming temperature independent entropy.

Coexisting phase	$\Delta\overline{H}_{\text{Dy}}$ / kJ (mo-Dy)$^{-1}$	$\Delta\overline{H}_{\text{Ni}}$ / kJ (mol-Ni)$^{-1}$	$\Delta\overline{S}_{\text{Dy}}$ / J (mol-Dy)$^{-1}$ K^{-1}	$\Delta\overline{S}_{\text{Ni}}$ / J (mol-Ni)$^{-1}$ K^{-1}
DyNi + DyNi$_2$	-101	-33.1	-50.0	13.3
DyNi$_2$ + DyNi$_3$	-104	-31.9	-23.3	-0.0695
DyNi$_3$ + DyNi$_5$	-245	15.3	-92.0	22.9
DyNi$_5$ + Ni	-169	0	22.2	0

Table 3-9   Standard Gibbs energies of formation ($\Delta G_{\text{f}}^{\circ}$) for the Dy–Ni alloys.

Phase	$\Delta G_{\text{f}}^{\circ}$ / J (mol·atom)$^{-1}$
DyNi	$-6.71\times10^4 + 1.84\times10T$
DyNi$_2$	$-5.58\times10^4 + 7.80T$
DyNi$_3$	$-4.98\times10^4 + 5.87T$
DyNi$_5$	$-2.81\times10^4 - 3.71T$

to the plateau (i) could not be clearly observed, there may be slight inaccuracy in determining the start of the plateau (i). This small deviation may have caused the 16 J (mol·atom)$^{-1}$ K^{-1} difference in $\Delta S_{\text{f(DyNi)}}^{\circ}$, which would make $\Delta H_{\text{f(DyNi)}}^{\circ}$ more negative than the CALPHAD and calorimetry values. For the DyNi$_2$ alloy, $\Delta H_{\text{f}}^{\circ}$ and $\Delta S_{\text{f}}^{\circ}$ of this study are almost the same as the CALPHAD values. However, the calorimetry value of $\Delta H_{\text{f}}^{\circ}$ is more positive than both this study and the value of CALPHAD. Nevertheless, the difference is smaller than that for the DyNi, which is likely due
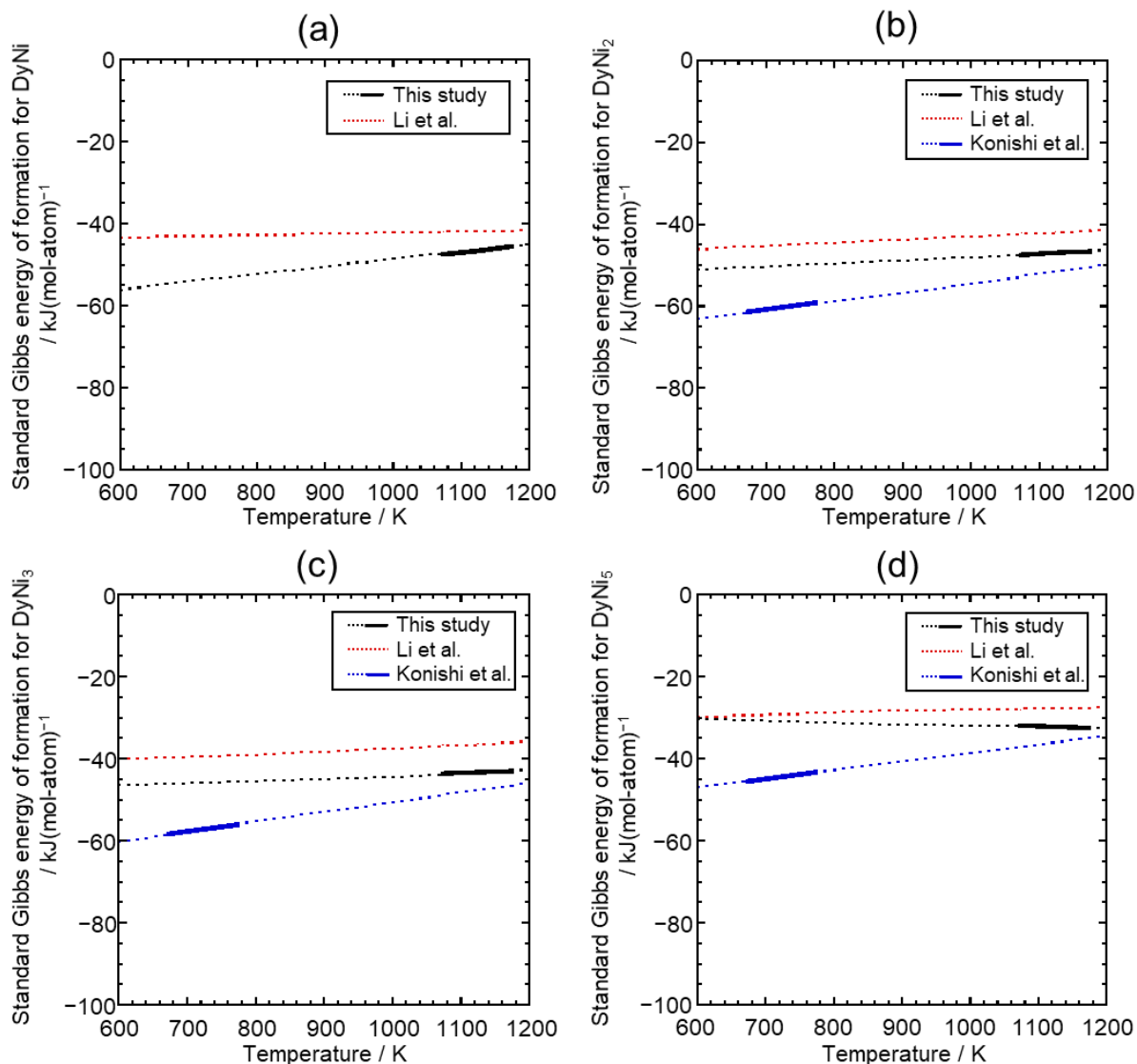
Fig. 3-10   Calculated standard Gibbs energies of formation for (a) DyNi, (b) DyNi$_2$, (c) DyNi$_3$, and (d) DyNi$_5$. The solid line indicates the experimental temperature range.

to the more accurate determination of the potential plateau (ii) than that of plateau (i). For the DyNi$_3$ alloy, both ΔH_f° and ΔS_f° are close to the CALPHAD values. Here, no calorimetry value has been reported for DyNi$_3$. As for the DyNi$_5$ alloy, ΔH_f° was close to all the reported values. However, ΔS_f° of this study, 3.71 J (mol·atom)$^{-1}$ K^{-1}, is more positive than the CALPHAD value, -3.75 J (mol·atom)$^{-1}$ K^{-1}.

In this calculation, all the ΔH_f° values are more negative than calorimetry values. Since calorimetry is a method of directly detecting thermal variables, it should have a higher accuracy

Table 3-10 Standard enthalpies and entropies of formation ($\Delta H_\mathrm{f}^\circ$ and $\Delta S_\mathrm{f}^\circ$) for the Dy–Ni alloys.

Phase	$\Delta H_\mathrm{f}^\circ$ / kJ (mol·atom)$^{-1}$				$\Delta S_\mathrm{f}^\circ$ / J (mol·atom)$^{-1}$ K^{-1}	
	This study	Li et al. (CALPHAD)	Schott et al. (Calorimetry)	Guo et al. (Calorimetry)	This study	Li et al. (CALPHAD)
DyNi	−67.1	−44.8	−33.4 ± 1.9	−35.2 ± 1.5	−18.4	−2.60
DyNi$_2$	−55.8	−50.7	−32.6 ± 1.8	–	−7.80	−7.82
DyNi$_3$	−49.8	−44.3	–	–	−5.87	−7.17
DyNi$_5$	−28.1	−32.1	−25.1 ± 0.9	−27.4 ± 0.7	3.71	−3.75

than extrapolating $\Delta G_\mathrm{f}^\circ$ using $\Delta S_\mathrm{f}^\circ$. In this study, the experiment temperature range was 100 K, which might not be wide enough. Thus, a wider experimental temperature should be tested for a more reliable determination.

3.4   Conclusions

The two-phase coexisting potentials of (NdNi$_2$ + NdNi$_3$), (NdNi$_3$ + NdNi$_5$), and (NdNi$_5$ + Ni) were investigated at 1073–1173 K in a molten CaCl$_2$–NdCl$_3$ (1.0 mol%) system. The relative partial molar quantities and activities of Nd and Ni were calculated using the two-phase coexisting potentials. The relative partial molar Gibbs energies of Nd and Ni were used to calculate the standard Gibbs energies of formation for the Nd–Ni alloys. The obtained values were compared with those other studies that employed the CALPHAD and calorimetry.

Similar research was also carried out in a molten CaCl$_2$–DyCl$_3$ (1.0 mol%) system to investigated the two-phase coexisting potentials and the thermodynamic properties of (DyNi + DyNi$_2$), (DyNi$_2$ + DyNi$_3$), (DyNi$_3$ + DyNi$_5$), and (DyNi$_5$ + Ni).

Both the standard Gibbs energies of formation for the Nd–Ni and Dy–Ni alloys were lower than the reported values. Possible reasons for the differences were proposed and a wider experimental temperature range was suggested to obtain a more reliable determination.

References

1. Y. Du and N. Clavaguera, *Calphad,* **20**, 289 (1996).

2. M. Huang, R. W. McCallum, and T. A. Lograsso, *J. Alloy. Compd.,* **398**, 127 (2005).

3. A. Hussain, M.-A. Van Ende, J. Kim, and I.-H. Jung, *Calphad,* **41**, 26 (2013).

4. V. S. Sudavtsova, M. O. Shevchenko, M. I. Ivanov, V. G. Kudin, and N. V. Podopryhora, *Powder Metall. Met. Ceram.,* **58**, 581 (2020).

5. H. Konishi, T. Nishikiori, T. Nohira, and Y. Ito, *Electrochim. Acta,* **48**, 1403 (2003).

6. M. Li and W. Han, *Calphad,* **33**, 517 (2009).

Chapter 4

Highly Efficient and Precise Separation of Dy via Selective Electrochemical Formation of RE–Ni (RE = Nd, Dy) Alloys in Molten Salt

4.1   Introduction

In Chapter 2, the electrochemical formation potentials of RE–Ni (RE = Nd, Dy) alloys were investigated in molten $CaCl_2$–$RECl_3$ system at 1123 K. $DyNi_2$, $DyNi_3$, and $DyNi_5$ alloys have more positive formation potentials than the same types of Nd–Ni alloys, $NdNi_2$, $NdNi_3$, and $NdNi_5$, respectively. Because of the potential differences, different types Nd–Ni and Dy–Ni alloys could be formed at the same electrolysis potential. In this chapter, the potential dependence of the Nd–Ni and Dy–Ni alloy formation rates was investigated by preparing the Nd–Ni and Dy–Ni alloys at different potentials. After that, RE–Ni alloys were manufactured in a molten $CaCl_2$–$NdCl_3$ (1 mol%)–$DyCl_3$ (1 mol%) system to investigate the formation rates and the Dy/Nd separation ratios of the RE–Ni alloys. As described in Chapter 1, F^- is added to the molten salt to suppress the RE evaporation in the SEEE process. Therefore, in this Chapter, CaF_2 was added into the system to investigate the F^- effect on the alloy formation rates and the Dy/Nd separation ratios.

4.2   Experimental

The preparation method of $CaCl_2$ and the experimental apparatus are almost the same as Chapters 2 and 3. Additional information is described below.

After the individual measurements, both NdCl$_3$ and DyCl$_3$ were added to the melt at 1 mol% each for Dy/Nd separation experiments. Anhydrous CaF$_2$ (Kojundo Chemical Laboratory Co., Ltd., 99.9%) was added as a F$^-$ source at concentration 0–10 mol%. Due to the high oxide solubility of fluorides, the mullite reference electrode is not suitable as the reference electrode anymore. A Pt wire (Tanaka Kikinzoku Kogyo Corp., 99.95%, d.: 1.0 mm) immersed in the bulk melt was employed as a quasi-reference electrode in the following experiments.

4.3   Results and Discussion

Fig. 4-1 shows the cyclic voltammograms for a Ni electrode before (black curve) and after the addition of 1.0 mol% NdCl$_3$ (blue curve) or DyCl$_3$ (red curve) at 1123 K. Compared with the blank measurement, the cathodic current density increased from around 0.9 V (vs. Ca^{2+}/Ca) in the NdCl$_3$ addition system. According to the results mentioned in Chapter 2, the increase in cathodic current density in this potential region corresponds to the formation of NdNi$_5$ alloy. In addition, the larger cathodic current increasing from around 0.5 V indicates the formation of NdNi$_2$ alloy.
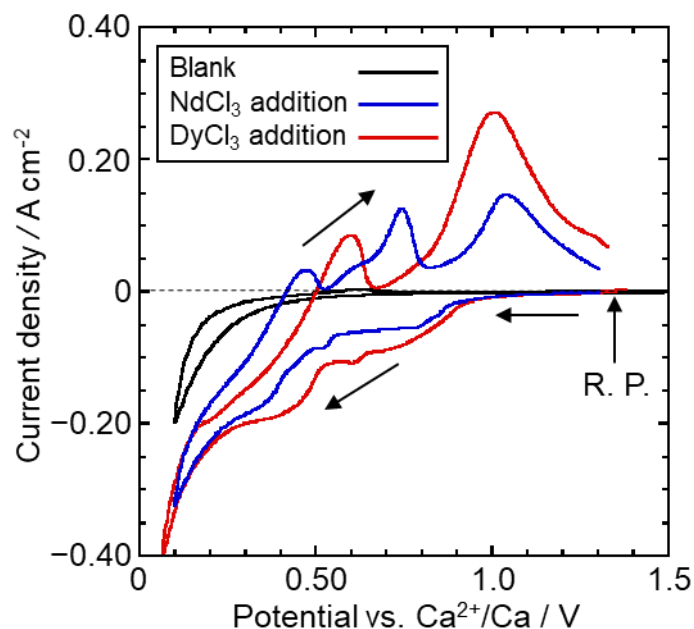
Fig. 4-1   **Cyclic voltammograms for a Ni electrode in molten CaCl$_2$ before and after the addition of 1.0 mol% NdCl$_3$ or DyCl$_3$ at 1123 K. Scan rate: 100 mV s^{-1}. R. P.: Rest potential.**

Furthermore, the current corresponding to the deposition of Nd metal is observed at 0.2 V. As for the DyCl$_3$ addition system, increases in the current density corresponding to the DyNi$_5$, DyNi$_2$, and Dy metal are observed at 1.0, 0.6, and 0.2 V, respectively. The cathodic current density at 0.2–0.8 V in the DyCl$_3$ addition system is larger than that in the NdCl$_3$ addition system, which indicates that the electrochemical formation rate of the Dy–Ni alloy in this potential range are higher than that of the Nd–Ni alloy. On the other hand, the different potentials and current densities for anode peaks indicate that the electrochemical formation potentials of the Nd–Ni and Dy–Ni alloys are different.

Based on the results of cyclic voltammetry, the Nd–Ni and Dy–Ni alloy samples were prepared in molten CaCl$_2$–NdCl$_3$ (1.0 mol%) and CaCl$_2$–DyCl$_3$ (1.0 mol%) systems at different potentials, respectively. First, Fig. 4-2 shows the cross-sectional SEM images of the samples prepared in CaCl$_2$–NdCl$_3$ system. Starting from the sample at positive electrolysis potential, no alloy formation is observed at (a) 1.0 V and (b) 0.90 V. The first observable Nd–Ni alloy is found in the sample electrolyzed at (c) 0.80 V for 60 min. The thickness of the alloy gradually increases
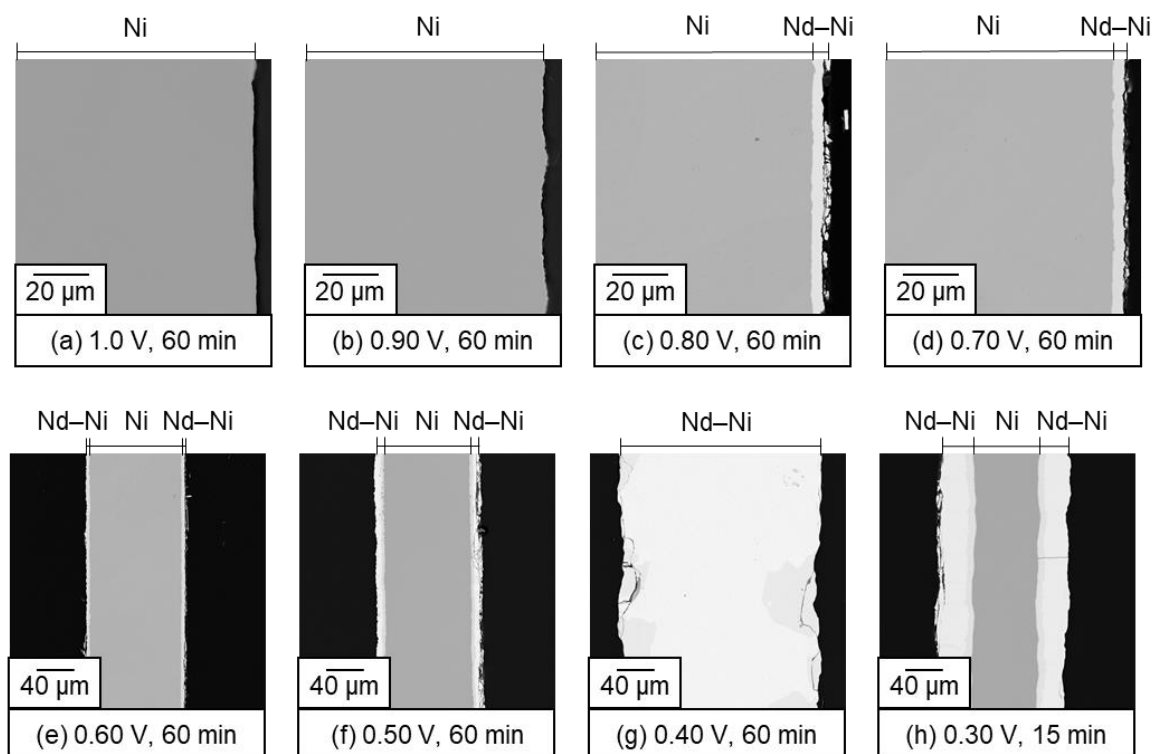
Fig. 4-2   Cross-sectional SEM images of the samples prepared by potentiostatic electrolysis with Ni electrodes at (a) 1.0 – (h) 0.30 V in molten CaCl$_2$–NdCl$_3$ (1 mol%) at 1123 K.

when the electrolysis potential is negatively shifted from (c) 0.80 V to (f) 0.50 V, and dramatically increased from (g) 0.40 V. Here, it should be noted that only the sample at (h) 0.30 V was prepared for 15 min. Secondly, Fig. 4-3 shows the cross-sectional SEM images of the samples prepared in $CaCl_2$–$DyCl_3$ system. The alloy thickness visibly increased from (b) 0.90 V and rapidly increased from (e) 0.60 V. Also, only the samples at (f) 0.50 V and (g) 0.40 V were electrolyzed for 30 and 15 min, respectively. The formation rate was simply estimated by dividing the thickness of alloy by the electrolysis time, and the results were summarized in Fig. 4-4. The blue broken line in Fig. 4-4 indicates the two-phase coexisting potential of $NdNi_2$/$NdNi_3$ and red indicates $DyNi_2$/$DyNi_3$. Obviously, the formation rate of RE–Ni alloy rapidly increased due to the formation of $RENi_2$ alloy. The formation rate of Dy–Ni alloy is higher than that of the Nd–Ni alloy at each electrolysis potential and a significant difference was observed at 0.50–0.60 V. In this potential range, $DyNi_2$ alloy is theoretically formed while $NdNi_2$ alloy is not. Should be noted that, the formation rate of the Nd–Ni alloy at 0.50 V is around 15 μm h^{-1}, which is relatively high due to the large overpotential for the formation of the $NdNi_3$ alloy. By utilizing the difference in the alloy formation
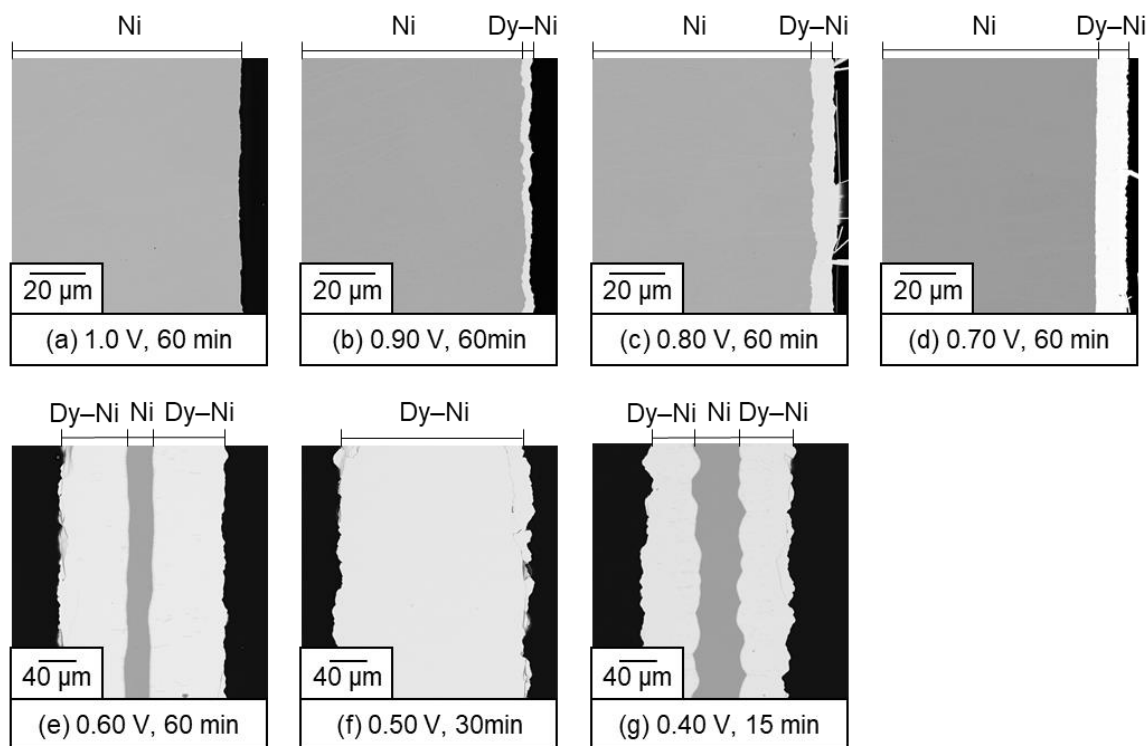
Fig. 4-3   Cross-sectional SEM images of the samples prepared by potentiostatic electrolysis with Ni electrodes at (a) 1.0 – (g) 0.40 V in molten $CaCl_2$–$DyCl_3$ (1 mol%) at 1123 K.
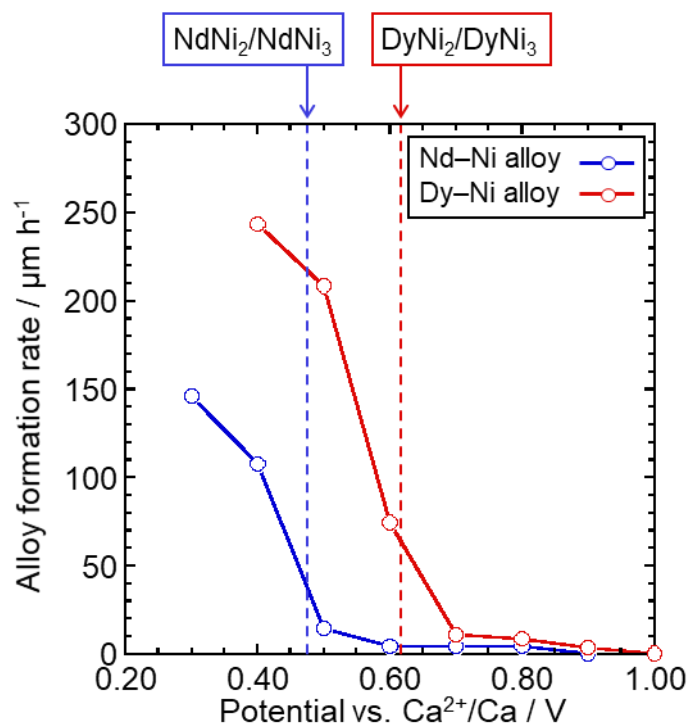
Fig. 4-4 Electrochemical formation rate of RE–Ni (RE = Nd, Dy) alloy in molten CaCl$_2$–RECl$_3$ (1 mol%) at 1123 K.

rate, a high Dy/Nd separation ratio is expected at 0.50–0.60 V.

To demonstrate the Dy/Nd separation ability, the RE–Ni alloy samples were prepared at 0.80, 0.70, 0.60, 0.50, and 0.40 V for 30 min in molten CaCl$_2$–NdCl$_3$ (1.0 mol%)–DyCl$_3$ (1.0 mol%) at 1123 K. Fig. 4-5 shows the cross-sectional SEM images and the EDX analysis of the alloy layers. The alloy thickness is small at (a) 0.80 V and (b) 0.70 V and is obviously thicker at potentials more negative than (c) 0.60 V, which can be attributed to the formation of DyNi$_2$ alloy. The molar ratio of Dy ($x_{Dy} = 28.9$ mol%) analyzed by EDX also confirmed the formation of DyNi$_2$ alloy. The alloy formation rate was estimated with the same method mentioned above and the Dy/Nd separation ratio was evaluated from the molar ratio of Dy and Nd (x_{Dy} and x_{Nd}) measured by EDX. Fig. 4-6 shows the potential dependence of the formation rate of RE–Ni alloy and the Dy/Nd separation ratio. The alloy formation rate is increased from around 10 to 160 μm h^{-1} with the potential negative shift from 0.80 V to 0.40 V. The highest Dy/Nd separation ratio of 96 is observed at 0.60 V, where the alloy formation rate is 48 μm h^{-1}. According to a private communication with the staff of a
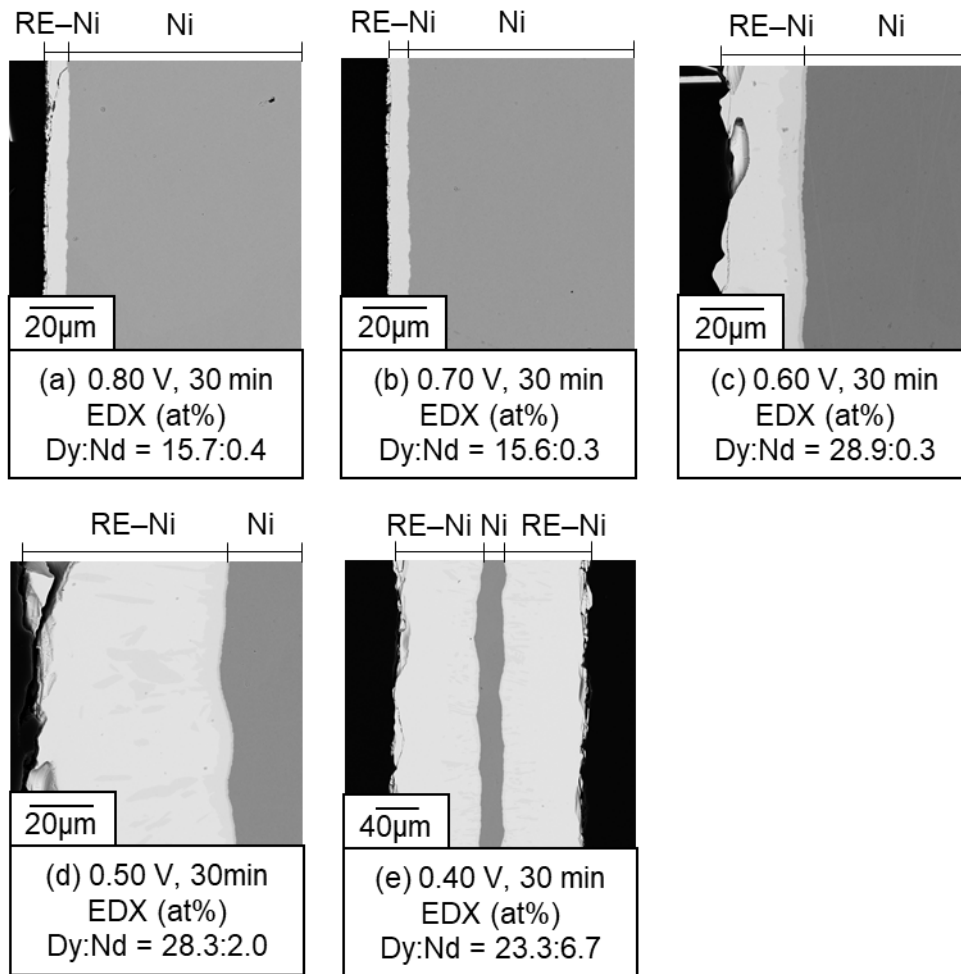
Fig. 4-5 **Cross-sectional SEM images and EDX analysis of the samples prepared by potentiostatic electrolysis with Ni electrodes at (a) 0.80 – (e) 0.40 V in molten $CaCl_2$–$NdCl_3$ (1 mol%)–$DyCl_3$ (1 mol%) at 1123 K.**

magnet manufacturer, Dy with a purity higher than 90% can be used in the production of heat-resistant Nd magnets. Therefore, if the Dy/Nd separation ratio is larger than 9, the purity requirement of Dy will be satisfied. The Dy/Nd separation ratio of 96 is as high as that obtained in LiCl–KCl system (Dy/Nd = 72) and much higher than those obtained in NaCl–KCl (Dy/Nd = 25) and LiF–CaF_2 (Dy/Nd = 5.6) systems.[1-3] A simple calculation on the processing rate is shown for an alloying rate of 50 μm h^{-1} (about 50 mA cm^{-2}): assuming a 1-m^2 Ni electrode and a current efficiency of 80%, it is possible to process 130 g of Dy (typical amount used per HEV)[4] in 10 min. The alloy formation rate of 48 μm h^{-1} is not as high as that of the LiF–CaF_2 system, but one can still expect to construct an efficient process in $CaCl_2$ system with this formation rate. At 0.50 V, the
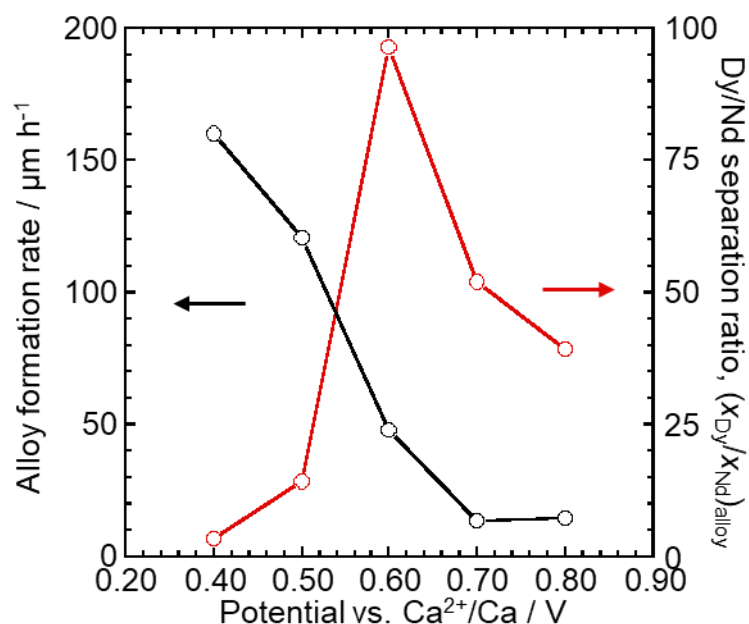
Fig. 4-6   **Electrochemical formation rate of RE–Ni (RE = Nd, Dy) alloy and the Dy/Nd separation ratio of the alloy prepared by potentiostatic electrolysis in molten CaCl₂–NdCl₃ (1 mol%)–DyCl₃ (1 mol%) at 1123 K.**

Dy/Nd separation ratio is 14 and the alloy formation rate is 121 μm h^{-1}. The Dy/Nd separation ratio is within the acceptable range and the alloy formation rate is ideal for an efficient process. As for other conditions, 0.70 V and 0.80 V have desirable Dy/Nd separation ratios but the alloy formation rates are not suited for an efficient process. The highest alloy formation rate of 160 μm h^{-1} is achieved at 0.40 V. However, the Dy/Nd separation ratio of 3 here is too low for high precision separation of Dy.

In order to investigate the effect of F$^-$ on the alloy formation rate and Dy/Nd separation ratio, CaF$_2$ was added to the system in the ratios of 0–10 mol%. The possible fluorination reactions along with the CaF$_2$ addition in this system are considered as the reactions (1) and (2):

$$NdCl_3 \ (l) + 1.5 \ CaF_2 \ (l) = NdF_3 \ (l) + 1.5 \ CaCl_2 \ (l) \qquad (1),$$

$$DyCl_3 \ (l) + 1.5 \ CaF_2 \ (l) = DyF_3 \ (l) + 1.5 \ CaCl_2 \ (l) \qquad (2).$$
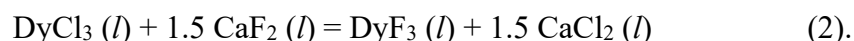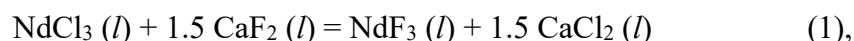
The standard Gibbs energies for the reactions (1) and (2) are −23.1 and −65.7 kJ mol^{-1} at 1123 K, respectively, according to the standard Gibbs energies of formation for NdCl$_3$, DyCl$_3$, CaCl$_2$, NdF$_3$, DyF$_3$, CaF$_2$ reported in the HSC Chemistry software.[5] Data for the salts with high melting point

were calculated by extrapolating the data of liquid phase to 1123 K. Since the standard Gibbs energies of the two reactions are both sufficiently negative and (2) is more negative than (1), the two reactions would proceed to the right and Dy^{3+} would be more fluorinated when F^- is insufficient. Since RE^{3+} is usually coordinated with six halide ions,[6,7] the addition of 3.0 mol% CaF_2 in the present system is high enough to completely coordinate Dy^{3+} with F^- in stoichiometric viewpoint. The addition of 6 mol% is the theoretical amount to completely coordinate both Nd^{3+} and Dy^{3+} with F^-. In general, for the same RE^{3+}, RE fluoride is more difficult to reduce than RE chloride.[8] In our case, the formation potential of the RE–Ni alloy from F^--coordinated RE^{3+} ions should be more negative than that from Cl^--coordinated RE^{3+} ions. Therefore, the addition of CaF_2 to the $CaCl_2$ system is considered to shift the formation potentials of the RE–Ni alloys to more negative values.

Fig. 4-7 shows the dependence of CaF_2 concentration on (a) the formation rate of RE–Ni alloy and (b) the Dy/Nd separation ratio of the alloy prepared in molten $CaCl_2$–CaF_2 (0–10 mol%)–$NdCl_3$ (1.0 mol%)–$DyCl_3$ (1.0 mol%) systems at 1123 K. As the concentration of CaF_2 increases, the alloy formation rate obviously decreases at 0.40 V and 0.50 V, and slightly decreases at 0.60 V. As mentioned above, since the addition of CaF_2 shifts the electrochemical formation potentials of RE–Ni alloys to negative values, the increase of CaF_2 concentration results in a lower overpotential and alloy formation rate compared to the electrolysis at the same potential in a pure chloride system. However, even with the addition of 10 mol% CaF_2, the formation rates of the RE–Ni alloys at 0.40, 0.50, and 0.60 V were 77, 65, and 41 $\mu m \ h^{-1}$, respectively, which were expected to construct an efficient process.

Concerning the Dy/Nd separation ratios, the values show different changing trends at 0.40, 0.50, and 0.60 V, which can be explained as follows. At 0.40 V, the Dy/Nd separation ratio is around 3 without CaF_2 addition and almost unaltered at the CaF_2 concentration up to 2 mol%. The Dy/Nd separation ratio rapidly increases with CaF_2 concentration and reaches the maximum ratio of 29 at 6 mol%. The Dy/Nd separation ratio has increased over 9, which enables highly precise
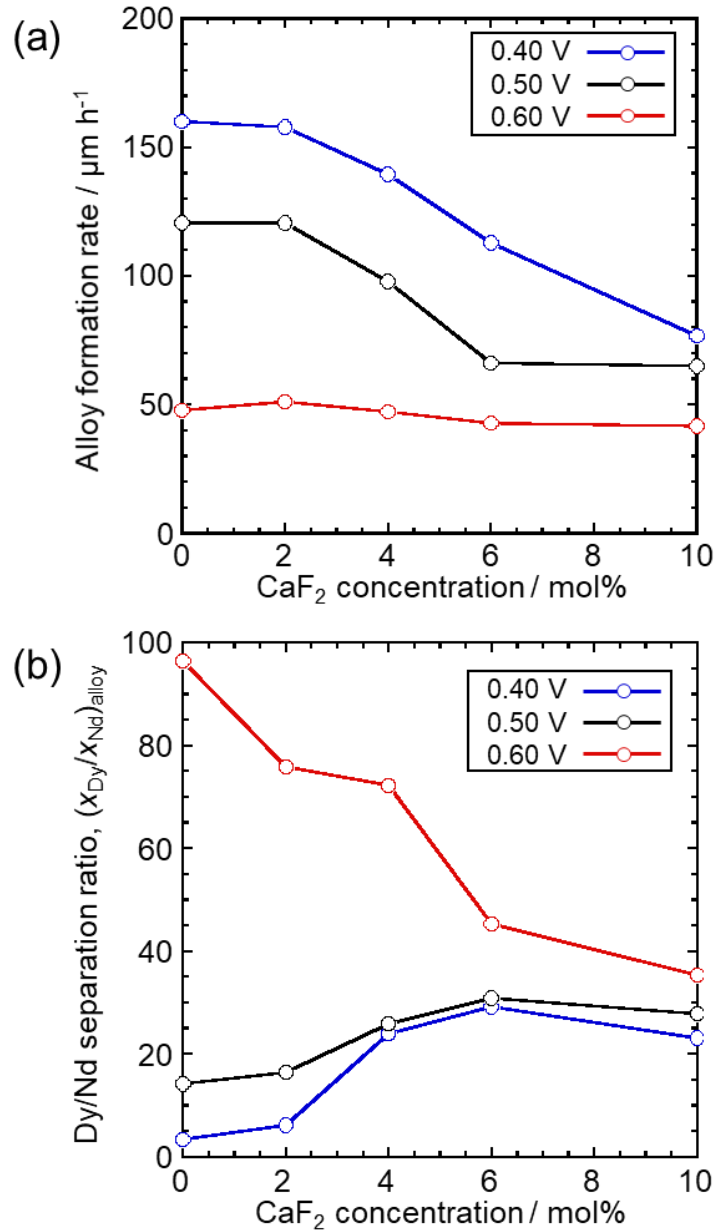
Fig. 4-7   CaF$_2$ concentration dependence of (a) the RE–Ni (RE = Nd, Dy) alloy formation rate and (b) the Dy/Nd separation ratio of the alloy prepared by potentiostatic electrolysis in molten CaCl$_2$–CaF$_2$ (0–10 mol%)–NdCl$_3$ (1 mol%)–DyCl$_3$ (1 mol%) at 1123 K.

Dy separation even at this potential. Further addition of CaF$_2$ up to 10 mol% results in a slight decrease in the Dy/Nd separation ratio to 23. As explained above, Dy^{3+} will be coordinated by F$^-$ prior to Nd^{3+}, and 3 mol% CaF$_2$ is the stoichiometric amount to where coordinate 1.0 mol of Dy^{3+} with F$^-$. The overpotential for Dy–Ni alloy formation decreases with increasing CaF$_2$ concentration up to 3 mol%. However, the formation potentials of Dy–Ni alloys are still more positive than those

of Nd–Ni alloys of the same type. Thus, the Dy/Nd separation ratio is almost unaltered when the concentration of CaF_2 is less than 3 mol%. Next, as the concentration of CaF_2 increases to 3–6 mol%, Nd^{3+} is subsequently coordinated by F^- after Dy^{3+}. Then, the overpotential used for Nd–Ni alloy formation decreases with increasing CaF_2 concentration up to 6 mol%. Since the formation potentials of the Nd–Ni alloys are more negative than those of the Dy–Ni alloys of the same type, the decrease of overpotential for the Nd–Ni alloys should have a greater influence on the Dy/Nd separation ratio. Thus, the Dy/Nd separation ratio rapidly increases within this CaF_2 concentration range. When the concentration of CaF_2 is over 6 mol%, both Nd^{3+} and Dy^{3+} are completely coordinated by F^- and the concentration of free F^- increases, which may have another influence on the Dy/Nd separation ratio. In a previous study, only a low Dy/Nd separation ratio of 5.6 was obtained in a pure fluoride system of LiF–CaF_2 at 1123 K.[3] This suggests that the high concentration of free F^- in the molten salt is unfavorable for the Dy/Nd separation. Almost the same trend as 0.40V is observed at 0.50V. The Dy/Nd separation ratio is 14, 31, and 28 at the CaF_2 concentration of 0, 6, and 10 mol%, respectively.

In contrast, a changing trend of Dy/Nd separation ratio is different at 0.60 V. The ratio decreases with CaF_2 addition, and remains still relatively high as 35 even at 10 mol%. The reason for the monotonically decreasing trend of Dy/Nd separation ratio can be attributed to the fact that the formation rate of the Nd–Ni alloy is already extremely low at 0.60 V even without CaF_2 addition as shown in Fig. 4-4. As a result, the formation rate of Nd–Ni alloy remains low and cannot be further decreased with the addition of CaF_2. Thus, at 0.60 V, the Dy/Nd separation ratio decreases with increasing the CaF_2 concentration, first because the overpotential for the Dy–Ni alloy formation decreases, and then because the free F^- concentration increases above 6 mol%.

From the above results, both of high Dy/Nd separation ratio and the formation rate of RE– Ni alloy are attainable at 0.40–0.60 V and CaF_2 concentration of 6 mol%. The Dy/Nd separation ratios are high enough at 29–45 for highly precise Dy separation, and simultaneously the formation rates are as high as 43–113 μm h^{-1}. The fact that such high evaluation index was achieved indicates

that an efficient process can be constructed using this molten salt system.

4.4　Conclusions

The formation rates of Nd–Ni and Dy–Ni alloys were estimated at various potentials at 1123 K. At both 0.50 V and 0.60 V, a large difference in the alloy formation rate between Nd–Ni and Dy–Ni alloys is observed, suggesting a high Dy/Nd separation ratio. The alloy formation rate and Dy/Nd separation ratio were measured using molten $CaCl_2$ containing the same concentrations of $NdCl_3$ and $DyCl_3$. The maximum Dy/Nd separation ratio of 96 was obtained at 0.60 V with an alloy formation rate of 48 μm h^{-1}. Although the highest alloy formation rate of 160 μm h^{-1} was obtained at 0.40 V, the Dy/Nd separation ratio was as low as 3.

The effect of F$^-$ is then investigated by adding CaF_2 to the $CaCl_2$ melt. The alloy formation rate decreases with increasing CaF_2 concentration and the effect is relatively stronger at negative electrolysis potentials. As for the Dy/Nd separation ratio, a specific phenomenon was observed. The Dy/Nd separation ratio at 0.60 V decreases with increasing CaF_2 concentration, and remains relatively high as 35 even at 10 mol%. On the other hand, at 0.40 V, the Dy/Nd separation ratio increases with CaF_2 concentration, reaching a maximum value of 29 at 6 mol%, with a high alloy formation rate of 113 μm h^{-1}. Then, as the CaF_2 concentration increases to 10 mol%, the separation ratio decreases slightly to 23. This change in the Dy/Nd separation ratio is explained as follows: with increasing CaF_2 concentration, Dy^{3+} is preferentially coordinated by F$^-$ first, followed by Nd^{3+}, which changes the overpotential used for alloy formation and changes the alloy formation rate. It is found that highly efficient and precise Dy separation is expected by the RE–Ni alloy formation in the molten $CaCl_2$–CaF_2 system.

References

1. H. Konishi, H. Ono, T. Nohira, and T. Oishi, *ECS Trans.,* **50**, 463 (2012).

2. K. Yasuda, K. Kondo, S. Kobayashi, T. Nohira, and R. Hagiwara, *J. Electrochem. Soc.,* **163**, D140 (2016).

3. T. Nohira, S. Kobayashi, K. Kondo, K. Yasuda, R. Hagiwara, T. Oishi, and H. Konishi, *ECS Trans.,* **50**, 473 (2012).

4. O. Takeda and T. H. Okabe, *Metall. Mater. Trans. E,* **1**, 160 (2014).

5. A. Roine and P. Kobylin, *HSC Chemistry®*, ver 9, Outotec Information Center, Pori, Finland (2016).

6. V. Dracopoulos, B. Gilbert, and G. N. Papatheodorou, *J. Chem. Soc., Faraday Trans.,* **94**, 2601 (1998).

7. T. Uda, T. Fujii, Y. Iwadate, A. Uehara, and H. Yamana, *Z. Anorg. Allg. Chem.,* **639**, 765 (2013).

8. K. Fujita, A. Nezu, H. Akatsuka, and H. Matsuura, Proceedings of 4th Asian Conference on Molten Salt Chemistry and Technology, and 44th Sympoisium on Molten Salt Chemistry, Japan, Matsushima, (2012).

Chapter 5

Selective Extraction-Evaporation-Electrolysis (SEEE) Process for Highly Efficient and Precise Separation Recycling of RE Elements from Magnet Scrap in Molten Salt

5.1   Introduction

In Chapters 2 and 4, the electrochemical formation potentials, formation rates, and Dy/Nd separation ratios of RE–Ni (RE = Nd, Dy) alloys were investigated in molten $CaCl_2$–$RECl_3$ and $CaCl_2$–CaF_2–$RECl_3$ systems. When alloy samples were prepared at specific potentials, Dy could be selectively separated from the molten salt containing equal amounts of $NdCl_3$ and $DyCl_3$. A specific phenomenon was observed in which the Dy/Nd separation ratio at 0.40 V and 0.50 V increased with the addition of CaF_2 until the F/RE ratio increased to 6.

As described in Chapter 1, the SEEE process consists of (A) selective extraction, (B) selective evaporation, and (C) selective electrolysis steps. In this chapter, all steps of the SEEE process were experimentally investigated. Commercial heat-resistant Nd magnets were used to simulate Nd magnet scrap. $MgCl_2$ and CaF_2 were added as an extraction agent and an RE evaporation inhibitor, respectively. First, RE extraction ratios, RE evaporation ratios, and Mg evaporation ratios were investigated after sequential experiments of the extraction step and the evaporation step. In a previous study,[1] RE elements in a molten $MgCl_2$ were recovered by evaporation of RE chlorides. However, in the present study, the extracted RE elements were

expected to remain in the molten salt for electrolysis separation. Thus, the removal of Mg components and the remaining of RE components are important in these steps. Then, RE–Ni alloys were prepared in molten salts containing RE ions with the similar proportion of RE components as the commercial heat-resistant Nd magnets or Nd magnets used in BEVs/HEVs motors. Several RE alloy samples were prepared at different potentials to investigate the suitable conditions for the enrichment of Dy using Ni electrode.

5.2   Experimental

5.2.1   RE Extraction and Mg Evaporation

Before the experiment, heat-resistant Nd magnets (Niroku Seisakusho Co., Ltd., NE206, diameter: 10 mm, thickness: 2 mm) were demagnetized by heat treatment at 773 K for 1 h under vacuum. The composition of the magnet was analyzed by ICP-AES (AMETEK, Inc., SPECTROBLUE) after dissolution in nitric acid (FUJIFILM Wako Pure Chemical Corp., Wako 1st Grade), and was found to be 0.9 wt.% B, 1.0 wt.% Cu, 66.5 wt.% Fe, 2.3 wt.% Ni, 20.3 wt.% Nd, 6.6 wt.% Pr, and 2.4 wt.% Dy. Ni and Cu were detected because they were used as the coating materials. Each magnet was broken in half by using two pliers to expose the Nd magnet surface and added into powdery $CaCl_2$–$MgCl_2$ (Kojundo Chemical Laboratory Co., Ltd., 99.9%) mixture. To prevent the evaporation of the extracted RE halides, 2, 4, and 6 mol% of CaF_2 were added to the mixture. The amount of molten salt system was set so that the RE concentration would be 2 mol% when all the RE contained in the magnet was extracted. All the substances were introduced into a graphite crucible (Sanko Co., Ltd., IG-110, inner diameter: 49 mm, height: 150 mm) and dehydrated in a vacuum oven at 453 K for 72 h, and then placed at the bottom of a stainless-steel vessel in an airtight Kanthal container for further dehydration under vacuum at 773 K for 24 h. After the dehydration, the Kanthal container was replenished with Ar gas and the temperature was raised to 1123 K and kept for 20 h to complete the RE extraction reaction. After 20 h, the temperature was raised to 1273 K and kept under vacuum for 3 h to remove unreacted $MgCl_2$ and

by-product Mg. The magnet and molten salt were cooled down to room temperature and recovered by crashing the crucible. The magnet was washed by water and dried in a vacuum oven at 453 K. One piece of magnet was embedded in resin and polished to expose the cross-section and then analyzed by SEM and EDX. The analysis methods were almost the same as described in Chapter 2. Another piece of magnet was dissolved with nitric acid and then analyzed by ICP-AES. A portion of the recovered salt that did not contain CaF_2 was ground in a ceramic mortar and subjected to ICP-AES analysis using the same method as the magnet. When CaF_2 was contained in the recovered salts, the components were analyzed by an analysis company (TECHNO SCIENCE Corp.). XRD analysis was carried out for the magnets before and after the extraction experiment. In addition, substances were collected from the low temperature part of the top of the container after RE extraction and analyzed by XRD.

5.2.2 Electrolysis Separation of Dy and Nd

The preparation method of molten salts and the experimental apparatus are almost the same as Chapter 4. Additional information is described below.

The magnet used in the RE extraction experiment contains Nd, Dy, and Pr as RE elements. Because the chemical property of Pr is very similar to that of Nd, the electrolysis separation experiment was conducted in molten salt systems that contained only Nd and Dy to simplify the experiments. Two molten salt systems were prepared in the experiments. The first molten salt was $CaCl_2$–CaF_2 (6.00 mol%)–$NdCl_3$ (1.83 mol%)–$DyCl_3$ (0.17 mol%). The Dy/Nd ratio was 0.09, which is similar to the Dy/Nd ratio of the commercial heat-resistant Nd magnet used in the RE extraction experiment. The second molten salt was $CaCl_2$–CaF_2 (9.00 mol%)–$NdCl_3$ (2.00 mol%)–$DyCl_3$ (1.00 mol%). The Dy/Nd ratio was set to 0.5 so that the system simulated the ratio in the Nd magnets used in the motors of BEVs/HEVs. Samples prepared in the two systems were analyzed by XRD and SEM/EDX.

5.3　Results and Discussion

5.3.1　RE Extraction and Mg Evaporation

5.3.1.1　Analysis on Nd Magnets

Fig. 5-1 shows (a) a photo, (b) an XRD pattern, and (c) a cross-sectional SEM image of the commercial heat-resistant Nd magnet. A metallic luster layer was observed covering the magnet. According to the ICP-AES and EDX analysis, this layer was a surface coating of Cu–Ni alloy. In the molten salt system used in the experiment, both Cu and Ni do not react with $MgCl_2$ due to their thermodynamic properties, thus the magnet was broken in half to expose the Nd magnet phase before the RE extraction experiment. The broken Nd magnets were powdered and then subjected to XRD analysis, wherein $Nd_2Fe_{14}B$ was observed as the main phase. From the cross-sectional SEM image, the Nd magnet alloy was found to be dense and consisted of the main Fe-rich phase and the RE-rich phase. The grey part was the Fe-rich phase with (Nd+Pr) concentrations of 10–15 at% and the white part was the RE-rich phase with (Nd+Pr) concentrations of higher than 90 at%. Since the energies of characteristic X-rays for Dy and Fe are close, the Dy concentration could not be accurately measured by EDX. The Fe-rich phase was considered to be the $Nd_2Fe_{14}B$ phase.

After extraction of the RE component in the magnet with different concentrations of $MgCl_2$ and evaporation of by-product Mg, the magnets were also analyzed in the same way. As an example, Fig. 5-2 shows (a) a photo, (b) an XRD pattern, and (c) a cross-sectional SEM image of the Nd magnet after RE extraction by 3 mol% $MgCl_2$ in molten $CaCl_2$ at 1123 K for 20 h and Mg evaporation by vacuum at 1273 K for 3 h. When Fig. 5-2(a) is compared with Fig. 5-1(a), the volume of the magnet hardly changed after the RE extraction and Mg evaporation. The XRD pattern of the magnet after the RE extraction was identified as Fe, indicating that almost all RE was extracted out from the magnet. Although the existence of B was not confirmed by XRD, B component is expected to remain in the solid phase as Fe–B (s) alloy according to the reaction (1) of the RE extraction in a similar condition.[1]

$$RE_2Fe_{14}B \ (s) + 3 \ MgCl_2 \ (l) = 2 \ RECl_3 \ (l) + Fe–B \ (s) + 3 \ Mg \ (l) \qquad (1).$$
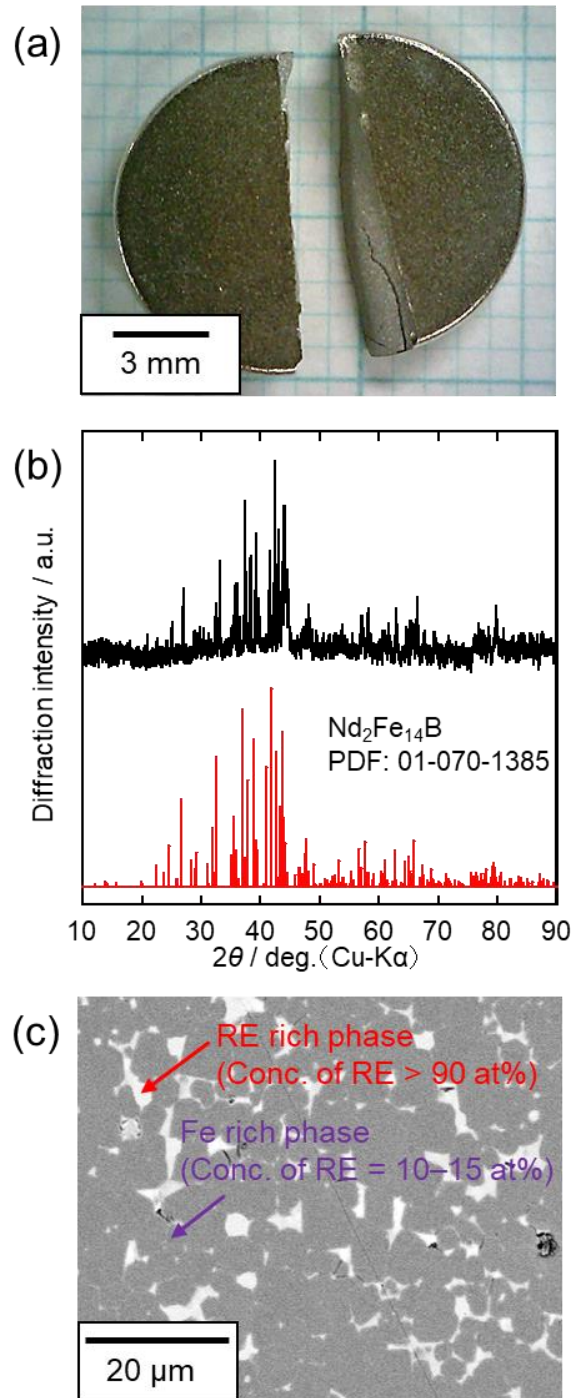
Fig. 5-1 **(a) A photo, (b) an XRD pattern, and (c) a cross-sectional SEM image of the commercial heat-resistant Nd magnet before RE extraction.**

The cross-sectional SEM image shows the existence of many pores and the decrease in the amount of RE-rich phase. The average concentrations of Nd and Pr analyzed by EDX were less than 0.1 at%. The concentration of Dy could not be accurately measured due to the same reason mentioned above. Since the concentrations of Nd and Pr decreased close to 0 at%, it is considered that the RE
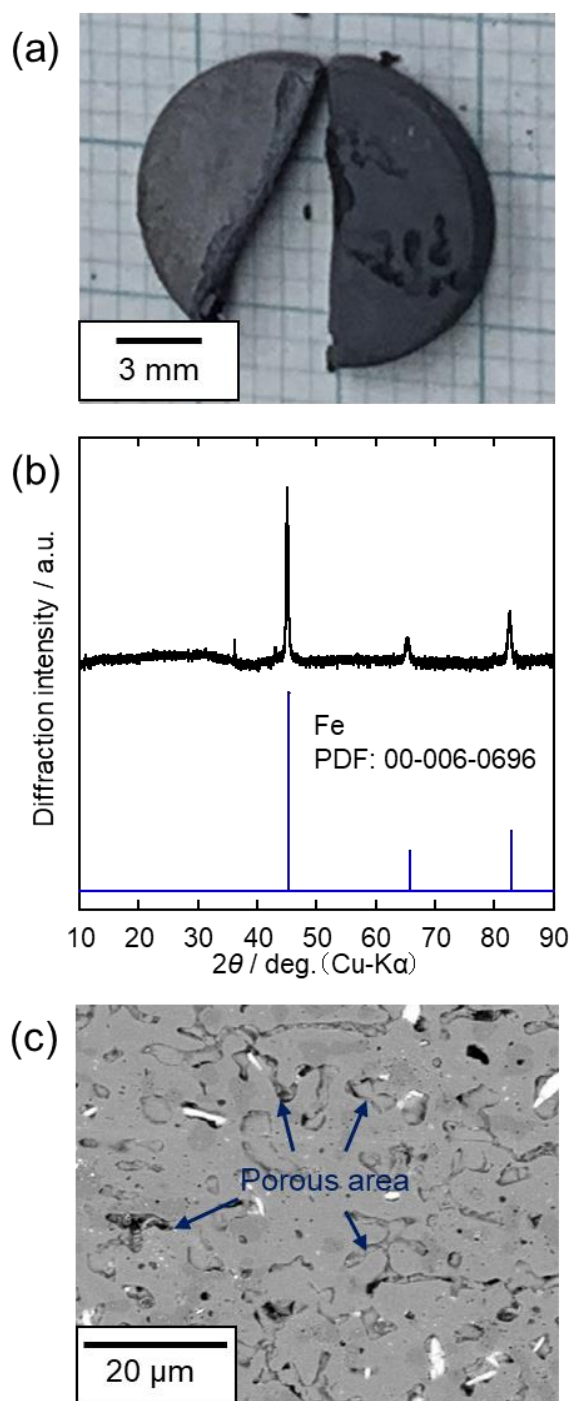
Fig. 5-2 **(a) A photo, (b) an XRD pattern, and (c) a cross-sectional SEM image of the commercial heat-resistant Nd magnet after RE extraction by 3 mol% MgCl₂ in molten CaCl₂ at 1123 K for 20 h and Mg evaporation by vacuum at 1273 K for 3 h.**

contained in the magnet was almost completely extracted.

The extraction ratios of RE were measured from the changes in concentrations of RE in the magnet before and after the reaction calculated from the results of ICP-AES analysis listed in Table

5-1. Here, since Fe does not react with $MgCl_2$, the concentrations of RE are shown as the mass ratios with respect to Fe. In the initial magnet, the concentration of Dy, Nd, and Pr were 36.0, 304.4, and 99.0 mg $(g\text{-Fe})^{-1}$, respectively. According to the reaction (1) described above, the stoichiometric amount of Mg^{2+} consumed in the RE extraction is 1.5 times that of RE. Since the amounts of RE contained in the magnet corresponded to 2 mol% of the molten salt, 3 mol% of Mg^{2+} was necessary to achieve complete extraction of RE from the magnet. For samples #1, #2, and #3, the added amounts of $MgCl_2$ were 1, 2, and 5 times the stoichiometric amount for 100% extraction of RE, respectively.

When 1 times $MgCl_2$ was added (sample #1), the concentrations of Dy, Nd, and Pr were 2.5, 8.2, and 2.2 mg $(g\text{-Fe})^{-1}$, which correspond to the extraction ratios of Dy, Nd, and Pr as 93%, 97%, and 98%, respectively. Here, the RE extraction reaction (1) is treated in a simplified form as reaction (2) for thermodynamic considerations:

$$2 \text{ RE } (s) + 3 \text{ MgCl}_2 \ (l) = 2 \text{ RECl}_3 \ (l) + 3 \text{ Mg } (l) \qquad (2).$$
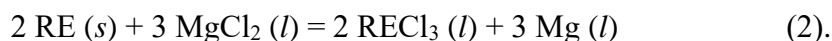
The standard Gibbs energies of reaction (2) are -70.1, -135.5, and -164.9 kJ mol^{-1} at 1123 K when RE = Dy, Nd, and Pr, respectively.[2] In experiment #1, RE and $MgCl_2$ were present as per the

Table 5-1 **Concentration of RE in the Nd magnets before and after RE extraction at 1123 K for 20 h and Mg evaporation by vacuum at 1273 K for 3 h in molten $CaCl_2$–CaF_2–$MgCl_2$ (No. 1–6).**

Sample No.	Conc. of added salts / mol%		Conc. in Nd magnets / mg $(g\text{-Fe})^{-1}$			Extraction ratio / %		
	$MgCl_2$	CaF_2	Dy	Nd	Pr	Dy	Nd	Pr
Initial magnet	–	–	36.0	304.4	99.0	–	–	–
1	3	0	2.5	8.2	2.2	93	97	98
2	6	0	1.3	4.2	0.6	96	99	99
3	15	0	1.5	4.6	0.6	96	99	99
4	6	2	2.3	7.2	1.7	94	98	98
5	6	4	3.0	8.5	2.4	92	97	98
6	6	6	2.1	6.5	1.6	93	98	98

stoichiometric amounts in reaction (2) before the reaction. The activities of $MgCl_2$ and $RECl_3$ at equilibrium after the reaction were calculated. The activities of RE and Mg were taken to be 1, and the initial activities of $MgCl_2$ and $RECl_3$ were taken to be 0.03 and 0, respectively. Here, the activity coefficients of $MgCl_2$ and $RECl_3$ were assumed to be 1. The activities of $DyCl_3$, $NdCl_3$, and $PrCl_3$ would be 0.0165, 0.0196, and 0.0199, respectively, when the reaction (2) equilibrates. Since the RE in the magnet corresponds to 2 mol% of the molten salt, when all the RE is extracted, the activity of $RECl_3$ corresponds to 0.02. Therefore, the extraction ratios of Dy, Nd, and Pr are thermodynamically calculated to be 82.5%, 98.0%, and 99.5%, respectively. The calculated extraction ratios of Nd and Pr are almost consistent with the experimental values of sample #1, but the calculated extraction ratio of Dy is lower than the experimental value, which may be due to the slightly small activity coefficient of $DyCl_3$ in this system.

On the other hand, when 100% of the RE is extracted, $RECl_3$ is 2 mol%, which corresponds to an activity of 0.02. In reaction (2), the activities of $MgCl_2$ in equilibrium with $RECl_3$ of activity 0.02 are 0.0060, 0.0006, and 0.0002 for RE = Dy, Nd, and Pr, respectively. Here, the initial amounts of $MgCl_2$ required are 0.0360, 0.0306, and 0.0302 in terms of the activity. These correspond to 1.20, 1.02, and 1.01 times of stoichiometric amounts. When the added amount of Mg^{2+} increased to 2 times (sample #2), the reaction (2) should sufficiently proceed to the right. Thus, the extraction ratios of Dy, Nd, and Pr were slightly increased to 96%, 99%, and 99%, which should be the extraction limit of RE in this system due to the over addition of $MgCl_2$.

To verify that the extraction limit of RE was reached, an experiment with the addition of 5 times $MgCl_2$ was performed (sample #3). Since the extraction ratios of RE were almost unaltered, the extraction limit of RE was already reached when $MgCl_2$ was added 2 times.

In order to suppress the evaporation of RE compounds, CaF_2 was added into the molten salt system to fluorinate the RE elements and decrease their vapor pressure. The influence of the addition of CaF_2 on the RE extraction was investigated from samples #2 and #4–6 prepared at different amounts of CaF_2 addition (0, 2, 4, and 6 mol%). Here, 6 mol% of CaF_2 is the

stoichiometric amount of F^- for octahedral coordination of all RE ions in this system. From the results of four samples, the extraction ratios of Dy, Nd, and Pr were slightly decreased by the CaF_2 addition, but still high and close to 100%. Therefore, the influence is small when the F^- concentration is not higher than 6 times of the RE concentration in molar ratio.

From the ICP-AES results of the initial and remained magnets listed in Table 5-1, the extraction of RE can be evaluated. However, it was not clear whether the components remained or volatilized after the reaction only from the above analysis. ICP-AES analyses of the remaining salt after the reaction is also necessary to evaluate the evaporation behavior. Especially, the remaining of $MgCl_2$ in the molten salt should be avoided because the electrodeposition of metallic Mg could be preferentially occurred prior to the electrochemical formation of RE–Ni alloys in the electrolysis step.

5.3.1.2 Analysis on Molten Salts and Evaporates

The influence of the addition of F^- on the evaporation behavior of each component was analyzed in details by ICP-AES analysis of the remaining salts in experiments #2 and #4–6. The amounts of Dy, Nd, Pr, and Mg contained in the salts were calculated by the ICP-AES results. The evaporation ratios of RE (R_{RE}) and Mg (R_{Mg}) were calculated by the equations (3) and (4):

$$R_{RE} = (1 - (W_{RE(\text{in molten salt})}/W_{RE(\text{extracted from magnet})})) \times 100\% \qquad (3),$$

$$R_{Mg} = (1 - (W_{Mg(\text{in molten salt})}/W_{Mg(\text{initially added})})) \times 100\% \qquad (4),$$

where $W_{RE(\text{in molten salt})}$ and $W_{Mg(\text{in molten salt})}$ are the mass of RE and Mg contained in the remaining salts after evaporation, $W_{RE(\text{extracted from magnet})}$ is the mass change of RE in magnet calculated from data listed in Table 5-1, and $W_{Mg(\text{initially added})}$ is the mass of Mg contained in the initially added $MgCl_2$. Fig. 5-3 shows the evaporation ratios of Dy, Nd, Pr, and Mg from molten $CaCl_2$–CaF_2 (0–6 mol%)–$MgCl_2$ (6 mol%) after RE extraction at 1123 K for 20 h and Mg/$MgCl_2$ evaporation at 1273 K for 3 h. When CaF_2 was not added, the evaporation ratios of Dy, Nd, Pr, and Mg were 90%, 77%, 73%, and 94%, respectively. The evaporated species are considered to be $DyCl_3$, $NdCl_3$, $PrCl_3$,
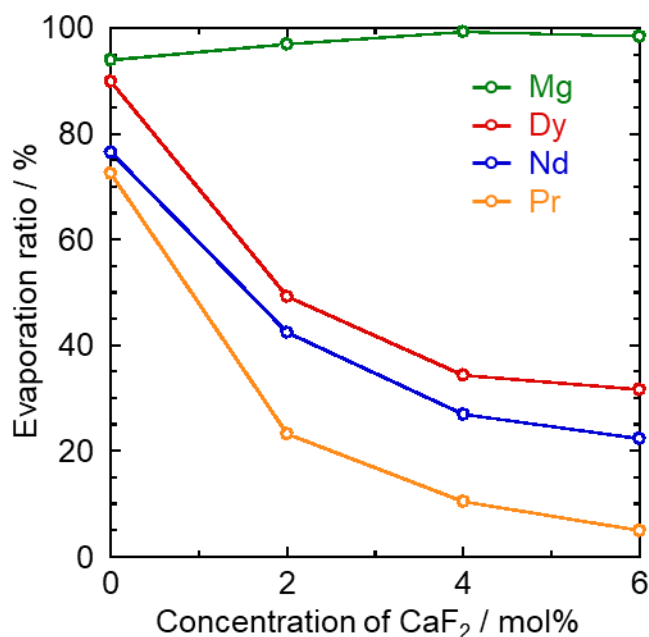
Fig. 5-3 **Evaporation ratios of Dy, Nd, Pr, and Mg from molten CaCl$_2$–CaF$_2$ (0–6 mol%)–MgCl$_2$ (6 mol%) after RE extraction at 1123 K for 20 h and Mg evaporation at 1273 K for 3 h.**

Mg, and MgCl$_2$. Although Mg component was almost completely removed, the loss of RE elements was also high. When the concentration of CaF$_2$ was increased, the evaporation ratios of Dy, Nd, and Pr were effectively suppressed while that of Mg remained almost the same: the values of Dy, Nd, Pr, and Mg were 32%, 22%, 5%, and 99%, respectively at the CaF$_2$ concentration of 6 mol%. The suppression of RE evaporation can be explained by formation of low-vapor-pressure stable octahedral F$^-$-coordinated RE ions, i.e. DyF$_6^{3-}$, NdF$_6^{3-}$ and PrF$_6^{3-}$, which were explained in Chapters 1 and 4.

$$RECl_3 \ (l) + 3\ CaF_2\ (l) \rightarrow REF_6^{3-} + 3\ Ca^{2+} + 3\ Cl^- \qquad (5).$$
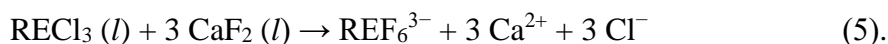
Further suppression of RE evaporation can be expected by changing the amount of CaF$_2$ added, evaporation temperature, evaporation time, and vacuum degree. On the other hand, the evaporation of Mg species was high due to the existence of high-vapor-pressure MgCl$_2$ when reaction (6) was in equilibrium.

$$MgCl_2\ (l) + CaF_2\ (l) = MgF_2\ (l) + CaCl_2\ (l) \qquad (6).$$
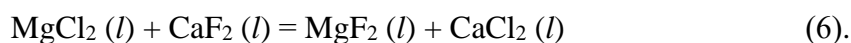
Although the standard Gibbs energy of the reaction (6) is −51.0 kJ mol^{-1} at 1123 K.[2] The reaction

would proceed to the left due to the continuous evaporation and removal of $MgCl_2$.

Fig. 5-4 shows (a) a photo and (b) an XRD pattern for evaporates collected from the low temperature part of the top of container after RE extraction at 1123 K for 20 h without the vacuum evaporation step. The main phases of the substance were identified as Mg and MgO, indicating that the evaporated Mg had solidified and a part of the Mg had been oxidized by air exposure. The fact that Mg was evaporated and recovered without a vacuum evaporation step indicates that the by-product Mg along with the RE extraction easily evaporates even at 1123 K without vacuum.

$$2 \text{ RE } (s, \text{ in magnet}) + 3 \text{ MgCl}_2 \text{ } (l) \rightarrow 2 \text{ RECl}_3 \text{ } (l) + 3 \text{ Mg } (g) \qquad (7).$$
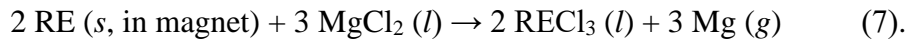
In the SEEE process, the evaporated Mg species can be reused as the RE extraction agent ($MgCl_2$) after the chlorination by Cl_2 gas formed at the next step.
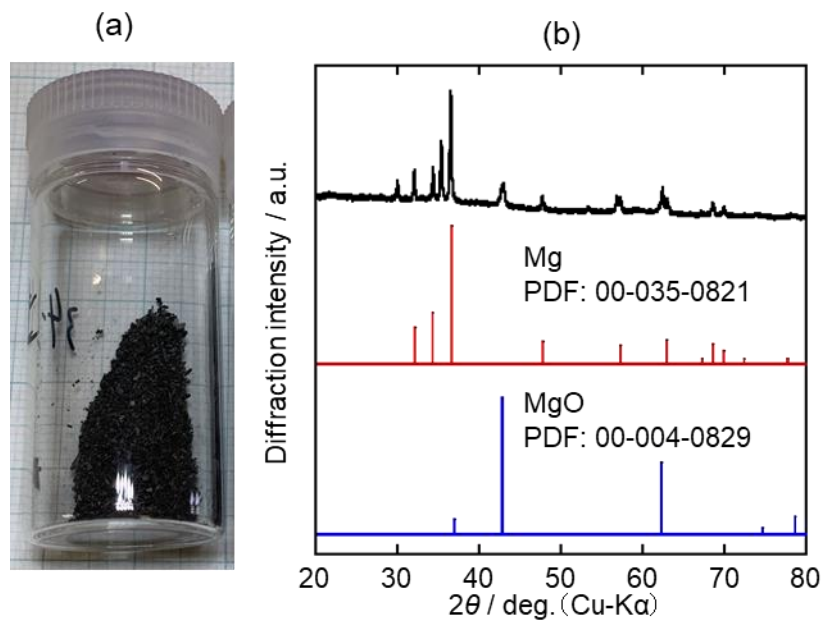
Fig. 5-4   **(a) A photo and (b) an XRD pattern for evaporates collected from the low temperature part of the top of container after RE extraction in a molten $CaCl_2$–$MgCl_2$ (3 mol%) system at 1123 K for 20 h.**

5.3.2   Electrolysis Separation of Dy and Nd

First, in order to investigate the RE separation ability from low Dy/Nd ratio magnets, a molten $CaCl_2$–CaF_2 (6.00 mol%)–$NdCl_3$ (1.83 mol%)–$DyCl_3$ (0.17 mol%) system was prepared,

which had the similar Dy/Nd molar ratio of 0.09 as the commercial heat-resistant Nd magnet. Several samples were prepared by potentiostatic electrolysis with Ni electrodes at 0.40–0.60 V for 30 min at 1123 K. As a typical sample, (a) a cross-sectional SEM image with EDX analysis results and (b) an XRD pattern of the sample at 0.50 V are shown in Fig. 5-5. A RE–Ni alloy layer was formed at the surface of Ni electrode. By dividing the thickness of the alloy layer with the electrolysis time, the alloy formation rate was calculated to be 47 μm h^{-1}. The components of the alloy layer analyzed by EDX were 20.2 at% Dy, 10.9 at% Nd, and 68.9 at% Ni. The molar ratio of (Dy+Nd):Ni = 31.1:68.9, which is close to the molar ratio of RENi$_2$. The XRD analysis also confirmed that the alloy layer was RENi$_2$. The Dy/Nd ratio was calculated to be 1.9, which

Fig. 5-5 **(a) A cross-sectional SEM image with EDX analysis results and (b) an XRD pattern of the sample obtained by potentiostatic electrolysis with a Ni electrode at 0.50 V for 30 min in a molten CaCl$_2$–CaF$_2$ (6.00 mol%)–NdCl$_3$ (1.83 mol%)–DyCl$_3$ (0.17 mol%) system at 1123 K.**

corresponds to approximately 21 times enrichment compared to the initial Dy/Nd ratio in the molten salt system.

$$f_{enrich} = \frac{x_{Dy}(alloy)/x_{Nd}(alloy)}{x_{Dy}(molten\ salt)/x_{Nd}(molten\ salt)} \qquad (8).$$

Here, f_{enrich} is enrichment factor of the electrolysis, x_{Dy} and x_{Nd} are the molar concentration of Dy and Nd, respectively, in the alloy or molten salt. Samples obtained at other potentials were also analyzed by the same method. Fig. 5-6 shows the potential dependence of (a) the formation rate of RE–Ni alloys, (b) the concentration of RE and the Dy/Nd ratio in RE–Ni alloys. The concentration
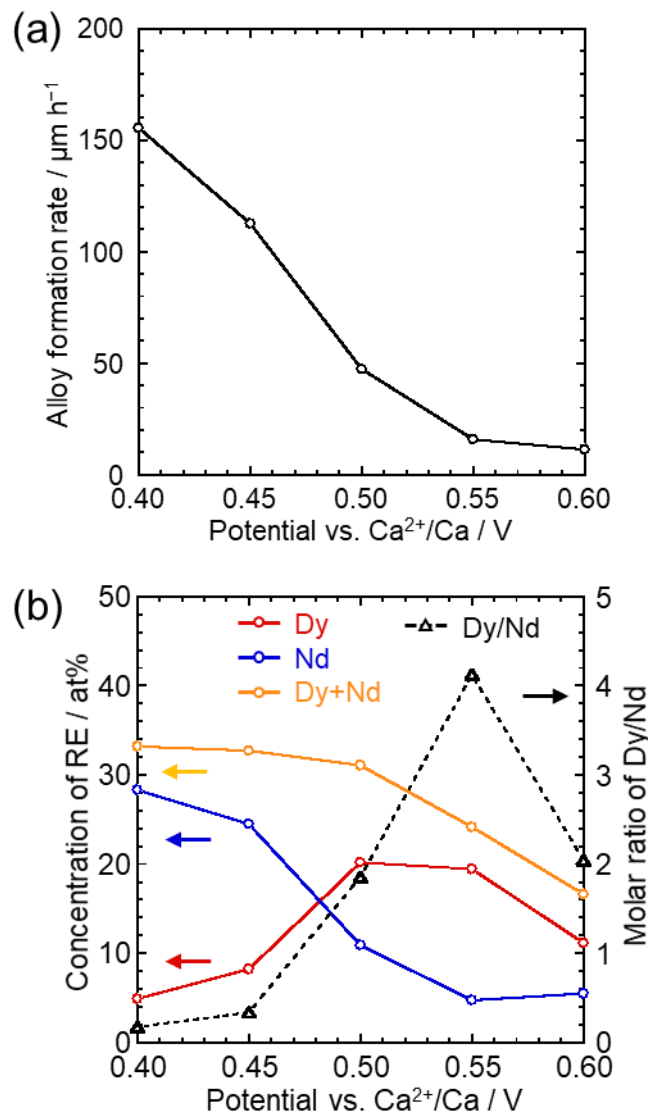
Fig. 5-6   **Potential dependence of (a) RE–Ni alloy formation rate, (b) concentration of RE and Dy/Nd ratio in the RE–Ni alloys. Samples obtained by potentiostatic electrolysis with Ni electrodes at various potentials for 30 min in a molten $CaCl_2$–CaF_2 (6.00 mol%)–$NdCl_3$ (1.83 mol%)–$DyCl_3$ (0.17 mol%) system at 1123 K.**

of (Dy+Nd) suggested that RENi$_5$ was formed at 0.60 V and RENi$_3$ at 0.55 V. Although the Dy/Nd ratios at these potentials are higher than that of the alloy obtained at 0.50 V, the alloy formation rates, 11 and 16 μm h^{-1}, are too low to meet the efficient processing requirement. As for 0.45 V and 0.40 V, the alloy formation rates are high at 113 and 155 μm h^{-1}, but the Dy/Nd ratios of 0.3 and 0.2 are too low. Considering the formation rate of 47 μm h^{-1} and the Dy/Nd ratio of 1.9, 0.50 V is expected to be a suitable potential for Dy enrichment in this system. Although the approximately 21 times enrichment was achieved, the Dy/Nd ratio of 1.9 does not meet the high precision Dy separation requirement.

Secondly, to investigate the ability to separate RE from magnet used in the motor of BEVs/HEVs, a molten CaCl$_2$–CaF$_2$ (9.00 mol%)–NdCl$_3$ (2.00 mol%)–DyCl$_3$ (1.00 mol%) system was prepared. In a similar manner, several samples were prepared by potentiostatic electrolysis with Ni electrodes at 0.40–0.60 V for 30 min at 1123 K. Fig. 5-7 shows (a) a cross-sectional SEM image with EDX analysis results and (b) an XRD pattern of the sample at 0.60 V. The alloy formation rate was calculated to be 65 μm h^{-1} and the components of the alloy layer analyzed by EDX were 29.3 at% Dy, 0.7 at% Nd, and 70.0 at% Ni. Both of the alloy composition and XRD analysis confirmed the formation of RENi$_2$. The Dy/Nd ratio of 42 for the alloy corresponds to 84 times enrichment compared to the initial Dy/Nd ratio in the molten salt system (Eq. (7-8)). Since both the alloy formation rate and the Dy/Nd separation ratio are sufficiently high for the sample prepared at 0.60 V, Dy can be selectively separated with high efficiency and precision in this condition. The analysis results of the samples prepared at other potentials are shown in Fig. 5-8. RENi$_2$ alloy was formed from 0.60 V and the highest Dy/Nd ratio was also achieved at this potential. Compared with the last system, RENi$_2$ alloy was formed at a more positive potential. As the concentration of the RE component is increased, the activity of RE^{3+} is also increased, thus shifting the formation potential of the RE–Ni alloy to positive. The formation of the RENi$_2$ alloy at 0.60 V was mainly due to the higher Dy concentration in this system. As discussed in Chapter 4, high Dy/Nd ratios can be obtained at potentials where the alloy formation rates of Nd–Ni and Dy–Ni
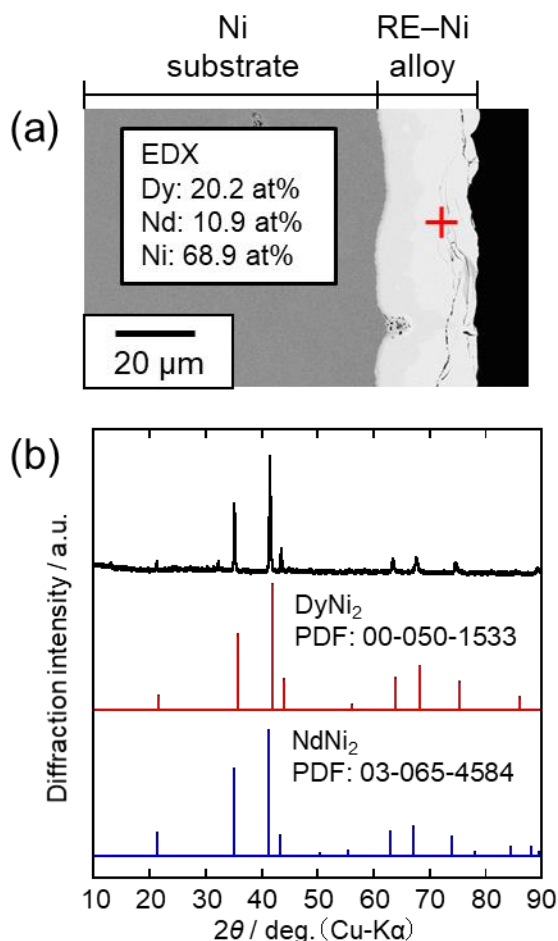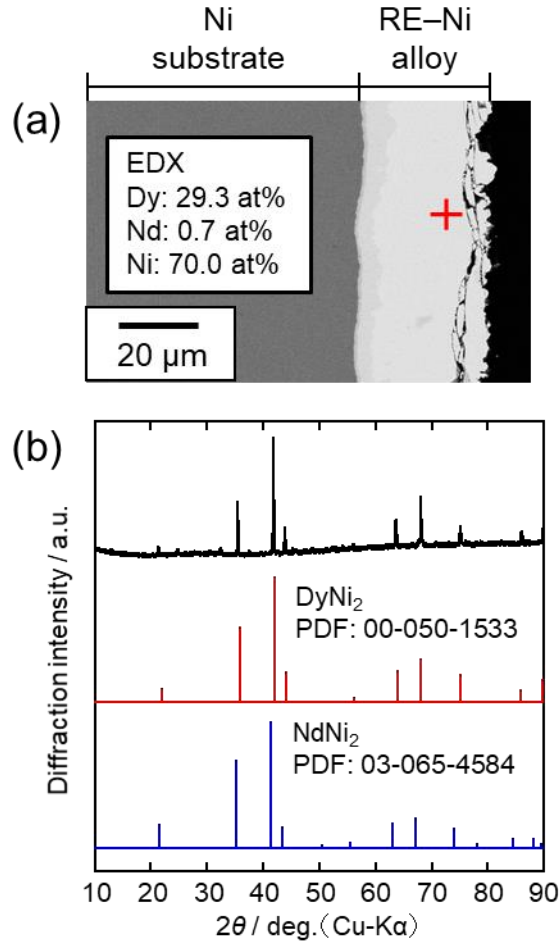
Fig. 5-7 **(a) A cross-sectional SEM image with EDX analysis results and (b) an XRD pattern of the sample obtained by potentiostatic electrolysis with a Ni electrode at 0.60 V for 30 min in a molten $CaCl_2$–CaF_2 (9.00 mol%)–$NdCl_3$ (2.00 mol%)–$DyCl_3$ (1.00 mol%) system at 1123 K.**

are largely different. Since the alloy formation potential of Dy–Ni is positively shifted in this system, the difference in the alloy formation rate between Nd–Ni and Dy–Ni is larger than in the last system, resulting in a higher Dy/Nd ratio. The Dy/Nd ratios of the samples electrolyzed at 0.55, 0.50, and 0.45 V were over 20, which also meet the requirement of high precision Dy separation. Furthermore, the alloy formation rates at these potentials, 108, 119, and 196 $\mu m\ h^{-1}$, were higher than that at 0.60 V. According to the above results, Dy can be separated from the Nd magnets used in BEVs/HEVs motors with high efficiency and precision.

Finally, the SEEE process capability is discussed as follows. As described in Chapter 4, the
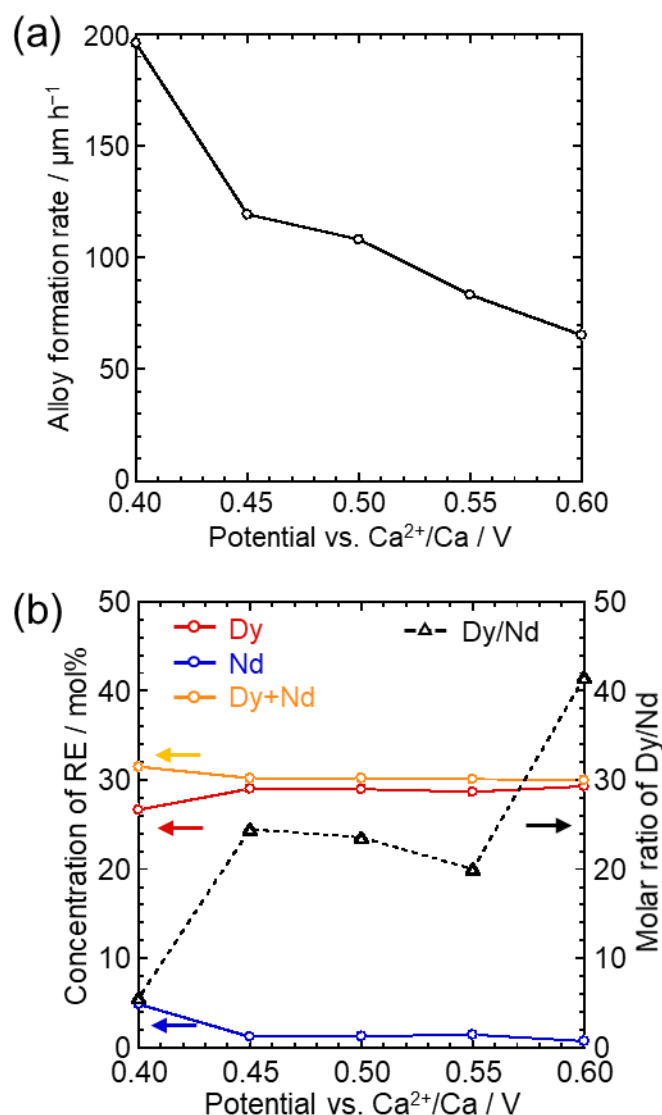
Fig. 5-8 **Potential dependence of (a) RE–Ni alloy formation rate, (b) concentration of RE and Dy/Nd ratio in the RE–Ni alloys. Samples obtained by potentiostatic electrolysis with Ni electrodes at various potentials for 30 min in a molten $CaCl_2$–CaF_2 (9.00 mol%)–$NdCl_3$ (2.00 mol%)–$DyCl_3$ (1.00 mol%) system at 1123 K.**

purity of the reusable Dy metal should be higher than 90%, therefore the $(Dy/Nd)_{alloy}$ should be higher than 9. Since $(Dy/Nd)_{salt}$ decreases with electrolysis, it is necessary to consider the lowest limit of $(Dy/Nd)_{salt}$ to obtain the target $(Dy/Nd)_{alloy}$ of 9. Table 5-2 summarizes the highest $(Dy/Nd)_{alloy}$ obtained in different molten $CaCl_2$–CaF_2–$NdCl_3$–$DyCl_3$ systems described in Chapters 4 and 5. As mentioned above, the molten salt with $(Dy/Nd)_{salt} = 0.5$ can be obtained after RE extraction from Nd magnet scraps used in BEVs/HEVs motors. Although the highest $(Dy/Nd)_{alloy}$

Table 5-2 The highest Dy/Nd ratios and corresponding Dy enrichment factors of alloy obtained in molten $CaCl_2$–CaF_2–$NdCl_3$–$DyCl_3$ (F/(Nd+Dy) = 6) salts with different Dy/Nd ratios at 1123 K.

Conc. of salts composition / mol%				$(Dy/Nd)_{salt}$	$(Dy/Nd)_{alloy}$	Potential / V vs. Ca^{2+}/Ca	f_{enrich}
$CaCl_2$	CaF_2	$NdCl_3$	$DyCl_3$				
92.0	6.00	1.83	0.17	0.09	4.1	0.55	46
88.0	9.00	2.00	1.00	0.50	42	0.60	84
92.0	6.00	1.00	1.00	1.00	45	0.60	45

obtained in this system is 42, the value of $(Dy/Nd)_{alloy}$ would decrease with decreasing $(Dy/Nd)_{salt}$. According to Table 5-2, $(Dy/Nd)_{alloy}$ of 9 would be obtained in molten salt with $(Dy/Nd)_{salt}$ between 0.09 and 0.50. Within this range, it is reasonable to speculate that $(Dy/Nd)_{salt}$ up to 0.20 can yield the $(Dy/Nd)_{alloy}$ of 9. Since the initial $(Dy/Nd)_{salt}$ is 0.50, there is still about 40% Dy left in the molten salt with $(Dy/Nd)_{salt}$ of 0.20. Consider the recovery of this remaining Dy as another alloy. Since the Dy/Nd ratio of the magnet scrap is 0.5, if an alloy with a $(Dy/Nd)_{alloy}$ of 0.5 or higher can be produced, it can be processed together with the scrap. In the same way as above, Table 5-2 shows that the $(Dy/Nd)_{alloy}$ of 0.50 would be obtained in the molten salt with $(Dy/Nd)_{salt}$ less than 0.09. Here, it is reasonable to speculate that the lowest limit of $(Dy/Nd)_{salt}$ is 0.05 to obtain a $(Dy/Nd)_{alloy}$ of 0.5.

The recovery rates and the purity of the recovered Nd and Dy metal products are estimated as follows. Fig. 12 shows the change in $(Dy/Nd)_{salt}$ and $(Dy/Nd)_{alloy}$ during SEEE process. Here, the final products of Dy metal with $(Dy/Nd)_{metal} > 9$ and Nd metal with $(Dy/Nd)_{metal} = 0.05$ are also described. In the C-1 step, Dy contained in the molten salt with $(Dy/Nd)_{salt} = 0.50$ is recovered as RE–Ni alloy with $(Dy/Nd)_{alloy} > 9$ until the $(Dy/Nd)_{salt}$ becomes 0.20. Here, 61% Dy and 3% Nd of raw material are contained in the alloy. In the C-2 step for Dy, the alloy is used to prepare the Dy metal product with the purity of Dy over 90%, which satisfies the requirements for the manufacturing of heat-resistant Nd magnets. To recover Dy left in the molten salt after the C-1 step, RE–Ni alloy with $(Dy/Nd)_{alloy} > 0.5$ is prepared until the $(Dy/Nd)_{salt}$ becomes 0.05. Here, 33% Dy
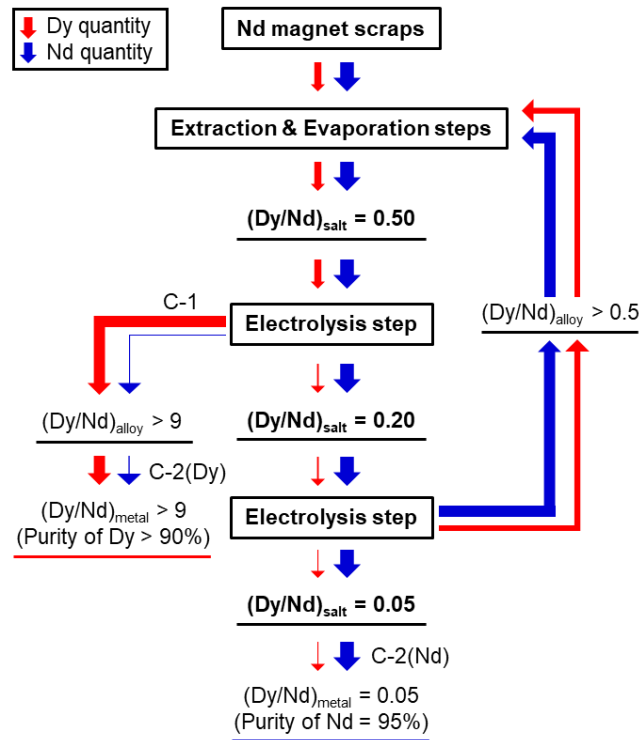
Fig. 5-9   **Dy/Nd ratio change in salt, alloy, and metal during SEEE process.**

and 33% Nd of raw material are contained in the alloy. The Dy and Nd contained in this alloy would be selectively extracted in the starting molten salt together with Nd magnet scraps. In the C-2 step for Nd, the Nd contained in the molten salt with $(Dy/Nd)_{salt} = 0.05$ is recovered as the Nd metal product with the purity of Nd over 95%. Here, 6% Dy and 64% Nd of raw material are contained in the Nd metal. Since Dy is lost only by contamination into Nd metal, the recovery rate of Dy is calculated as 91%. Due to the same reason, the recovery rate of Nd is calculated as 96%. It should be noted that the unrecovered Dy and Nd is contained in the Nd metal and Dy metal, therefore has not been lost when producing the magnet.

In summary, both Nd and Dy can be recovered as high purity RE metals and the recovery rates of them are sufficiently high in the (C) electrolysis steps. Therefore, the process capability of the SEEE process is verified.

5.4   Conclusions

The RE extraction and Mg evaporation steps were investigated in the molten $CaCl_2$–CaF_2–

$MgCl_2$ system using commercial heat-resistant Nd magnets. The Nd magnet samples were analyzed by XRD and SEM/EDX before and after the consecutive steps. Different amounts of $MgCl_2$ and CaF_2 were added into the system to investigate their influences on the extraction ratios of Dy, Nd, and Pr. Even when $MgCl_2$ was added with only 1 times of the stoichiometric value to extract 100% of RE, the extraction ratios of Dy, Nd, and Pr were all above 90%. The extraction limit of RE was reached when $MgCl_2$ was added with 2 times. The high extraction ratios of RE and the extraction limit of RE were explained by the thermodynamic analysis based on the standard Gibbs energies of RE extraction reactions. The influence of CaF_2 addition on the extraction ratio of RE was found to be small, at least until the concentration of F^- was 6 times higher than the concentration of RE. The addition of CaF_2 obviously suppressed the evaporation of RE, while the evaporation of Mg was almost unaltered. The phenomena were explained by selective fluorination of RE ions. Evaporated Mg could be recovered at a low temperature part of container without vacuum evaporation, which indicates that Mg evaporation occurs easily.

Electrolysis separation of Dy and Nd using Ni electrodes was first conducted in a molten $CaCl_2$–CaF_2 (6.00 mol%)–$NdCl_3$ (1.83 mol%)–$DyCl_3$ (0.17 mol%) system, which had the similar Dy/Nd ratio of 0.09 as the commercial heat-resistant Nd magnet. In this system, Dy was enriched by 21 times by fabricating RE–Ni alloys at 0.50 V, where an alloy formation rate was 47 μm h^{-1}. Electrolysis separation of Dy and Nd was also performed in a molten $CaCl_2$–CaF_2 (9.00 mol%)–$NdCl_3$ (2.00 mol%)–$DyCl_3$ (1.00 mol%) system, which had the similar Dy/Nd ratio of 0.5 as the Nd magnet used in the motor of BEVs/HEVs. Dy was enriched by 84 times at 0.60 V with an alloy formation rate of 65 μm h^{-1}.

The capability of SEEE process for RE recycling from the Nd magnet used in BEVs/HEVs motors was estimated by considering the Dy/Nd separation results obtained in molten salts with different (Dy/Nd)$_{salt}$. The final product of Dy is recovered as Dy metal with the purity of over 90% and the recovery rate is 91%. While 96% of Nd is recovered as Nd metal product with the purity of 95%. Both Nd and Dy can be recovered as high purity RE metals and the recovery rates are

sufficiently high, which confirms the high processing capability of the SEEE process.

References

1. S. Shirayama and T. H. Okabe, *Metall. Mater. Trans. B,* **49**, 1067 (2018).

2. A. Roine and P. Kobylin, *HSC Chemistry*®, ver 9, Outotec Information Center, Pori, Finland (2016).

Chapter 6
General Conclusion

In order to develop a highly efficient and precise RE separation and recycling process from Nd magnet scraps, a combination process named "SEEE process" including selective extraction, evaporation, and electrolysis is proposed in this study. To verify that each step is effective, experiments were conducted and the results are summarized below.

In Chapter 2, the electrochemical behaviors of Nd^{3+} and Dy^{3+} were investigated at 1123 K in molten $CaCl_2$–$NdCl_3$ (1.0 mol%) and $CaCl_2$–$DyCl_3$ (1.0 mol%) systems, respectively. The deposition potential of metallic Nd and Dy were 0.27 and 0.33 V vs. Ca^{2+}/Ca. The open-circuit potentiometry after electrolysis of Ni electrodes at various conditions showed three potential plateaus at 0.48, 0.68, and 0.95 V in the $NdCl_3$ addition system and four potential plateaus at 0.49, 0.62, 0.87, and 1.04 V in the $DyCl_3$ addition system. The observed potential plateaus suggested different two-phase coexisting states. According to the SEM, EDX, and XRD analysis results, the thermodynamically stable phases at 0.30, 0.50, 0.80, and 1.00 V were $NdNi_2$, $NdNi_3$, $NdNi_5$, and Ni, respectively, in the $CaCl_2$–$NdCl_3$ system. As for the $CaCl_2$–$DyCl_3$ system, the thermodynamically stable phases at 0.40, 0.50, 0.70, 0.90, and 1.20 V were DyNi, $DyNi_2$, $DyNi_3$, $DyNi_5$, and Ni, respectively.

In Chapter 3, the two-phase coexisting potentials of ($NdNi_2$ + $NdNi_3$), ($NdNi_3$ + $NdNi_5$), and ($NdNi_5$ + Ni) were investigated at 1073–1173 K in a molten $CaCl_2$–$NdCl_3$ (1.0 mol%) system. The relative partial molar quantities and activities of Nd and Ni were calculated using the two-phase coexisting potentials. The relative partial molar Gibbs energies of Nd and Ni were used to calculate the standard Gibbs energies of formation for the Nd–Ni alloys. The obtained values were

compared with those other studies that employed the CALPHAD and calorimetry. Similar research was also carried out in a molten $CaCl_2$–$DyCl_3$ (1.0 mol%) system to investigate the two-phase coexisting potentials and the thermodynamic properties of Dy–Ni alloys. Both the standard Gibbs energies of formation for the Nd–Ni and Dy–Ni alloys were lower than the reported values. Possible reasons for the differences were proposed and a wider experimental temperature range was suggested to obtain a more reliable determination.

In Chapter 4, the formation rates of Nd–Ni and Dy–Ni alloys were estimated at various potentials at 1123 K. At both 0.50 V and 0.60 V, a large difference in the alloy formation rate between Nd–Ni and Dy–Ni alloys is observed, suggesting a high Dy/Nd separation ratio. The alloy formation rate and Dy/Nd separation ratio were measured using molten $CaCl_2$ containing the same concentrations of $NdCl_3$ and $DyCl_3$. The maximum Dy/Nd separation ratio of 96 was obtained at 0.60 V with an alloy formation rate of 48 $\mu m\ h^{-1}$. Although the highest alloy formation rate of 160 $\mu m\ h^{-1}$ was obtained at 0.40 V, the Dy/Nd separation ratio was as low as 3.

The effect of F^- is then investigated by adding CaF_2 to the $CaCl_2$ melt. The alloy formation rate decreases with increasing CaF_2 concentration and the effect is relatively stronger at negative electrolysis potentials. As for the Dy/Nd separation ratio, a specific phenomenon was observed. The Dy/Nd separation ratio at 0.60 V decreases with increasing CaF_2 concentration, and remains relatively high as 35 even at 10 mol%. On the other hand, at 0.40 V, the Dy/Nd separation ratio increases with CaF_2 concentration, reaching a maximum value of 29 at 6 mol%, with a high alloy formation rate of 113 $\mu m\ h^{-1}$. Then, as the CaF_2 concentration increases to 10 mol%, the separation ratio decreases slightly to 23. This change in the Dy/Nd separation ratio is explained as follows: with increasing CaF_2 concentration, Dy^{3+} is preferentially coordinated by F^- first, followed by Nd^{3+}, which changes the overpotential used for alloy formation and changes the alloy formation rate. It is found that highly efficient and precise Dy separation is expected by the RE–Ni alloy formation in the molten $CaCl_2$–CaF_2 system.

In Chapter 5, The RE extraction and Mg evaporation steps were investigated in the molten

CaCl$_2$–CaF$_2$–MgCl$_2$ system using commercial heat-resistant Nd magnets. The Nd magnet samples were analyzed by XRD and SEM/EDX before and after the consecutive steps. Different amounts of MgCl$_2$ and CaF$_2$ were added into the system to investigate their influences on the extraction ratios of Dy, Nd, and Pr. Even when MgCl$_2$ was added with only 1 times of the stoichiometric value to extract 100% of RE, the extraction ratios of Dy, Nd, and Pr were all above 90%. The extraction limit of RE was reached when MgCl$_2$ was added with 2 times. The high extraction ratios of RE and the extraction limit of RE were explained by the thermodynamic analysis based on the standard Gibbs energies of RE extraction reactions. The influence of CaF$_2$ addition on the extraction ratio of RE was found to be small, at least until the concentration of F$^-$ was 6 times higher than the RE concentration. The addition of CaF$_2$ obviously suppressed the evaporation of RE, while the evaporation of Mg was almost unaltered. The phenomena were explained by selective fluorination of RE ions. Evaporated Mg could be recovered at a low temperature part of container without vacuum evaporation, which indicates that Mg evaporation occurs easily.

Electrolysis separation of Dy and Nd using Ni electrodes was first conducted in a molten CaCl$_2$–CaF$_2$ (6.00 mol%)–NdCl$_3$ (1.83 mol%)–DyCl$_3$ (0.17 mol%) system, which had the similar Dy/Nd ratio of 0.09 as the commercial heat-resistant Nd magnet. In this system, Dy was enriched by 21 times by fabricating RE–Ni alloys at 0.50 V, where an alloy formation rate was 47 μm h^{-1}. Electrolysis separation of Dy and Nd was also performed in a molten CaCl$_2$–CaF$_2$ (9.00 mol%)–NdCl$_3$ (2.00 mol%)–DyCl$_3$ (1.00 mol%) system, which had the similar Dy/Nd ratio of 0.5 as the Nd magnet used in the motor of BEVs/HEVs. Dy was enriched by 84 times at 0.60 V with an alloy formation rate of 65 μm h^{-1}. The capability of SEEE process for RE recycling from the Nd magnet used in BEVs/HEVs motors was estimated by considering the Dy/Nd separation results obtained in molten salts with different (Dy/Nd)$_{salt}$. The final product of Dy is recovered as Dy metal with the purity of over 90% and the recovery rate is 91%. While 96% of Nd is recovered as Nd metal product with the purity of 95%. Both Nd and Dy can be recovered as high purity RE metals and the recovery rates are sufficiently high, which confirms the processing capability of the SEEE process.

Throughout a series of experiments carried out in Chapters 2–5, each step of the SEEE process was verified. The entire process is described as follows. In the RE extraction step, Nd magnet scraps are immersed in a molten $CaCl_2$ system at high temperature. $MgCl_2$ is added into the molten $CaCl_2$ with 1 times the stoichiometric amount for 100% RE extraction from the Nd magnet scraps and CaF_2 is added with 3 times the amount of RE^{3+} to suppress the evaporation of RE. After the reaction, most of RE contained in the Nd magnet scraps can be extracted into the molten salt. In the evaporation step, Mg and $MgCl_2$ are evaporated by decreasing the pressure. At a specific low temperature part, Mg and $MgCl_2$ are selectively recovered. In the RE electrolysis separation step, Dy is highly enriched by the formation of Dy–Ni alloy at a specific potential. After the separation of Dy, Nd is removed as Nd metal by electrolysis at a sufficiently negative potential using a Mo electrode. Cl_2 gas formed at the counter electrode is reused to chlorinate the Mg metal recovered in the evaporation step. $MgCl_2$ and regenerated molten $CaCl_2$–CaF_2 are reused in the RE extraction step. In another molten salt, Dy^{3+} is anodically dissolved from the Dy–Ni alloy obtained from the previous step and Dy metal can be electrodeposited using Mo as the cathode. After releasing Dy, the Dy-free Ni electrode is reused as the cathode in the Dy/Nd electrolysis separation step.

The SEEE process is a feasible, simple, and efficient method to recycle RE from Nd magnet scraps. The entire process consumes only Nd magnet scraps and electricity, and generates almost only Fe–B alloy as a by-product. Herein, the behavior of Ni and Cu contained in the surface coating layer is unknown at this stage. However, in the present process, around 30% of Dy in the RE extraction salt is lost in the Mg evaporation step, as described in 5.3.1.2. In order to increase the recycling ratio of Dy, the evaporation of Dy should be further suppressed by changing the amount of CaF_2 added, evaporation temperature, evaporation time, and vacuum degree. Furthermore, in the present study, the electrolysis experiments were conducted using $CaCl_2$–CaF_2 without $Mg/MgCl_2$ as the molten salt after RE extraction and Mg evaporation steps. However, as described in 5.3.1.2, in the actual molten salt after Mg evaporation step, at least 1% of Mg would be left in the salt as

MgCl$_2$, which could influence the Dy/Nd electrolysis separation. Other Mg removal methods such as pre-electrolysis need to be considered. Finally, the recovery of Cl$_2$ gas and the chlorination of Mg metal have not been experimentally investigated. In order to further reduce the environmental load, these parts of the process need to be carefully considered.

Concerning the worldwide expectation of carbon neutrality, the rapid spread of BEVs/HEVs is foreseeable and an environmental-friendly process to recycle RE from magnets used in BEVs/HEVs will be required. In addition, this process can be used not only for RE recycling from magnets, but also for reprocessing of nuclear fuel. Although the SEEE process still needs some technical details to be worked out, this study has largely proven that the process is effective. The SEEE process is expected to use both academically and industrially for the construction of a carbon-neutral society.

List of Publications

The main parts of this thesis are constructed from the following papers.

Chapter 2

1. Hang Hua, Kouji Yasuda, Hirokazu Konishi, and Toshiyuki Nohira
   "Electrochemical Formation of Dy–Ni Alloys in Molten $CaCl_2$–$DyCl_3$"
   Journal of the Electrochemical Society, **167**, 142504 (2020).
2. Hang Hua, Kouji Yasuda, Hirokazu Konishi, and Toshiyuki Nohira
   "Electrochemical Formation of Nd–Ni Alloys in Molten $CaCl_2$–$NdCl_3$"
   Journal of the Electrochemical Society, **168**, 032506 (2021).

Chapter 3

3. Hang Hua, Kouji Yasuda, and Toshiyuki Nohira
   "Thermodynamic Properties of Ni–Dy Intermetallic Compounds Measured Electrochemically in Molten $CaCl_2$–$DyCl_3$"
   Journal of the Electrochemical Society, **168**, 102501 (2021).
4. Hang Hua, Kouji Yasuda, and Toshiyuki Nohira
   "Thermodynamic Properties of Ni–Nd Intermetallic Compounds Measured Electrochemically in Molten $CaCl_2$–$NdCl_3$"
   Journal of the Electrochemical Society, **168**, 112506 (2021).

Chapter 4

5. Hang Hua, Kouji Yasuda, and Toshiyuki Nohira
   "Highly Efficient and Precise Electrolysis Separation of Dysprosium from Neodymium for Magnet Scrap Recycling in Molten Salt"
   Electrochimica Acta, submitted.

Chapter 5

6. Hang Hua, Kouji Yasuda, Yutaro Norikawa, and Toshiyuki Nohira
   "Selective Extraction-Evaporation-Electrolysis (SEEE) Process for Highly Efficient and Precise Separation Recycling of Rare-Earth Elements from Neodymium Magnet Scraps in Molten Salt"
   Energy & Environmental Science, to be submitted.

Acknowledgement

First of all, I would like to give my sincere gratitude to my supervisor Professor Toshiyuki Nohira. Under the guidance of Prof. Nohira, I have changed from not knowing to knowing about the field of study, from knowing little to being able to conduct indepth research on a certain aspect, enriching knowledge, and broadening my horizons. In the process of writing this thesis, a lot of his efforts were poured into it. Prof. Nohira's truthfulness, solid theoretical skills and writing skills have left an indelible impression on me and have benefited me for life. Prof. Nohira's teachings to students in work and life have been the greatest reward during my doctoral study and a great asset in my life. I am aware that my academic research level is still far from the requirements of Prof. Nohira, and I have to make extra efforts in my future work and study in order to live up to the sincere teaching and ardent hope of Prof. Nohira.

Special thanks are given to Professor Rika Hagiwara for his rewarding discussions and valuable suggestions. The author also wishes to thank Professor Tetsuya Uda of the Graduate School of Engineering, Kyoto University for fruitful discussion.

I would like to express my appreciation to Associate Professor Kouji Yasuda of the Graduate School of Engineering, Kyoto University for deep discussions and valuable advice. Not only for the experiments but also for the paper writing skills and manners of working people. I also want to expresses my appreciation to Assistant Professor Hirokazu Konishi Graduate School of Engineering, Osaka University. Without his leading, I would not enter the field of molten salt research and would not join to the Nohira laboratory.

Special acknowledgements are due to Associate Professor Tsutomu Kodaki and Kenji Kawaguchi for their useful advice and continuous encouragement throughout this study. Also, deeply thanks to Assistant Professor Takayuki Yamamoto for his kind guidance and discussions. I would also like to thank Assistant Professor Yutaro Norikawa for his helpful discussions, valuable advice on experiments, and continuous encouragement for this study. His perseverance, wit, and

hard work have inspired me time and time again. Special thanks are extended to Mr. Junichi Imaru for his technical support especially for constructing the experimental equipment.

Looking back at the difficulties and turns encountered in research and life, I sincerely thank all the members in Nohira laboratory, without their daily discussions, warm encouragements, and having a chance for friendly competition, I would not go to this day. Special thank is due to Dr. Yuanjia Ma for her help in experiments and lively discussions. Also, the special thanks are for Ms. Hiromi Takatori and Ms. Naoko Sakamoto for their help in administrative works and daily encouragement.

Thanks, all researchers and students for the technical discussions in the conferences, official and unofficial meetings, and the events in the Institute of Advanced Energy and in the Graduate School of Energy Science in Kyoto University. I would like to appreciate the financial support from the JSPS.

Thanks to my parents far away in my hometown. They have supported my study, work, and life with the simplest actions, and provided selfless support and encouragement when I was frustrated and hesitated. Their accompany and support gave me the courage and perseverance to learn more and more. The completion of my studies also condenses more of their hard work.

Finally, I would like to extend my sincere thanks and best wishes to all the professors, friends, and family members who have educated me, supported me, helped me, and cared about me. Thank you.

March 2022

Hang Hua